Silica hollow core fibres for mid-infrared medical applications

Artur Urich

Submitted for the degree of Doctor of Philosophy

Heriot-Watt University

School of Engineering and Physical Sciences

August 2013

Abstract

In this thesis two types of silica hollow core microstructured fibres - the Negative Curvature Fibre and the Photonic Bandgap Fibre - are presented as a novel solution for the flexible delivery of Er:YAG laser radiation. The Negative Curvature Fibre and Photonic Bandgap Fibre had attenuations of 0.06 dB/m and 1.1 dB/m at 2.94 µm wavelength, respectively. This is an important wavelength regime for medical applications, specifically surgery, due to the existence of a strong absorption peak for water around 3 µm. The guidance of high energy pulses of the order of 195 mJ and 14.4 mJ respectively is demonstrated. These energies are sufficient to ablate soft and hard biological tissue. As verification, porcine bone was ablated in air and submerged in water to simulate practical application of a surgical device. The presented fibres are compared to alternative state-of-the-art solid and hollow core fibres, in respect of the fabrication, attenuation, pulse energy delivery capability, bend sensitivity and the output beam profile. The fabrication and characterisation of a novel sapphire endtip is also presented, which seals the hollow cores of the fibres from contamination and therefore increases the usability significantly. The endtip was shown to be mechanically robust, provide a hermetic seal and able to survive practical tissue ablation in air and water. These encapsulated fibres provide a new fully flexible delivery system for high energy Er:YAG laser radiation and hence will open up the possibility of new minimally invasive surgical procedures.

Acknowledgment

Firstly I would like to thank Dr. Jonathan Shephard for the opportunity of doing a PhD with him and the Applied Optics and Photonics group. Without his support and guidance this work would have not been possible. I'm glad I had the chance to work with him and appreciate his open, friendly and respectful attitude.

Also I'm thankful to the rest of the group and my colleagues, in particular Prof. Duncan Hand, Dr. Robert Maier, Dr. Richard Carter and Dr. Tiina Delmonte. Special thanks go to all the support staff of the university, who were always there to help throughout the project.

I would also like to thank our collaborators from the University of Bath, for the fabrication of the fibres used in this work, without whom this work would not have been possible.

I'm glad that during the time at the Heriot-Watt University I made many friends so that the time outside of the lab was also enjoyable. I also want to thank Mandy for the reminder that an occasional break is necessary to keep a calm and relaxed attitude during the sometimes more stressful periods.

I would like to thank my family for all the support over the years, which kept me on track. I would also like to give a special thanks to my partner, Sarah. Thank you for believing in me and being there for me all the time.

Herzlichen Dank an meine Familie für all die Unterstützung über all die Jahre, die mich auf dem Weg begleitet haben. Ich bedanke mich insbesondere bei meiner Freundin Sarah. Danke das ihr an mich geglaubt habt und immer für mich da ward.

Thank you!

Danke!

ACADEMIC REGISTRY
Research Thesis Submission

Name*:*	Artur Urich		
School/PGI:	Engineering and Physical Sciences		
Version: *(i.e. First, Resubmission, Final)*	Final	Degree Sought (Award **and** Subject area)	PhD

Declaration

In accordance with the appropriate regulations I hereby submit my thesis and I declare that:

1) the thesis embodies the results of my own work and has been composed by myself
2) where appropriate, I have made acknowledgement of the work of others and have made reference to work carried out in collaboration with other persons
3) the thesis is the correct version of the thesis for submission and is the same version as any electronic versions submitted*.
4) my thesis for the award referred to, deposited in the Heriot-Watt University Library, should be made available for loan or photocopying and be available via the Institutional Repository, subject to such conditions as the Librarian may require
5) I understand that as a student of the University I am required to abide by the Regulations of the University and to conform to its discipline.

* *Please note that it is the responsibility of the candidate to ensure that the correct version of the thesis is submitted.*

Signature of Candidate*:*		Date:	

Submission

Submitted By *(name in capitals):*	
Signature of Individual Submitting:	
Date Submitted:	

For Completion in the Student Service Centre (SSC)

Received in the SSC by *(name in capitals):*			
Method of Submission *(Handed in to SSC; posted through internal/external mail):*			
*E-thesis Submitted (**mandatory for final theses)***			
Signature:		Date:	

Contents

Glossary

a	Core/Bore radius
A	Area
AG	Air-Guiding
a_{ab}	Absorption constant
α_{bend}	Bend depending losses
ARROW	Anti-Resonance Reflective Optical Waveguide
β	Wavevector
BG	Bragg fibre
Λ	Pitch
c	Speed of light
COP	Cycling Olefin Polymer
d	Diameter
D	Beam diameter
D_c	Clip Width
DC	Double Crucible
ε	Clipping level
Er,Cr:YSGG	Erbium, Chromium: Yttrium, Scandium, Gallium, Garnet
Er:YAG	Erbium : Yttrium Aluminium Garnet
υ	Displacement
F	Force
FPR	Fabry-Perot Resonator
FWHM	Full Width Half Maximum
HAZ	Heat Affected Zone
HC	Hollow Core
HC-NCF	Hollow Core-Negative Curvature Fibre
HC-PCF	Hollow Core-Photonic Crystal Fibre
HNA	High Numerical Aperture
HNL	Highly Non-linear
HWG	Hollow Waveguides
ID	Inner Diameter
IR	Infrared
k	Wavenumber
LASEK	Laser Subepitheal Keratomileusis
LASIK	Laser In Situ Keratomileusis
LHPG	Laser Heated Pedestal Growth
LIC	Low Index Core
LIDT	Laser Induced Damage Threshold
LMA	Large Mode Area
m	number of supported modes
M^2	Beam quality factor
λ	Wavelength
λ_{res}	Resonant wavelength
MOF	Microstructured Optical Fibre
MSF	Microstructured Fibre
n	Refractive index
n_2	Non-linear refractive index
n_{cl}	Refractive index of the cladding
n_{co}	Refractive index of the core
na	Not available/applicable
NA	Numerical aperture
NRL	Naval Research Laboratory
OD	Outer diameter
OM	Optical microscope
ω	Frequency
$\omega_{(z)}$	Local beam radius
ω_0	Beam waist
OPO	Optical Parametric Oscillator
P_0	Total transmitted Power
PBF	Photonic Bandgap Fibre
PC	Polycarbonate
PCF	Photonic Crystal Fibre
R	Bending Radius
R^2	Coefficient of determination
R_C	Critical angle
ρ	Density
SC	Single Crucible
SCW	Surface Capillary Waves
SEM	Scanning Electron Microscope
σ_{surf}	Surface roughness
σ	Standard deviation
T	Transparency
τ	Sheer stress
TEM	Transverse Electromagnetic Mode
T_g	Glass Transition temperature
Θ_B	Brewster angle
Θ_C	Critical angle/maximum launch angle

TIR	Total Internal Reflection	Z_R	Rayleigh length
UV	Ultra Violet	ZBLAN	ZrF4–BaF2–LaF3–AlF3–NaF

Publications

Urich, A., R.R.J. Maier, B.J. Mangan, S. Renshaw, J.C. Knight, D.P. Hand, and J.D. Shephard, *Delivery of high energy Er:YAG pulsed laser light at 2.94 µm through a silica hollow core photonic crystal fibre.* Optics Express, 2012. **20**(6): p. 6677-6684.

Urich, A., R.R.J. Maier, F. Yu, J.C. Knight, D.P. Hand, and J.D. Shephard, *Silica hollow core microstructured fibres for mid-infrared surgical applications.* Journal of Non-Crystalline Solids, 2013. **377**: p. 236-239.

Urich, A., R.R.J. Maier, F. Yu, J.C. Knight, D.P. Hand, and J.D. Shephard, *Flexible delivery of Er:YAG radiation at 2.94 µm with negative curvature silica glass fibers: a new solution for minimally invasive surgical procedures.* Biomedical Optics Express, 2013. **4**(2): p. 193-205.

Urich, A., T. Delmonte, R.R.J. Maier, D.P. Hand, and J.D. Shephard, *Towards implementation of hollow core fibres for surgical applications*, in *Optical Fibers, Sensors, and Devices for Biomedical Diagnostics and Treatment Xi*, I. Gannot, Editor 2011, Spie-Int Soc Optical Engineering: Bellingham.

Urich, A., R.R.J. Maier, J.C. Knight, B.J. Mangan, S. Renshaw, D.P. Hand, and J.D. Shephard, *Fabrication of silica hollow core photonic crystal fibres for Er:YAG surgical applications*, in *Optical Fibers and Sensors for Medical Diagnostics and Treatment Applications Xii*, I. Gannot, Editor 2012, Spie-Int Soc Optical Engineering: Bellingham.

Urich, A., R.R.J. Maier, J.C. Knight, F. Yu, D.P. Hand, and J.D. Shephard, *Flexible delivery of Er:YAG radiation at 2.94 µm with novel hollow-core silica glass fibres: Demonstration of tissue ablation*, in *Optical Fibers and Sensors for Medical Diagnostics and Treatment Applications Xiii*, I. Gannot, Editor 2013, Spie-Int Soc Optical Engineering: Bellingham.

1 Introduction

Shortly after the invention of the laser in 1960 the idea that it could potentially revolutionise medicine was envisioned and indeed tests were carried out on malignant tumours using a ruby laser just a few years later [1, 2]. In addition to a wide range of therapeutic treatments the laser provides a means of cutting tissue to a precision on the scale of cells with the safety of selective tissue cutting. This inspired new medical procedures and provided a route to minimally invasive surgery. However, despite the now widespread use of lasers in many treatments ranging from dermatology to neurosurgery, there are still many barriers in the way of this "medical laser revolution". There is a reluctance of clinicians to use new (more complicated) systems in place of established techniques with which they are familiar and confident also, the significant initial costs in acquiring such systems is a larger disincentive. Different wavelengths have been used for medical applications but the most promising, particularly for surgery, are correlated to an absorption peak of water, which are the CO_2 (9.6-10.6 µm) and the Er:YAG (2.94 µm) laser. These mid- and far-infrared wavelengths present another issue, which is the flexible delivery of sufficient laser energy to the patient without restricting the clinician's or surgeon's movement. One of the most common solutions is to use an articulated arm (a system of rigid tubes with mirrors) which does provide the capability of high power delivery over a wide range of wavelengths. However this limits the movement of the surgeon and due to its bulky size and weight they are reluctant to use them. Moreover, articulated arms are not compatible with minimally invasive or endoscopic procedures. Therefore much research has been focussed on enabling a truly flexible delivery system with the use of fibre optics. A fibre based on silica would be attractive as it is established for telecommunications and has very well-known and stable material properties and fabrication processes. However silica has high intrinsic losses at the Er:YAG wavelength (~50 dB/m) (and is even higher for CO_2 wavelengths in the range of 10^7 dB/m [3]) and is therefore not suitable in the form of a solid core fibre. Therefore different materials and designs have been implemented to deliver mid-infrared (mid-IR) laser radiation such as chalcogenide fibres, germanium oxide fibres and hollow waveguides (HWG).

In recent years a revolution in fibre optics has taken place in the fabrication of the so called Photonic Bandgap Fibres (PBF) which has significantly changed the perspective of what is possible with fibres. These fibres guide by the use of a microstructured photonic bandgap cladding with a specific geometry which surrounds the core and

confines the light in the fibre. This has opened the new possibility of guidance in a hollow core not possible by normal total internal reflection as air has a lower index than glass. This bandgap guidance provided very low interaction of the light with the glass and hence realised very low losses and high damage thresholds compared to standard solid core fibres.

This work is concentrated on exploiting the novel properties of such silica *microstructured* fibres in order to provide a realistic and practical solution for the flexible delivery of an Er:YAG laser for surgical procedures. It involves the characterisation and demonstration of two types of microstructured silica hollow core fibres which guide in the mid-IR regime due to the photonic bandgap effect or an anti-resonance reflective optical waveguide (ARROW) effect. Both fibres have a hollow core to minimize the interaction of laser light with the material reducing the losses to the lowest reported at these wavelengths in a silica fibre. It is also important to have a high quality beam profile (i.e. Gaussian) for precision cutting. Fibres used to date for this application are multimode as they have a large core in order to overcome the light induced damage threshold (LIDT) arising from the strong interaction of the light with the solid material. These multimode fibres are also highly bend sensitive which is a critical flaw for medical applications which demands a constant output energy independent of the fibre's configuration. In comparison it is presented here that the silica microstructured fibres can achieve a single-mode like guidance with a high pulse energy delivery capability which is more than sufficient to ablate soft and hard tissue. In addition the fibres are highly flexible and experience none or minimal additional losses due to bending.

The fibres described in this work will address the search for a truly flexible delivery system for medical laser radiation. Ultimately it is envisioned that the advances of the fibres could not just improve on existing methods and systems, but also open new fields of medicine to the advantages of laser, particularly for minimally invasive surgery.

The fibres were designed and fabricated from the group around Prof. Jonathan Knight at the University of Bath, UK. The design and optimisation of the presented fibres are not part of this thesis.

The aim of this work is to present an alternative for the delivery of mid-IR laser radiation to the established methods, in from a two novel silica hollow core fibres. The application of these fibres in this work is concentrated on medical proceedings, specifically high power applications like surgery. The feasibility of using the fibres will as a delivery tool and the performing hard and soft tissue ablation will be shown.

The presented work is divided into eight Chapters:

Chapter 1 will introduce the relevant literature and background related to this work. Starting with the medical use of lasers and how they are distinguished depending on the laser output power and the irradiation time. This is followed by a closer investigation of laser tissue ablation with focus on the use of Er:YAG lasers, and delivery systems already in use for medical applications. The available delivery systems for 2.94 µm are divided into "traditional" solid core and hollow core fibres and will form the main part of the literature review. The Chapter is concluded with the description of existing fibre encapsulation methods.

Chapter 2 presents the methods and measurement techniques used throughout the work, for example the imaging process and the measurement and calculation of the laser beam diameter. The Chapter also introduces the laser systems used for all the experiments carried out.

In Chapter 3 the results for the Hollow Core-Photonic Crystal Fibre (HC-PCF) are presented. The main sections include the fabrication, coupling efficiency, the bend sensitivity and the high energy pulse delivery capability. It will also be shown that the fibre has a single mode output beam profile in both straight and bent conditions.

Chapter 4 will present the results of the Hollow Core-Negative Curvature Fibre (HC-NCF) with the same focus as the previous Chapter for the HC-PCF.

The evaluation and discussion of the two presented fibres and established competitive fibres is given in Chapter 5. The main points of this critical analysis are the fabrication, high energy pulse delivery capability, the bend sensitivity and the output beam profile.

The encapsulation of the two hollow core fibres is reported in Chapter 6. Different attempts are given to show the reasoning of using the final design based on a sapphire tube and rod. The optical and mechanical properties of the final design are investigated at the end of the Chapter.

A demonstration of tissue ablation using the HC-NCF will be described in Chapter 7, and the results compared to other (established) laser delivery systems.

The final Chapter 8 will give a conclusions and suggestions of further work.

1.1 Medical applications and laser tissue interaction

The laser was envisioned as a tool for medical applications shortly after its invention [4]. In principle, laser surgery provides a non-contact solution with the ability to perform

cutting or ablation at the scale of a single cell, which is practically the fundamental resolution of biological tissue. Even if the cut itself is thinner than a single cell it would lead to the death of the cell cut, therefore limiting the practical cutting resolution. Also a self-selective cutting or ablation process was proposed achieved by tailoring the wavelength of the laser to the absorption spectrum of the tissue. However, in practice, the full potential of lasers system for surgical procedures is yet to be fulfilled and rather than the laser being a widely adopted tool by clinicians for surgery its use has been somewhat limited to specific (medical) niches.

Lasers are however used in fields such as dermatology, ophthalmology, dentistry, otolaryngology, gastroenterology, urology, gynaecology, neurosurgery and orthopaedics [5-12]. The laser-tissue interaction can be divided into six different categories: electromechanical, ablation, thermal (vaporisation and coagulation), photomechanical or photodisruptive and biostimulation [8], which are defined depending on the fluence and the exposure time. The different regimes are shown in Figure 1.

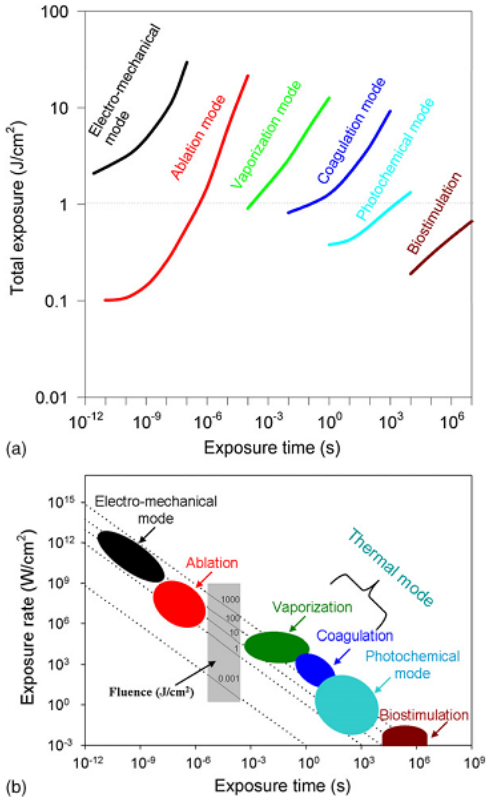

Figure 1: Definition of terms if a laser at the wavelength of 2.94 µm is used with different exposure times and exposure rates. (a) Different types of laser–tissue interaction dependent on total exposure and exposure time. (b) Different types of laser–tissue interaction dependent on exposure rate and interaction time (figure is adapted from [8]).

The relevant interaction in this work is the ablative laser-tissue interaction. The ablation is based on tissue melting and sublimation (direct phase change from solid to vapour), due to heating using the laser beam, followed by expulsion or ejection of the evaporated

material [8, 13]. The kinetic energy of the molecules and tissue fragments is provided by the excess energy of the pulse (typically longer than 10 ns). In most cases the target substance or molecule is water, which has a relatively low transition temperature, and is present in all biological tissue.

Consequently, a laser operating at a wavelength which overlaps with a strong absorption band of water would have high efficiency for tissue ablation. The water absorption versus the wavelength is shown in Figure 2 and the operating wavelengths of different laser systems are also shown. The Er:YAG laser is operated at strong absorption peak of water with an absorption factor α= 11.850 cm^{-1} [14] at 2.94 µm, leading to a short absorption depth (the depth at which the incident intensity is reduced to $1/e^2$) of ~300nm. Also Peavy et al. [15] stated that the best ablation results for bone can be achieved with lasers with wavelength of 2.9, 3.0 and 5.9-6.45 µm, therefore the Er:YAG laser is especially suitable for the cutting of mineralized tissue [16, 17].

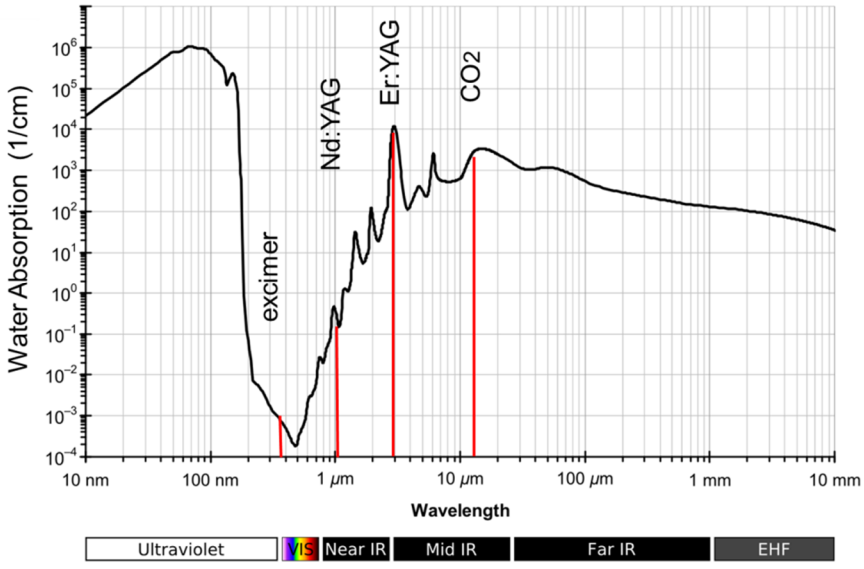

Figure 2: Absorption spectrum of liquid water versus the wavelength. Also included are the operating wavelengths of different lasers.

From Figure 2 it can also be seen that a CO_2 laser could be used for surgical application, however many studies in osteotomy showed that the use of this laser system leads to serious biological complications with severe carbonization effects and a delayed bone healing compared with conventional mechanical tools [18-21]. The reason for the collateral damage and the carbonization is the excessive heat leading to temperature rise of over 47°C in the tissue [22]. Eriksson and Albrektsson [23] demonstrated that temperature shifts between 44°C and 47°C in bone resulted in wound healing impairments

and thermal damage. Charred tissue and a high amount of debris aggravated the whole surgical procedure.

The use of lasers for medical applications offer several advantages compared to traditional/mechanical tools: blood reduced and vibration reduced surgery techniques, a small operation field, the prevention of massive bone flour and metal abrasion less tissue traumatization with no need of sutures, reduced scar formation and it is bacteriostatic [24-28]. Also the cut geometry is not dependent or limited by the size or shape of a mechanical part such as a drill or scalpel used but is controlled by the distribution of the energy in the tissue (spot size and laser bream profile) and the laser material interaction. This potentially provides a level of flexibility and control over the cut geometry and the possibility of producing holes much finer than traditional methods with diameters in the order of 0.5 mm [29]. Also, the non-contact nature of the laser process is attractive from a patient comfort point of view. In dentistry it has been shown that the use of a non-contact procedure eliminates the pressure on the tooth and therefore reduces the pain for the patient [13]. The non-contact and non-pressure attribute of lasers gives a beneficial alternative if thin and fragile bone has to be machined, for example in osteotomy of boney segments of the maxilla and mandible which are prone to fracture due to massive contact pressure. Furthermore, friction during conventional processing of hard tissue can cause severe mechanical trauma, pain and thermal damage to the adjacent remaining tissue, and the use of a drill or saw often results in a broadening of cuts and a subsequent deposit of metal shavings and bacterial contamination [29]. It could also be shown that the use of a laser could reduce the fear experienced by patients, as the characteristic drilling sound and vibrations are avoided [30]. Additionally, if a laser is used in non-contact mode there is no heating of the tip and therefore accidental thermal damage can be minimized, although the laser process itself must be optimised to avoid collateral damage to surrounding tissue. Another important advantage of the (Er:YAG) laser surgery is the possibility of faster wound healing compared to traditional mechanical tools, as studies could show [31, 32].

The previous stated advantages are based on already established proceedings which can be improved by using a laser system; however another very beneficial use of lasers is the possibility to create completely new methods and operations not possible with traditional tools. The most common and established would be the use of lasers in ophthalmology, in proceedings like Laser Subepithelial Keratomileusis (LASEK) [33] and Laser in Situ Keratomileusis (LASIK) [34].

However there are also some disadvantages in using lasers as a medical tool. Due the small rate of tissue removal in some procedures operation times are sometimes longer than with conventional drills [30]. From a patient perspective the smell during the proceedings has been described as unpleasant [13]. One major practical disadvantage from a surgeon's perspective is that there is a lack of (physical) feedback for the depth control if the laser is used in non-contact mode. Different approaches have been undertaken to solve this problem, one of them is based on the volumetric 3D data to navigate the laser ablation through a defined geometry [35-37]. Based on computer topographical data, cylindrical cavities were planned with the help of a navigation system inside bovine bone and the position of the headpiece was tracked optically to calculate the distance to the bone surface. The theoretical ablation depth was calculated for every single pulse on the basis of a special mathematical model and displayed by the navigation system. This system allowed a visualization of the ablation process with an accuracy of less than 1 mm [38]. This approach however has some flaws, as it is only a planar positioning system setup whereas in a clinical use it would be a (fully) free moving system, making the modelling and navigation more complicated. Also for the calculation of the ablation depth the bone was assumed to be homogenous, which is not the case, and the influence of blood, cooling water and boney debris on the ablation was not accounted for. Another approach was done by Rupprecht et al. [39, 40] using several sensors to pick up the acoustic, optical and thermal signals from the ablation side. As the group showed [41] these signals change with different tissue types, so that they were able to cut through cortical bone without any damage to the underlying cancellous bone. There was also no harm done to the soft tissue structure in the vicinity of the laser cut, such as the inferior alveolar nerve. This approach however works only if it is desired to cut completely through the specific tissue producing a change in the signal and is not appropriate if a specific cut depth is needed inside a single tissue type. Another drawback is that it can be difficult to maintain a constant distance between the end of the laser probe (hand piece or fibre end face) and the tissue during the operation; however this can be addressed by adding a distance holder to the output end which can be kept in constant contact with the tissue thus providing as fixed standoff. Also it is critical to keep the exit window clean to avoid etching of the lens/window due to overheating of debris [13]. Finally, as the time scale for the laser pulse is normally in the region of 10s of ns to 100s μs a shock wave can be generated due to a the micro-explosion which can lead to unwanted collateral damage of surrounding tissue [42].

The ablation process itself occurs due to the absorption of the laser energy due to the target material (in the case of this work water) in a very short time (tenth of ns) leading to an overheating and therefore a phase change with a high pressure build-up. The tissue water is evaporated almost instantly and the following steam explosion exceeds the cell and/or crystal strength of the irradiated soft and/or hard tissue, leading to a fragmentation and ejection of the tissue particles and debris at the localised heated spot [43].

1.1.1 Tissue ablation threshold and laser tissue interaction

The laser parameters that control the ablation of tissue are wavelength, pulse duration and pulse fluence, which is defined as pulse energy per unit area. The main laser used for this work operates at 2.94 µm with a pulse duration of 225 µs full width half maximum (FWHM) and 15 Hz repetition rate. The ablation thresholds for different biological tissues are given in Table 1, for laser parameters similar to the ones used for this work. From this table it can be seen that if an energy fluence of > 35 J/cm^2 is achieved, all tissue types inside a human body can be ablated.

Table 1: Ablation thresholds for different tissue types. (Rep. -- repetition, na -- not applicable)

Rep. rate /Hz	Pulse duration /µs	Tissue type	Threshold /Jcm^{-2}	Reference
2	250	Human dental enamel	35	[44]
7-10	250	Human skin	1.6	[45]
1.7	250	Pig retina	1	[46]
1	100-5000	Human dentine	2.69-3.66	[47, 48]
5	na	Pig skin (vitro)	3.6 - 5.6	[49]
2	200	Guinea pig skin	0.6-1.5	[50]

The pulse duration of 225 µs was chosen because previous experiments [51-53] have shown that the optimum pulse duration for (under water and water cooled) ablation of hard tissue is in the range of 200-300 µs. In this regime the ablation depth per pulse is highest and the collateral damage minimal. The reason being is a build-up of a steam cloud or plume 10 µs after the laser pulse irradiation which produces a channel between the laser output side and the tissue. The vibrational absorption of steam is lower than

liquid water, and the density is 100 to 1000 times lower [52, 53]. This leads to a 4 stage ablation process, first is the build-up of the steam cloud during which water micro-droplets are formed in a time of 0-60 µs after pulse start. The second stage is the expansion of the cloud and deposition of the droplets on the surface and under the top layer of tissue about 60-100 µs after the laser pulse start. The formation of the cloud is accompanied with pressures in the range of few tenth of mega-Pascal's , which can lead to ablation and damage to tissue. This is followed by the actual irradiation of the tissue with the laser leading to micro explosions of the water droplets deposited inside the tissue and the already existing water within the tissue. The final state is the implosion of the steam cloud which, due to the high pressures of hundreds of mega-Pascal's, removes loose and cracked material leading to an increased ablation volume [54]. A schematic of the process is presented in Figure 3, where an Er,Cr:YSGG laser was used on enamel, however the authors stated that the same process would be present if an Er:YAG laser would be used.

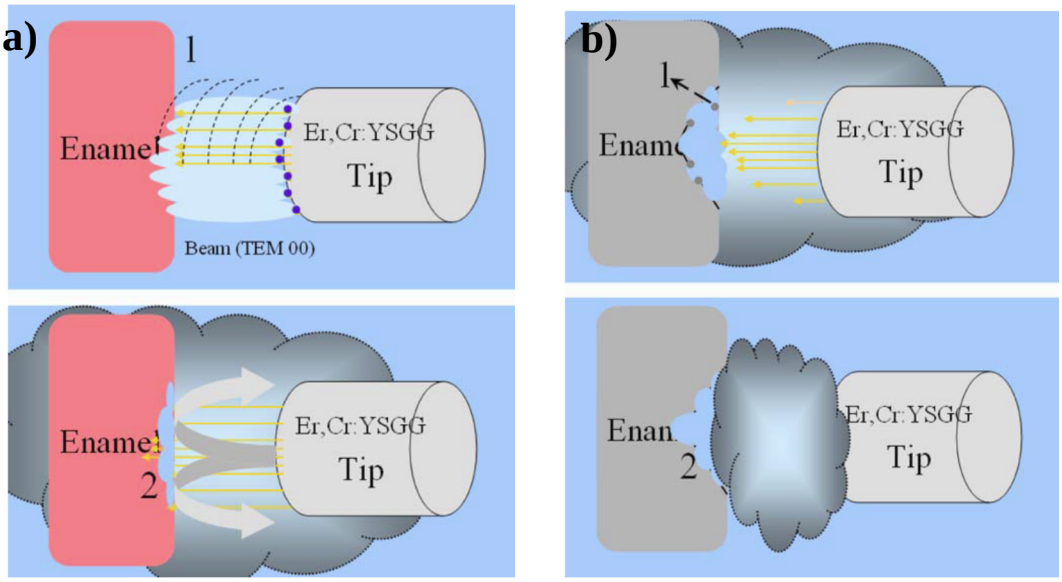

Figure 3: 4 stage ablation process of tissue under water: a1) build-up of the steam cloud and formation of water micro-droplets; a2) expansion of the steam cloud and deposition of water droplets into the tissue; b1) laser ablation process of the tissue through the cloud and b2) implosion of the steam cloud leading to removal of loose and cracked material. Presented in [54].

A study by Nahen et al. [55] investigated the dynamics of the steam cloud and its transmission properties for Er:YAG laser radiation. The authors concluded that due to the steam, water droplets and ejected tissue, only around 80-90% of the laser energy is deposited onto the material surface in the case of hard and soft tissue. This has to be considered if theoretical models are developed for clinical applications.

Many studies [54, 56, 57] have shown that the addition of water spray has a high impact on the ablation volume, the tissue narcosis and charring. Fried et al. [57] demonstrated that an appropriate (~1 mm) water layer on the bovine enamel can increase the cut depth by a factor of ~10 and produce much smoother und crack free surfaces. Figure 4 and Figure 5 illustrate the findings. Mir et al. [58] investigated the influence of the water layer thickness, the distance between the fibre output tip and the fluence and concluded that there is "no significant difference when using a different pulse ablation speed (cm^3/J) and a water-layer thickness between the tip and enamel surface of 0.5–1.25 mm with energy densities of 30–60 J/cm^2 (200 – 400 mJ)." This gives a certain regime at which the ablation efficiency is relative constant over a range of energy densities (30–60 J/cm^2) and distances of dental enamel and the fibre end (0.5 - 1.25 mm) if submerged in water.

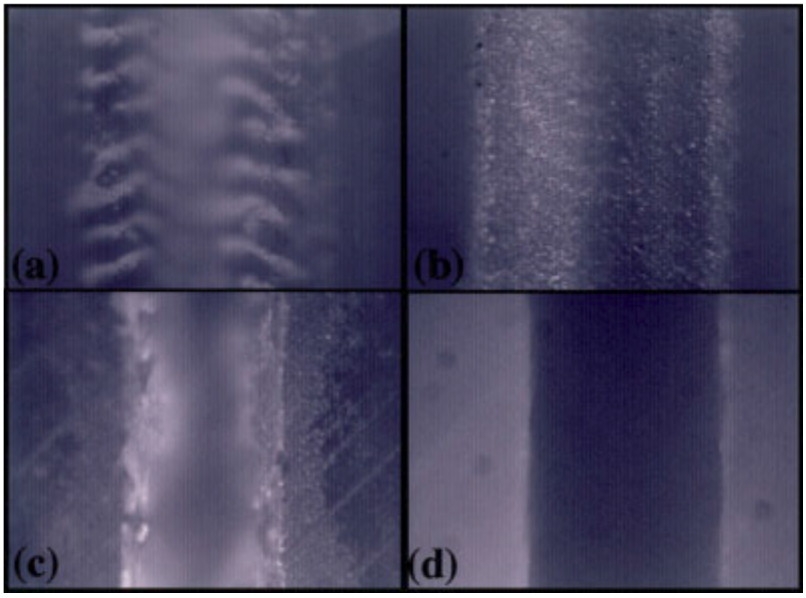

Figure 4: Lateral cuts in the surface of polished bovine blocks using a 9.6 µm TEA CO_2 laser pulse with a fluence of 70 J/cm^2: (a) no droplet added; (b) water added, and a Q-switched Er:YAG laser pulses with a fluence of 15 J/cm^2; (c) no water added and (d) a water droplet placed before each five laser pulses. Presented in [57].

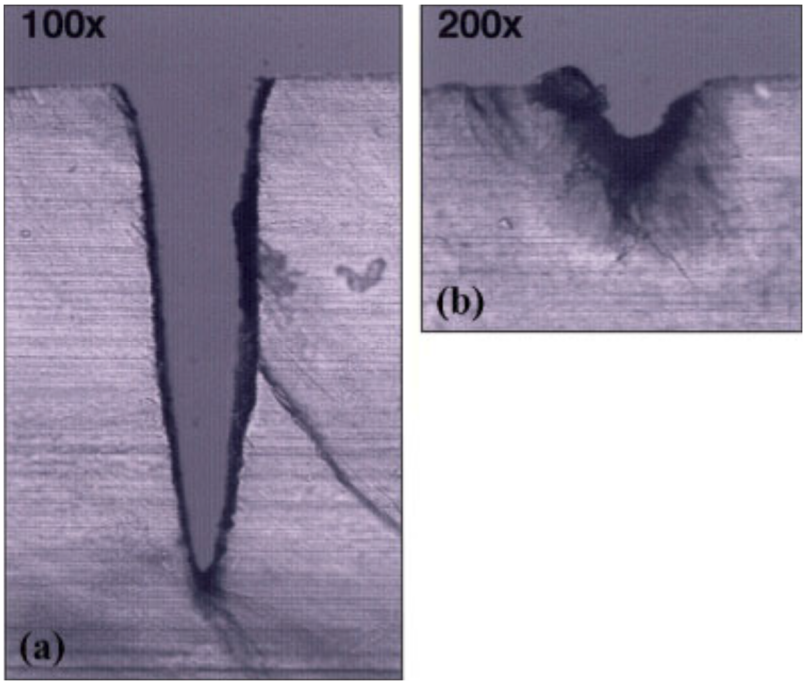

Figure 5: Polarized light images of 100 µm thick cross sections of the Q-switched Er:YAG laser cuts of Figure 4c,d with: (a) and without and (b) water. The respective crater dimensions are (a) 125 mm across and 490 mm in depth and (b) 33 mm across and 52 -mm deep. Presented in [57].

1.1.2 Systems in use

Ideally, for a laser to be a viable tool for surgical procedures the energy needs to be delivered flexibly from the laser unit to the patient using a robust and repeatable system that requires little or no technical expertise to align and operate. This would provide a surgeon a tool which they could pick up (in the same manner as they use a scalpel) and allow the surgeon to have complete freedom to perform intricate operations and would also enable the full benefits of laser energy to be utilised.

Currently there are two common systems in use to deliver radiation from the laser to the patient, the articulated arm and large core multimode fibres. The articulated arm [13] is a system of rigid tubes combined with movable joints containing mirrors and an interchangeable hand piece. The hand piece contains optics to generate a particular beam profile onto the tissue which is to be processed. There has been continued improvement of these systems and early issues, like beam wandering when the arm was moved, have been largely overcome. However, such arms can never be completely flexible in 3D space, and therefore restrict the surgeon. Generally, the size of the hand piece prevents the use of the articulated arm in minimally invasive surgery or in combination with endoscopy. An example of such an articulated arm and its internal guiding principal is shown in Figure 6, they are generally used with a red guiding laser so that the surgeon has a visible indication as to where the IR laser radiation is applied [13].

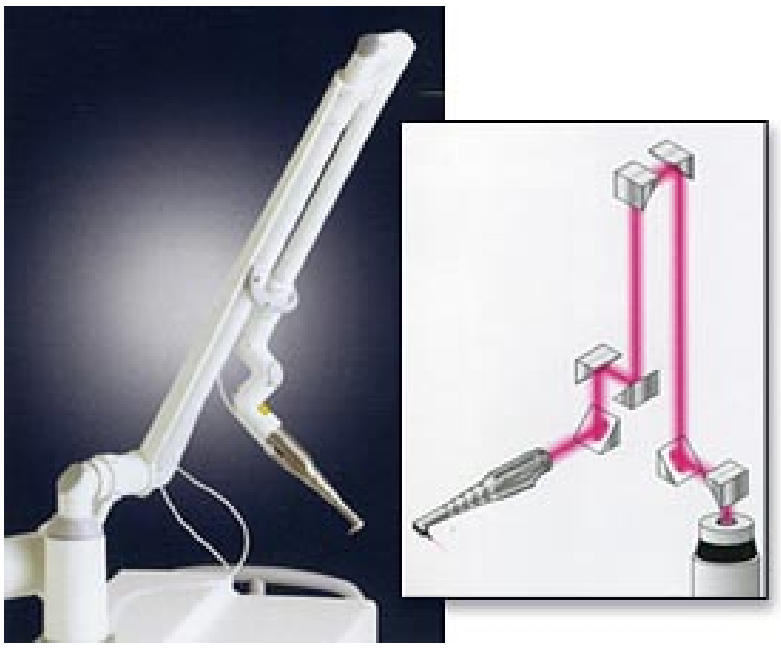

Figure 6: An example of an articulated arm with a schematic of its internal guiding system. The articulated arm is a laser beam delivery system consisted of rigid tubes connected via movable joints. At the joints mirrors are placed to steer the beam. Presented in [59].

Commercially available systems using an articulated arm for the delivering system are supplied by WON Technology Co., Ltd. (AVVIO system) and Fotona d.d. to mention some. Images of these laser systems are presented in Figure 7 and are taken from the company's webpage. As is obvious from the images the hand pieces are relatively large and not designed for minimally invasive procedures.

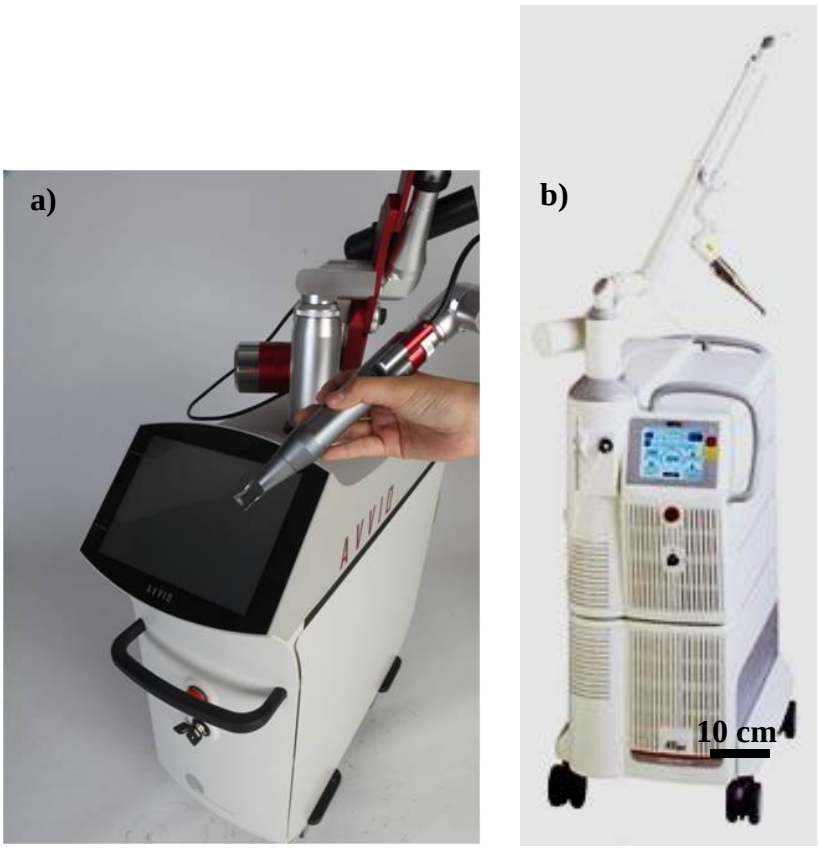

Figure 7: Commercially available systems from: a) WON Technology Co., Ltd. and b) Fotona d.d.

The alternative to the articulated arm is the use of fibres to deliver flexibly radiation from the laser to the patient. The main drive for developing a fibre delivery system is to give increased flexibility and movability to the surgeon and provide a lighter weight system in comparison to the articulated arm systems described above. Also, due to the small fibre dimensions, endoscopic and minimally invasive procedures can be investigated and in some instances are already practiced.

The use of fibres also has the advantage of reducing the access space needed to perform an operation. For example, when a bone is cut it has to be freed from surrounding tissue in order to accommodate the space for a saw [13]. There is less need for a visible guiding laser, as the fibre itself can be used as the guidance device and clearly indicates where the energy will be delivered. However, where the fibre is used inside the body then care has to be taken that the fibre (or the whole endoscope) is not heated higher than 40°C as this can damage the surrounding tissue [22]. Generally, the fibre has to be coated and packaged to be used in medical applications, which can limit the flexibility and increase the overall size.

The bend diameters which have to be achieved by the delivery system are wide ranging depending on the particular endoscopic proceedings, from semi-rigid systems for

nasopharyngeal, adenoidectomy, protoscopy and alike [60] down to 15 cm for endorology [24]. However one could envision that if the minimum possible bend radius were reduced further (in the order of 10's of mm) it would open up the possibility to use laser surgery/endoscopy leading to new proceedings, e.g. in neurology. It is difficult to define the needs for a general endoscope due to the widespread and specific designs for the different operations, however it is clear smaller bend radii could be used in more procedures.

In the following paragraphs the different fibre types for the mid-infrared will be discussed in detail. Fibres have the ability to deliver the mid IR laser radiation in a flexible manner and in doing so overcome some of the issues presented by the use of an articulated arm.

1.2 Solid core fibres for laser delivery in the 3µm region

The first type of fibres to be discussed that have been investigated as potential candidates for flexible delivery of laser light in the 3 µm wavelength region are solid core fibres. Ideally one would like to use established silica solid core fibres and their fabrication techniques to deliver the Er:YAG wavelength. This is however not feasible as silica has high intrinsic losses at wavelength larger than about 2.5 µm and ~50 dB/m at 2.94 µm, as can be seen in Figure 8. Therefore alternative materials have to be used for solid core fibres which can guide at this region, with acceptable losses.

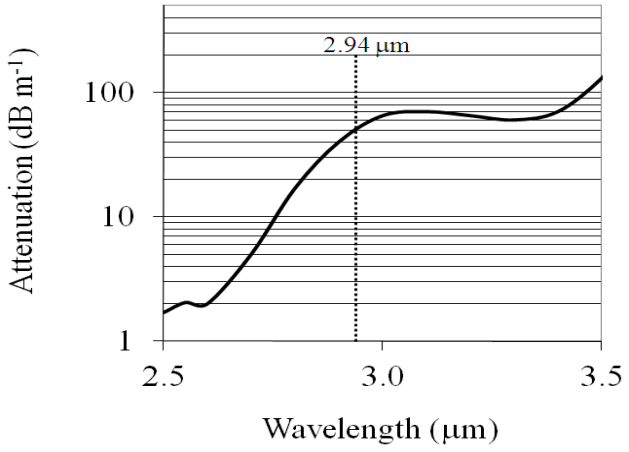

Figure 8: Absorption spectrum of silica (Suprasil F300) in the mid IR, as presented in [61].

Sections §1.2.1 to 1.2.4 describe and assess the suitability and performance of chalcogenide, germanium oxide, fluoride glass and sapphire solid core fibres in the context of delivering laser light suitable for surgery.

1.2.1 Chalcogenide glass solid core fibres

Solid core fibres and recently also microstructured fibres suitable for the mid- and far-infrared wavelength region are drawn from a preform and are based on S (sulfur), Se (selenium) and Te (tellurium) with addition of other elements like Ge (germanium), As (arsenic), Sb (antimony), Ga (gallium) and others, in contrast to silica, silicate, and sapphire fibres which are based around Oxygen. These glasses are generally transparent in the 1-11 µm region (see Figure 9). The sulfide-based fibres transmit from 1-5µm and the telluride-based fibres from 3-11 µm [62, 63] with refractive indices ranging from 2 to >3 which gives rise to a high Fresnel reflection loss of 10 to >25% at each air/glass interface [64]. Also the chalcogenide fibres have reasonable chemical durability and glass stability, but it are not comparable to that of silica fibres.

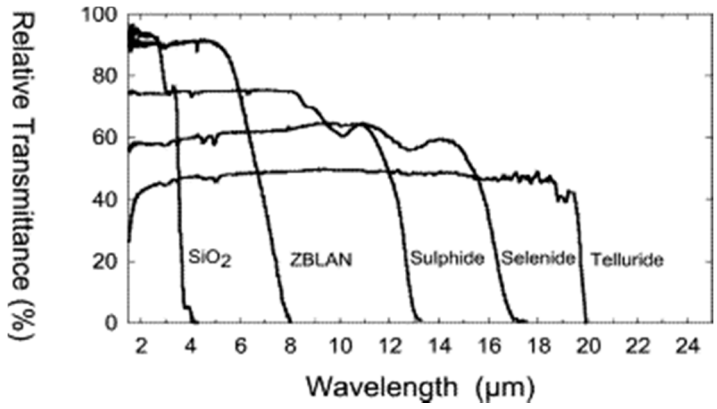

Figure 9: Transmission characteristics for different chalcogenide and oxide glasses, as presented in [65].

The combination of these elements and their relative concentration determines the wavelength at which the material is transparent. In Table 2 different combinations with their optical and mechanical properties are summarised, the data are taken from [66]. All the fibre compositions presented in the Table 2 are capable of transmitting at the relevant medical wavelength of 2.94 µm, however the glass transition temperature is relatively low for these glasses and ranges from 130-220 °C for glasses based on arsenic and 250-400 °C for germanium rich (25-30 at.%) glasses [66].

Table 2: Some compositions and properties of chalcogenide glasses for fibre optics (ρ — density, n — linear refractive index, n^2 — non-linear refractive index, na – not applicable, λ -- wavelength). Presented in [66].

Glasses	**Transmission range, μm (at α = 1 /cm)**	**ρ, kg/m^3**	**T_g /°C**	**T_c– T_g/ °C**	**n (λ/μm)**	**$n_2 \times 10^{-18}$ /m^{2}W^{-1}**
$As_{40}S_{60}$	0.62–9.5	3200	185	–	2.42 (3)	4–6
$As_{40}Se_{60}$	0.85–17.5	4620	178	147	2.83 (3)	14–30
$As_{40}S_{30}Se_{30}$	0.75–12.5	3920	180	–	2.61 (3)	14.5
$As_{30}Se_{50}Te_{20}$	1.23–18.52	5070	140	–	2.9 (5)	> 20
$GeSe_4$	0.75–18	4372	163	–	2.48 (1.55)	13
$Ge_{25}Sb_{10}S_{65}$	0.65–11.0	3400	315	> 200	2.25 (1.55)	2–5
$Ge_{30}As_{10}Se_{30}Te_{30}$	1.2–17.0	4880	260	225	2.8 (10.6)	> 20
$Ge_{21}Te_{76}Se_3$	2–20	5650	160	123	3.4	na
$Ge_{15}Ga_{10}Te_{75}$	2–25	5525	172	≥ 113	3.98	na
$(GeTe4)_{85}(AgI)_{15}$	2–25	5867	135	107	3.3–3.4	na

The losses for different chalcogenide fibres are given in Table 3 [66], with the relevant fibre type and losses at specific wavelength. As can be seen the minimum recorded loss was 13 dB/km at 2.9 μm are (see Figure 10) in a multimode fibre [67], which had an core/cladding diameter of 500/550 μm. The fibre was drawn using the double crucible method (see §5.1) and using additional purification operations oxygen content and heterophase impurity inclusions was reduced as far as possible [67].

Table 3: Minimum optical losses in the best samples of chalcogenide glass fibres (methods of fibre drawing: DC — double crucible, SC — single crucible). Presented in [66]

Fibre glass composition (core/clad)/atomic%	Type of fibre (method of drawing)	Minimum optical losses β/dBkm^{-1} (λ/ μm)	Optical losses at laser wavelengths/dBkm^{-1}				
			2.08 μm	2.9 μm	3.7 μm	5.6 μm	10.6 μm
$As_{40}S_{60}/As_{38.7}S_{61.3}$	Multimode(DC)	12 (3.0)	23	13	17	75	–
As–S/As–S	Single-mode(DC)	100 (2.1–2.2)	140				
$As_{38}S_{25}Se_{37}/As_{38}S_{27}Se_{35}$	Multimode(DC)	60 (4.8)	1000	3800	400	200	–
$As_{40}Se_{60}$/-	Mono-index(SC)	76 (4.2)	160	160	80	85	650
$As_{30}Se_{50}Te_{20}$/-	Mono-index(rod)	40 (6.6)	4000	950	380	160	3500
$GeSe_4$/-	Mono-index(rod)	100 (5.9)	300	500	320	180	–
$Ge_2As_{38}Se_{40}Te_{20}$/ $Ge_2As_{36}Se_{44}Te_{18}$	Multimode(DC)	150 (6.6)	6500	2000	1200	600	3600
$Ge_{9.9}As_{28.9}Se_{38.1}Te_{23.1}$/ $Ge_{10.2}As_{28.8}Se_{36.7}Te_{22.3}$	Single-mode(DC)	1500 (3.1)	7500	2000	2200	6000	–

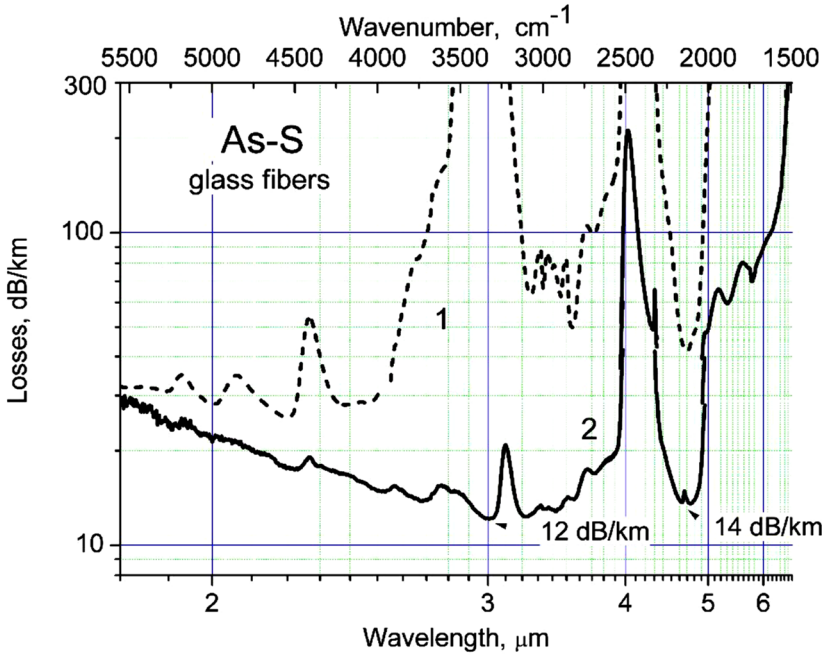

Figure 10: Optical loss spectra of As-S fibres. Presented in [67].

Recent publications present single mode guidance in solid core and microstructured (§1.3.4) chalcogenide fibres. Conseil et al. [68] achieved this at a wavelength of 9.3 μm in a step index fibre as shown in Figure 11, there was no information given on the guidance at 2.94 μm or the powers/energies that could be delivered. Fibres produced by the NRL [63] showed that they could deliver sufficient energy densities for ophthalmic surgery (1-2 mJ) through a sulfide based fibre, the power density achieved was 1.07 GW/cm^2 (Figure 12), the publication does not gives information on the laser parameters.

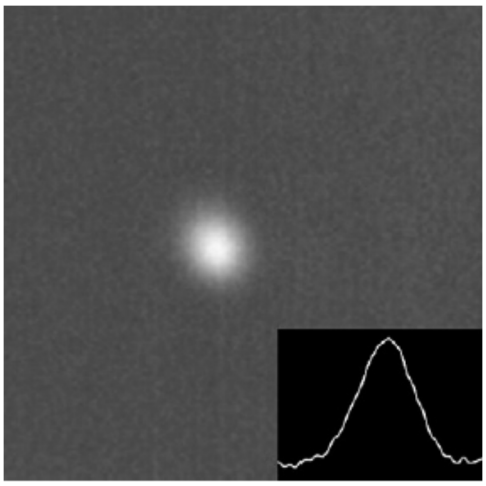

Figure 11: Near-field imaging of a step index chalcogenide fibre at 9.3 µm, guiding a single mode. Presented in [68].

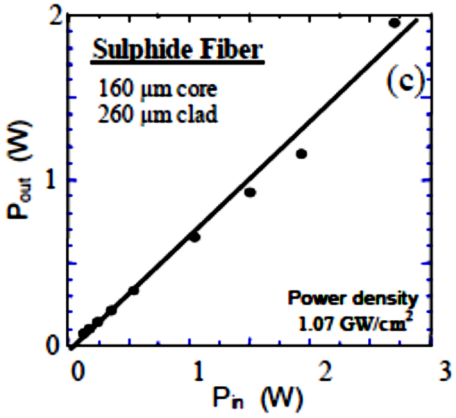

Figure 12: Pulsed high energy laser transmission in the 2-5 mm region. Presented in [63].

Chalcogenide fibres are now commercially available e.g. Fibre Photonics Ltd. and Newport Co., with losses of ~2.1 dB/m and core/cladding diameters of 200-500/300-600 µm, which according to the manufacturer are "capable of Er:YAG power delivery" of 1W for continuous wave [private communication with Gary Colquhoun from fibre Photonics Ltd.].

1.2.2 Germanium oxide fibres

Germanium oxide (GeO_2) is a material for solid core fibres that can guide in the 3 µm wavelength regime. These fibres have a higher damage threshold compared to fluoride glasses (see § 1.2.3), however their glass transition temperature is relatively low, at 680 °C, when compared to silica or sapphire [69].

Papagiakoumou et al. [69] were the first to evaluate the attenuation and output beam profile for this type of fibre using a free-running and Q-switched Er:YAG laser.

The fibres used were 1.4 m and 1.5 m long and had a 450 µm and 250 µm core, respectively. To avoid damage to the fibre, the maximal pulse energy was set to 10 mJ (15 ns pulse duration) in the Q-switched mode and 20 mJ (80 µs pulse duration) in the free-running mode. The attenuation for the two fibres was measured as 0.60 dB/m and 0.75 dB/m for the 250 µm and 450 µm core diameter fibre, respectively. The measurements are shown in Figure 13. The fibre was not damaged at these energies and did not show any significant increase in attenuation if bend down to a curvature of 25 $m^{-1.}$

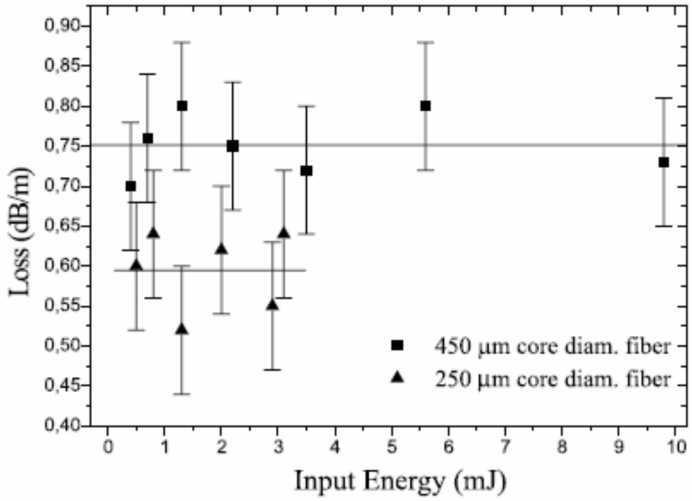

Figure 13: Attenuation of Q-switched Er:YAG laser energy as a function of the laser input power for 250 µm and 450 µm core diameter straight germanium oxide fibres. Presented in [69].

An investigation of the output beam profile for these two fibres showed that the output profile changed from a TEM_{00} mode to multimode character even if the fibre was held straight, with the highest portion of the energy in the centre of the beam profile. An example of the output beam profile for the 250 µm core diameter fibre in Q-switched and free-running mode is given in Figure 14. The authors also concluded that the output beam profile was highly sensitive to changes of the fibre output face.

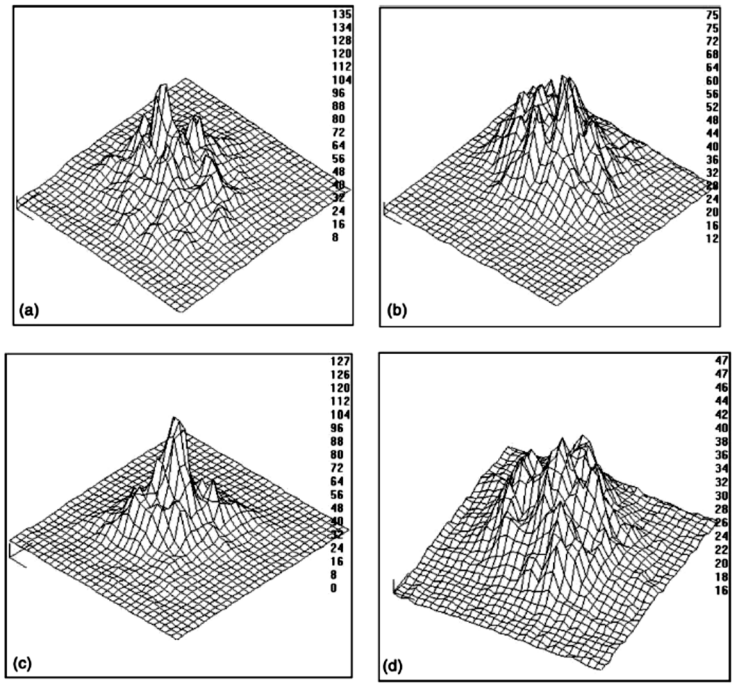

Figure 14: 3D beam profile of the Q-switched Er:YAG laser, at the output of the 250 µm fibre: (a) in straight; (b) in bending conditions. 3D beam profile of the free-running Er:YAG laser, at the output of the 250 µm fibre: (c) in straight and (d) in bending conditions. Presented in [69].

Germanium oxide fibres have been showed in tissue ablation trials as demonstrated by Scott et al. [70] on porcine ureteral tissue. However, the fibre had to be protected by an endtip, which will be described in more detail in §1.4.

1.2.3 Heavy metal fluoride glass fibres

The use of heavy metal fluoride glass fibres for the mid-IR was first proposed and shown by Poulain et al. [71] in 1977. The general heavy metal fluoride glass fibres are based on ZBLAN (ZrF_4–BaF_2–LaF_3–AlF_3–NaF), i.e. they are composed of a mixture of zirconium, barium, lanthanum, aluminium and sodium fluorides. This leads to a low refractive index of n = 1.5.

Recent publications showed attenuations as low as 0.13 dB/m for a 620 µm core diameter ZBLAN fibre using a free running Er:YAG laser and 0.11 dB/m if a Q-switched Er:YAG laser was used [72]. The fibres showed a minimal dependence of the loss if they were bent down to a bending radius of 10 cm, as shown in Figure 15.

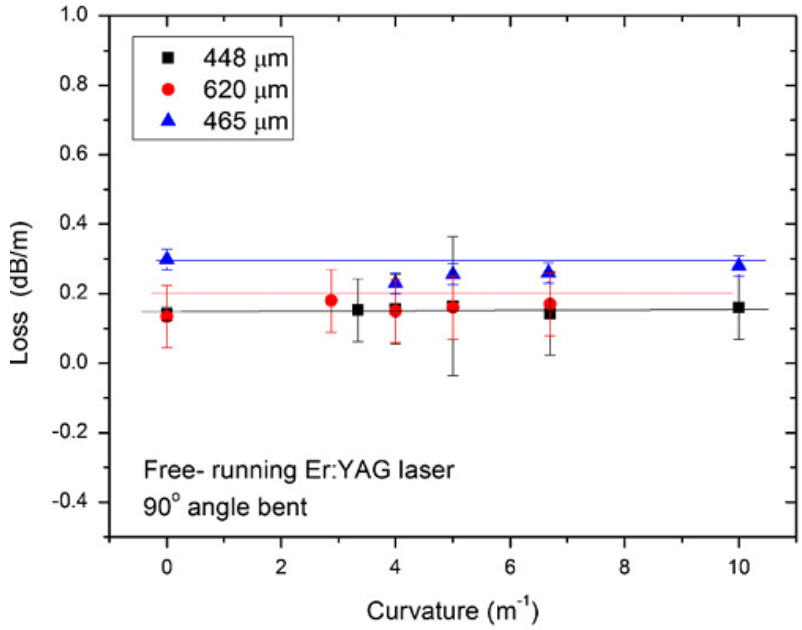

Figure 15: Attenuation of free-running Er:YAG laser energy as a function of the curvature at 90° bending angle, for a ZBLAN glass multimode optical fibre as presented in [72].

However the output beam profile did change with bending as is usual for a multimode fibre, and shown in Figure 16.

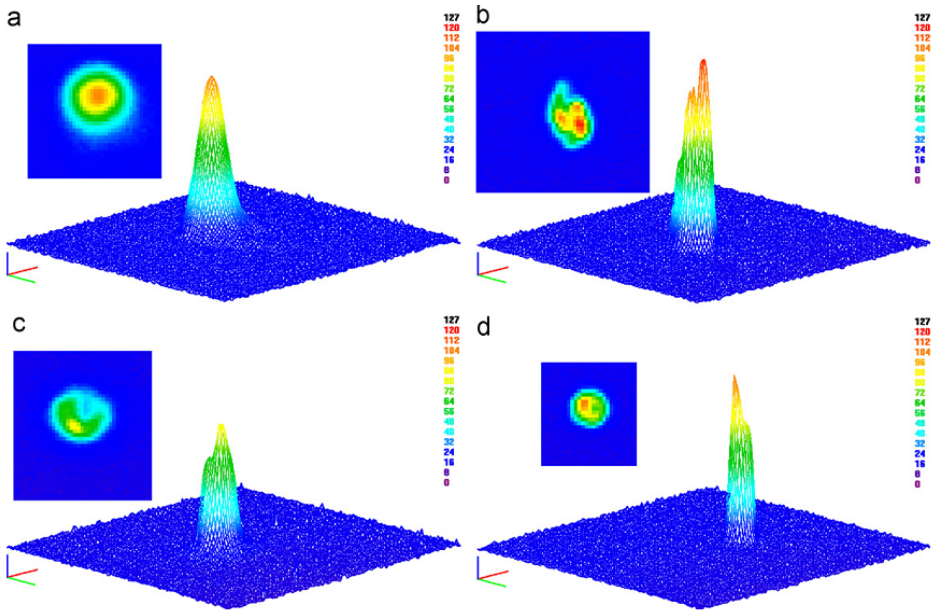

Figure 16: Beam profiles of Q-switched Er:YAG laser beam: (a) after the pinhole 200mm diameter; (b) at the output of the ZBLAN glass optical fibre, with core diameter 448 µm, of 90 cm length, with coupling lens=10 cm, in straight condition; (c) at the output of the ZBLAN glass optical fibre, with core diameter 465 µm, of 87 cm length, with coupling lens=10 cm, at 90° bent angle with R=20 cm and (d) at the output of the ZBLAN glass optical fibre, with core diameter 620 µm, of 90 cm length, with coupling lens=10 cm, in straight condition. Presented in [72].

Also the fibre experienced degradation at the launching side after extended irradiation (no specification on the timescale was given from the authors) (Figure 17).

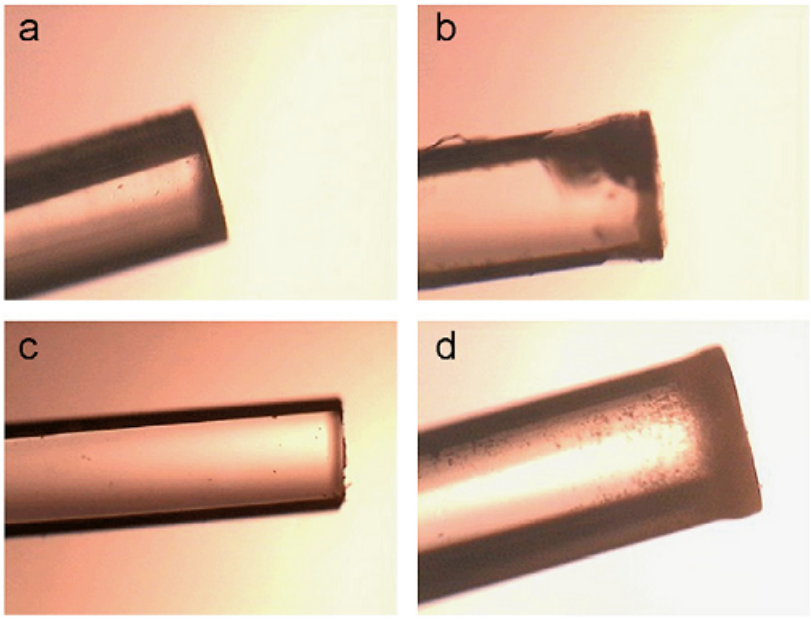

Figure 17: (a) Input end of the 465 µm ZBLAN glass fibre before irradiation; (b) input end of the 465 µm ZBLAN glass fibre after irradiation with Q-switched Er:YAG laser; (c) input end of the 448 µm ZBLAN glass fibre before irradiation and (d) after irradiation with Q-switched Er:YAG laser. Presented in [72].

1.2.4 Sapphire fibres

Sapphire has a low attenuation in the mid-infrared region and can therefore be used at 2.94 µm. The guiding is due to total internal reflection (TIR) which is a well-known process and depends on the reflective indices of the two materials defining the boundary layer; in this case sapphire and air. As the refractive index at 2.94 µm of sapphire is 1.71 and air 1, respectively, the critical angle for TIR is ~35.8°. However these fibres tend to be relatively rigid (compared to silica) due to the stiffness. The stiffness s of a material is defined by

$$s = F/\upsilon \tag{1}$$

where F is the applied force and υ the displacement. The Young's modulus also gives information about a materials properties and is defined as

$$E = \frac{tensile\ stress}{extensional\ strain} = \frac{F/A_0}{\Delta L/L_0} \tag{2}$$

Where A_0 is the area of the applied force, ΔL is the amount by which the length of the fibre changes and L_0 the original length of the fibre.

They can be produced by laser heated pedestal growth (LHPG) [73], where a fibre is drawn from a rod. A schematic diagram of this fabrication technique is shown in Figure 18. A source rod is placed into the focal spot of the spherical mirror, due to the CO_2 laser radiation the rod tip starts to melt and produces a melt pool, into which a single crystalline

seed is inserted and pulled out again. The molten sapphire re-crystallises into a single crystalline structure onto the seed, becoming a single-crystalline fibre. The source rod has to be fed into the focal spot to replenish the volume of molten material [74].

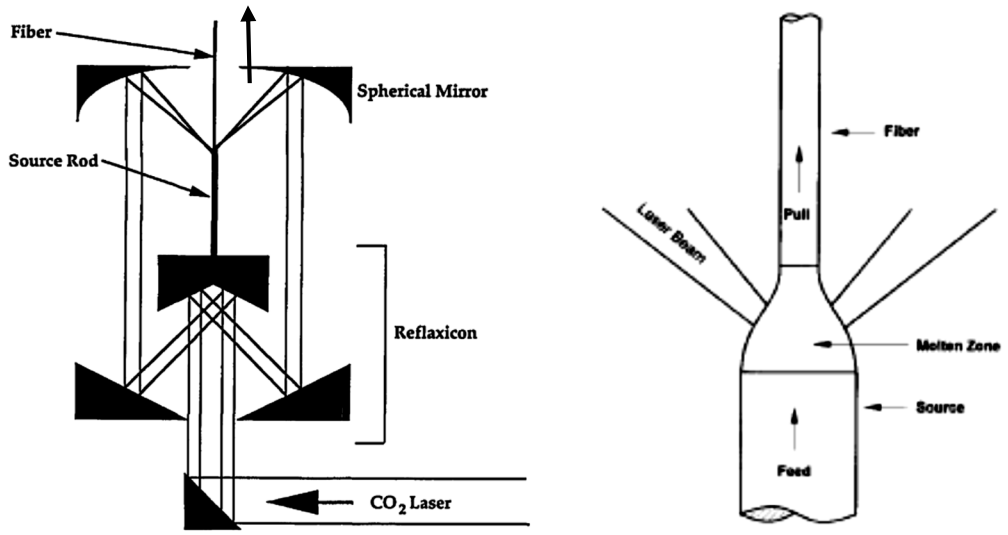

Figure 18: Laser heated pedestal growth (LHPG) technique for the production of sapphire fibres. A source rod is molten locally using CO_2 laser radiation in which seed crystal is inserted and pulled out again. The molten sapphire recrystallises into a single crystal fibre. Right hand image presented in [74] and left hand image presented in [75].

The first fibres reported had an attenuation of >1 dB/m [76] at 2.94 µm. Fried et al [77] could show that pulses up to 18 mJ could be delivered with losses for free-running and Q-switched Er:YAG lasers of 0.4 ± 02 dB/m and 0.6 ± 02 dB/m, respectively. The fibre was 1 m long and held straight during their experiment and no damage to the fibre was seen. Sapphire fibres showed signs of damage at an energy density of ~1.3 kJ/cm^2 [78] at the input end and were reported to deliver high pulse energies of up to 600 mJ through a 340 µm diameter sapphire fibre [75]. More information on the tested LIDT for different sapphire fibres was published by Nubling et al [75]. In the same publication the output beam profile for a 300 µm single-crystal fibre was investigated and it was concluded that the output beam profile was strongly dependent on the input beam profile. If a highly multimode profile was launched into the fibre, the exiting beam profile was also highly multimode, however coupling into lower order modes occured so that the beam profile fits a Gaussian envelope, effectively leading to a beam cleaning. Input and output beam profiles for 100 mw and 10 W input powers are presented in Figure 19.

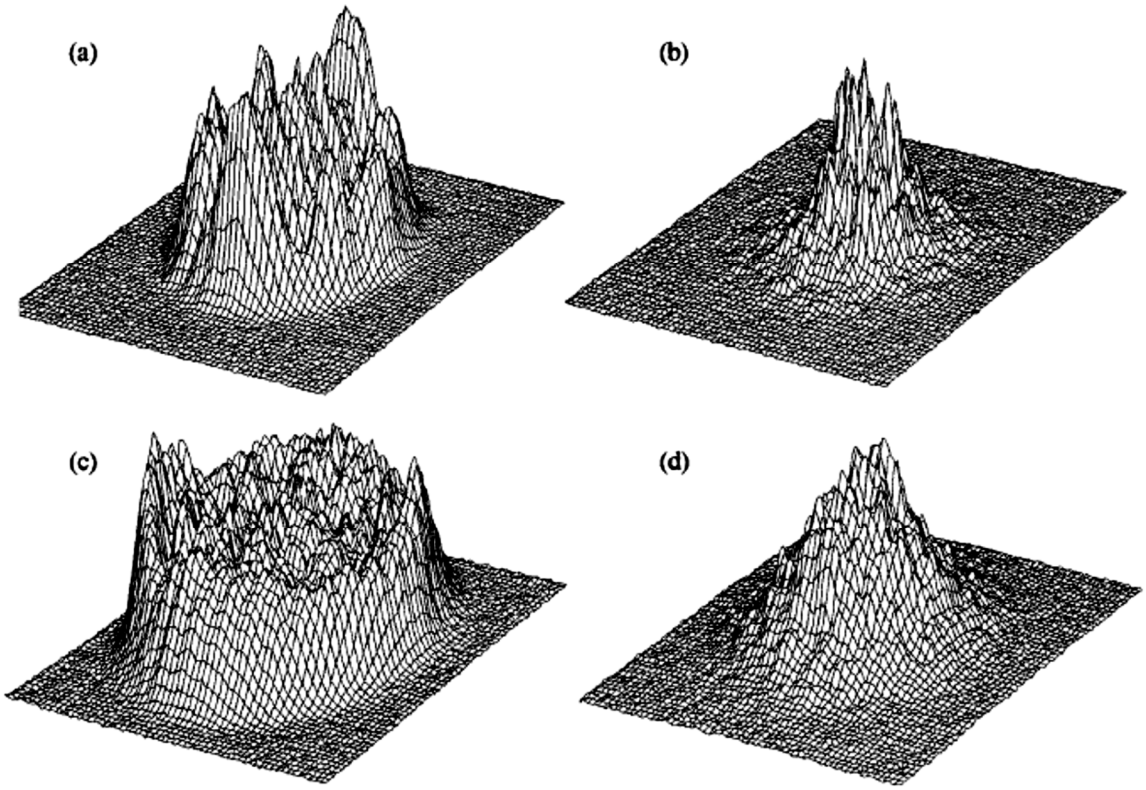

Figure 19: Multimode beam profiles of an unapertured Er:YAG laser beam at 100 mW: (a) into; (b) exiting a single-crystal sapphire fibre and at 10 W; (c) into and (d) exiting the fibre. The total loss of this fibre when measured with the apertured beam was ~ 0.4 dB/m. Presented in [75].

Alternatively if a single mode like profile is coupled into the fibre it will preserve its shape through the fibre, with a slight beam diameter decrease, as seen in Figure 20. However this beam preservation and cleaning, as seen in Figure 19, is only valid if the fibre is low loss and has a low scattering inside the fibre. A fibre with a loss of ~0.8 dB/m will produce a highly multimodal beam output even if the input beam profile is single mode, as shown in Figure 20a. The output of this fibre is presented in Figure 21. It should be noted that all the fibres were held straight during these experiments.

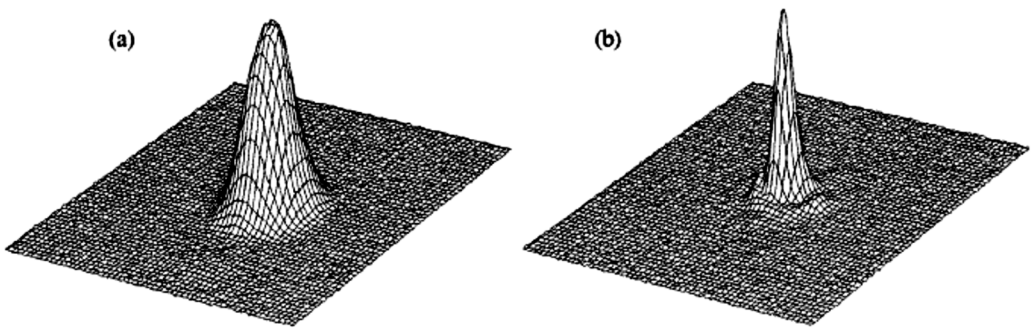

Figure 20: Near-single-mode beam profiles of an Er:YAG laser at 100 mW with a 2-mm aperture placed in the cavity: (a) into and (b) exiting a single-crystal sapphire fibre. Presented in [75].

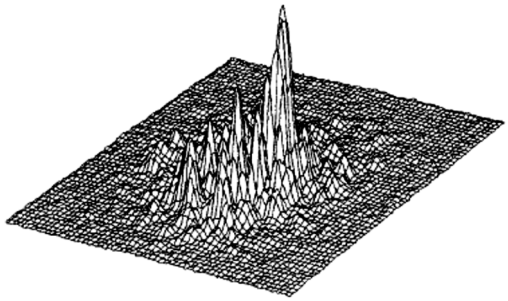

Figure 21: Multimode output from a sapphire fibre having higher scattering losses with a near-single-mode Er:YAG laser input beam at 100 mW. The total loss of this fibre when measured with the apertured beam was ~0.8 dB/m. Presented in [75].

1.2.5 Hollow or leaky waveguides

Hollow wave guides (HWG) or also called "leaky" waveguides [79] consist of tubes made of glass, plastic or metal with an inner coating. In most waveguide designs these coatings consists of Ag (silver) and a dielectric material like AgI (silver iodide) [80], COP (cycling olefin polymer) [79] or more recently PC (polycarbonate) [81]. The coating with a dielectric material reduces the losses due to increased reflection; this is a result of constructive interference effects. However as Bledt et al. showed, it is not necessary to apply the dielectric coating to have a guidance [82]. Figure 22 shows the cross-section of a typical HWG with and without an inner dielectric coating. These fibres have the advantage of a very simple structure, even when compared to the HC-NCF described above, which makes the design and fabrication relatively easy.

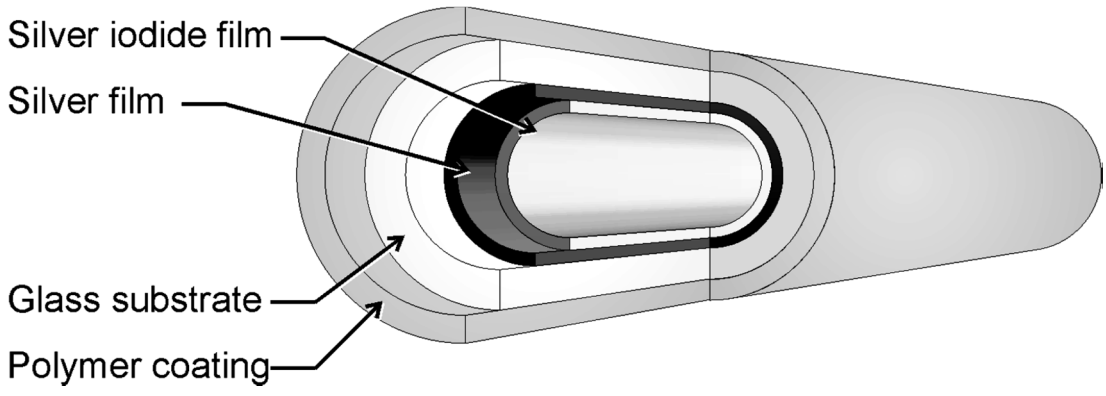

Figure 22: Cross-section of a HWG consisting of a glass tube with inner layers of silver and silver iodide and coated with a protective polymer layer, as presented in [83].

The theoretical calculation using wave and ray optics of HWGs was established by Marcatili and Schmeltzer et al. in 1964 [84], since then a significant amount of research has concentrated on the optimisation of these fibres. By adjusting the layer thicknesses

the guided wavelength can be selected, which makes these fibres easy to adapt for new applications. One of the main applications is in the medical field, as these fibres can operate in the 2.94 µm and 10.6 µm regime which are both important for medicine.

However these fibres transmit in a multimode manner, leading to mode mixing and more importantly high bend sensitivity $\alpha_{bend} \propto a^3 / R$ where a is the core size and R is the bend radius [78]. The bend sensitivity also leads to an appreciable change in the output beam profile with fibre bending, which can result in limitations for certain applications. Recently these fibres have shown a single mode guidance at 10.6 µm [85], which reduces the beam profile dependence on the bending. The attenuation is also highly dependent on the surface roughness σ ($\alpha \propto \sigma^2$) [78] of the different layers, so that extreme care has to be taken to produce a smooth layer and layer interface. Finally the attenuation is dependent on the core diameter a as $\alpha \propto 1/a^3$. This was demonstrated by Matsuura et al. [86] for two different wavelengths (2.94 µm and 10.6µm) and is presented in Figure 23. It has to be noted that the measured losses for the Er:YAG wavelength are significantly higher than the calculated ones. This is due to increased scattering losses at shorter wavelength and the multimode behaviour of the laser source used [80].

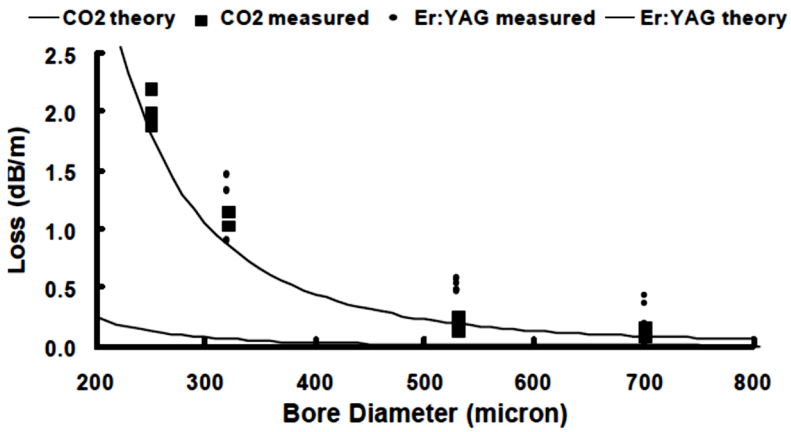

Figure 23: Losses of straight HWGs depending on the bore diameter as presented in [86].

There are different methods of fabricating the fibres: physical vapour deposition, electroplating, liquid phase formation and sputtering. The most common technique is the wet-chemistry process as schematically shown in Figure 24. Using this process the fibre length which can be produced depends on the inner diameter of the fibre and varies from ~1 m for a diameter of 250 µm [87] and 3-4 m for a diameter of 1000 µm [80].

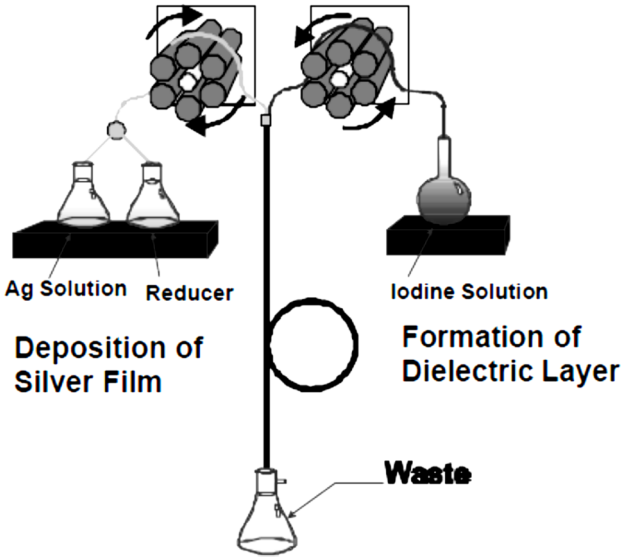

Figure 24: Schematic of a wet chemistry production of a HWG, as published in [80].

The first HWGs for the Er:YAG wavelength were presented by Matsuura and Miyagi [86] and had a core diameter of 1000 µm with losses of around 0.4 dB/m, as can be seen in Figure 25. The same figure also shows the bending losses for the waveguide.

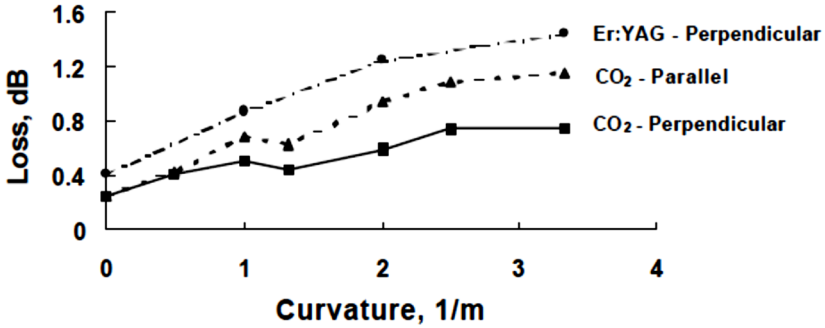

Figure 25: Bending losses of HWG's for CO_2 and Er:YAG wavelength as presented in [86].

The fibres have high power handling capability as presented in [80], 8 W average power could be delivered through a 1000 µm core HWG.

The output beam profile is bend sensitive due to coupling into higher order modes, the amount of supported modes is dependent on the core diameter, the surface roughness and the refractive index difference of the material combination used. An output beam profile for a 530 µm core diameter HWG is shown in Figure 26.

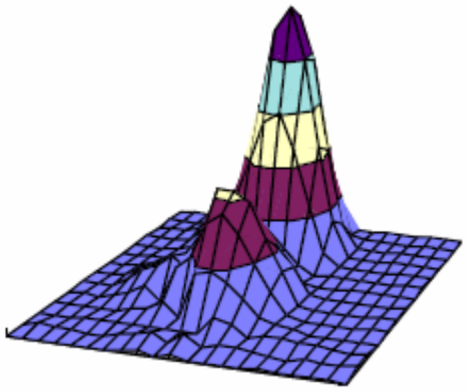

Figure 26: Output beam profile for a 530 µm core diameter HWG, presented in [80].

Recent developments of HWGs are concentrating on the fabrication of smaller bore diameters to increase their flexibility; also longer fibres are drawn to overcome the limitation of 2-3 m that is reached for the usual fabrication process. Matsuura et al. [88] were able to fabricate a Pyrex-glass hollow fibre with an inner diameter of 280 µm using the glass-drawing technique in which the Ag and dielectric layer are applied on the outside of the fibre, which enables longer fibres (>20 m). However, at around 3 µm the losses for a 15 cm length piece of fabricated fibre were in the order of 5 to 10 dB, no energy handling capability was presented and the fibres were mechanically fragile. Namec et al. [87] showed a HWG with an inner diameter of 250 µm and a transmission of 77% for 10 cm long fibre piece, however the output beam profile changed with the input power and with bend of the fibre.

1.3 Microstructured and photonic crystal fibres

1.3.1 Photonic Crystal Fibres (PCFs)

A radical new fibre geometry (compared to traditional solid core fibres discussed above) was first proposed in the mid-1990s [32] the Photonic Crystal Fibre. These fibres led to a step change in fibre based technology and are a viable solution for delivery of lasers for surgical applications when configured with a hollow core. This section will describe the fundamental guidance principals for this relatively new fibre class and the following sections will focus on the hollow core variants which have the greatest potential for delivery of Er:YAG laser radiation at levels applicable to surgical applications.

The first description of the photonic bandgap effect was by Yablonovich [89] and John [90] independently in 1987, both studied the spontaneous emission control and

localisation of light in novel periodic materials. The first fibre was produced by Russell et al. in 1996 [91]. The name of the photonic crystal was created to describe periodical materials in which specific frequency intervals of electromagnetic waves could not propagate irrespectively of their propagation direction. These forbidden frequency bands are called photonic bandgaps.

There are several different classes of photonic crystal fibres (PCF), depending on the literature also called microstructured fibres (MSF) [92, 93] or microstructured optical fibres (MOF) [80]. Some of the examples are presented in Figure 27. The two main classes are divided into fibres which guide due to a modified total internal reflection principle or due to a (real) photonic bandgap effect. A diagram of the different classes and sub-classes are presented in Figure 28, from [94], the denotation of this work is based on this. As the fibres used for this work are belonging to the sub-class of the hollow core fibres, the theoretical background will be mainly concentrated on the photonic bandgap fibres, which from now on are referred to as hollow core-photonic crystal fibres (HC-PCF).

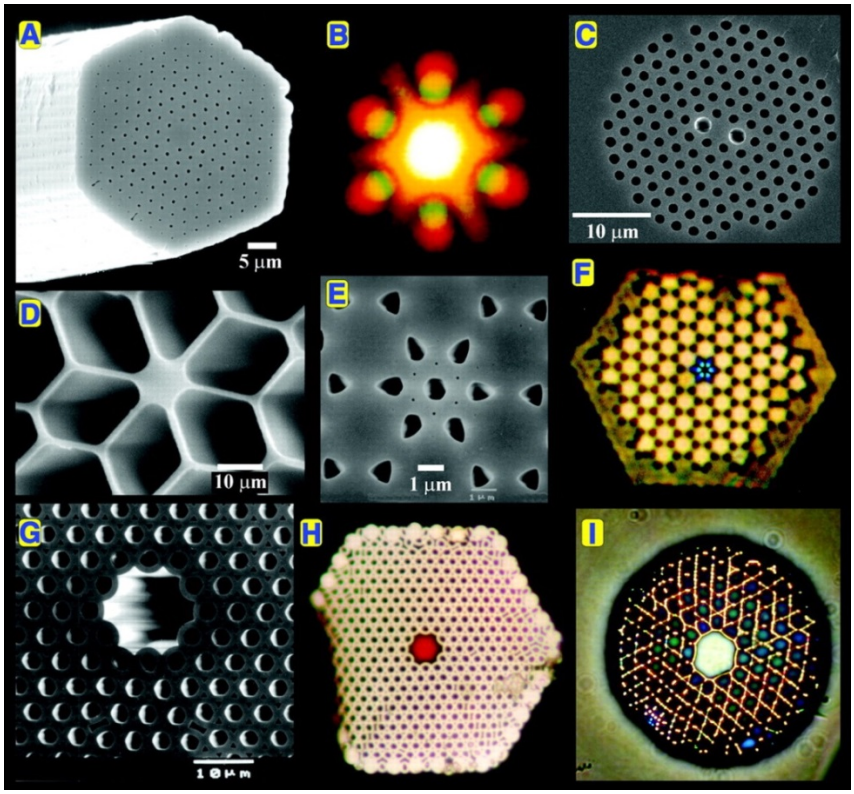

Figure 27: An assortment of optical (OM) and scanning electron (SEM) micrographs of PCF structures: (A) SEM of an endlessly single-mode solid core PCF; (B) Far-field optical pattern produced by (A) when excited by red and green laser light; (C) SEM of a recent birefringent PCF; (D) SEM of a small (800 nm) core PCF with ultrahigh nonlinearity and a zero chromatic dispersion at 560-nm wavelength; (E) SEM of the first photonic band gap PCF, its core formed by an additional air hole in a graphite lattice of air holes; (F) Near-field OM of the six-leaved blue mode that appears when (E) is excited by white light; (G) SEM of a hollow-core photonic band gap fibre; (H) Near-field OM of a red mode in hollow-core PCF (white light is launched into the core) and (I) OM of a hollow-core PCF with a Kagomé cladding lattice, guiding white light. Presented in [95].

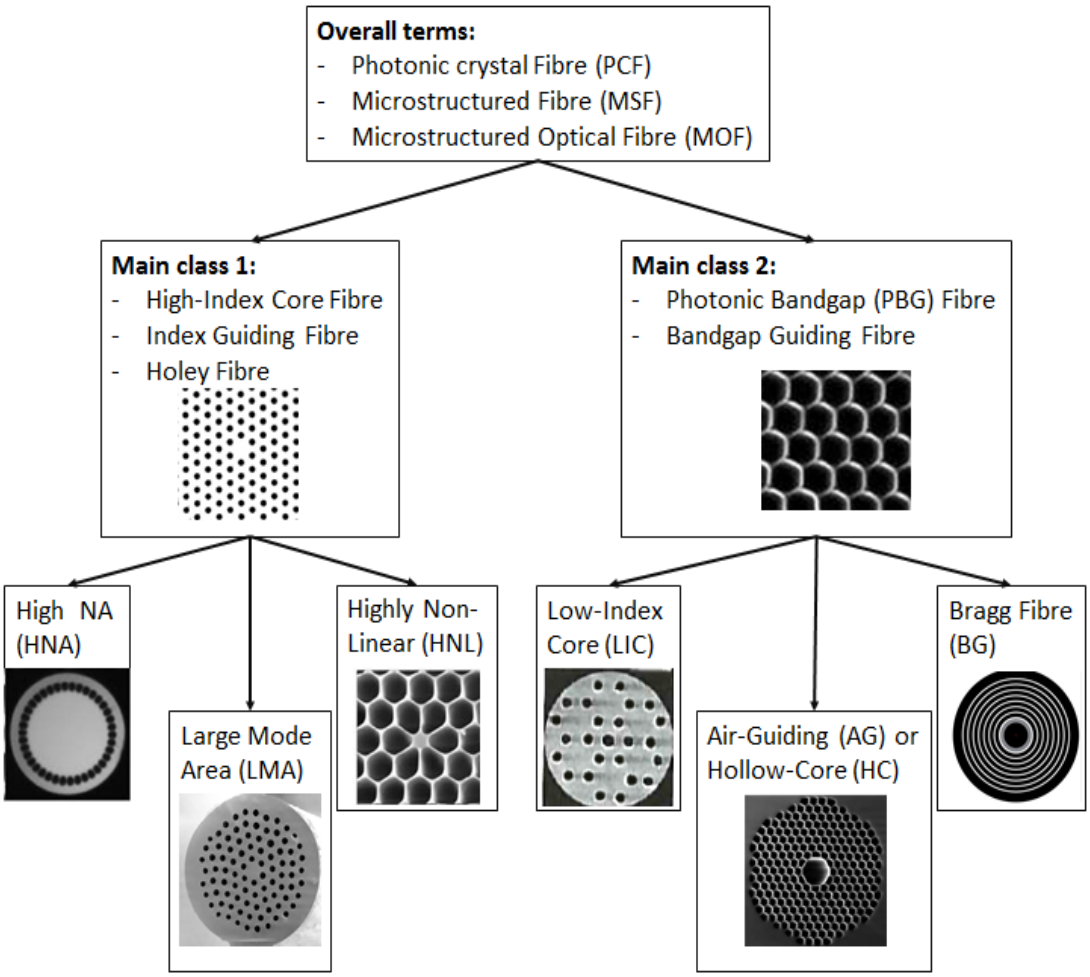

Figure 28: The diagram is showing the mostly common used terms and typical structures for the different types of photonic crystal fibres. The images and diagram are reproduced according to [94] the same nomeclature is used in this work.

The guidance of fibres ("traditional" solid core and PCF) is determined by the propagation constant (also called wavevector) β and additionally, in the case of PCF, the internal hole spacing (pitch) Λ. For fixed frequencies the maximum allowed value of β is set by $kn = \omega n / c$ where k is the wavenumber, ω the frequency, n the refractive index of the region of interest and c the speed of light in vacuum. This leads to a free propagation of the light in regions where $\beta < kn$ and forbidden areas where $\beta > kn$. For the case of the solid core fibre the condition of $kn_{cl} < \beta < kn_{co}$ where n_{cl} is the refractive index of the cladding and n_{co} the refractive index of the core, has to be fulfilled to have guidance due to total internal reflection (TIR), where n_{cl} and n_{co} the refractive index of the cladding and core region, respectively. Commonly a propagation diagram is used to show the regions in which fibres are guiding; such a diagram is presented in Figure 29 for conventional solid core fibres and for a PCF with an air-filling fraction of 45% and a triangular lattice of air holes in silica. The air-filling fraction is defined by the d/Λ, where

d is the diameter of the air-holes of the cladding structure. Regions in black are forbidden bands/zones, so that there is no propagation of light.

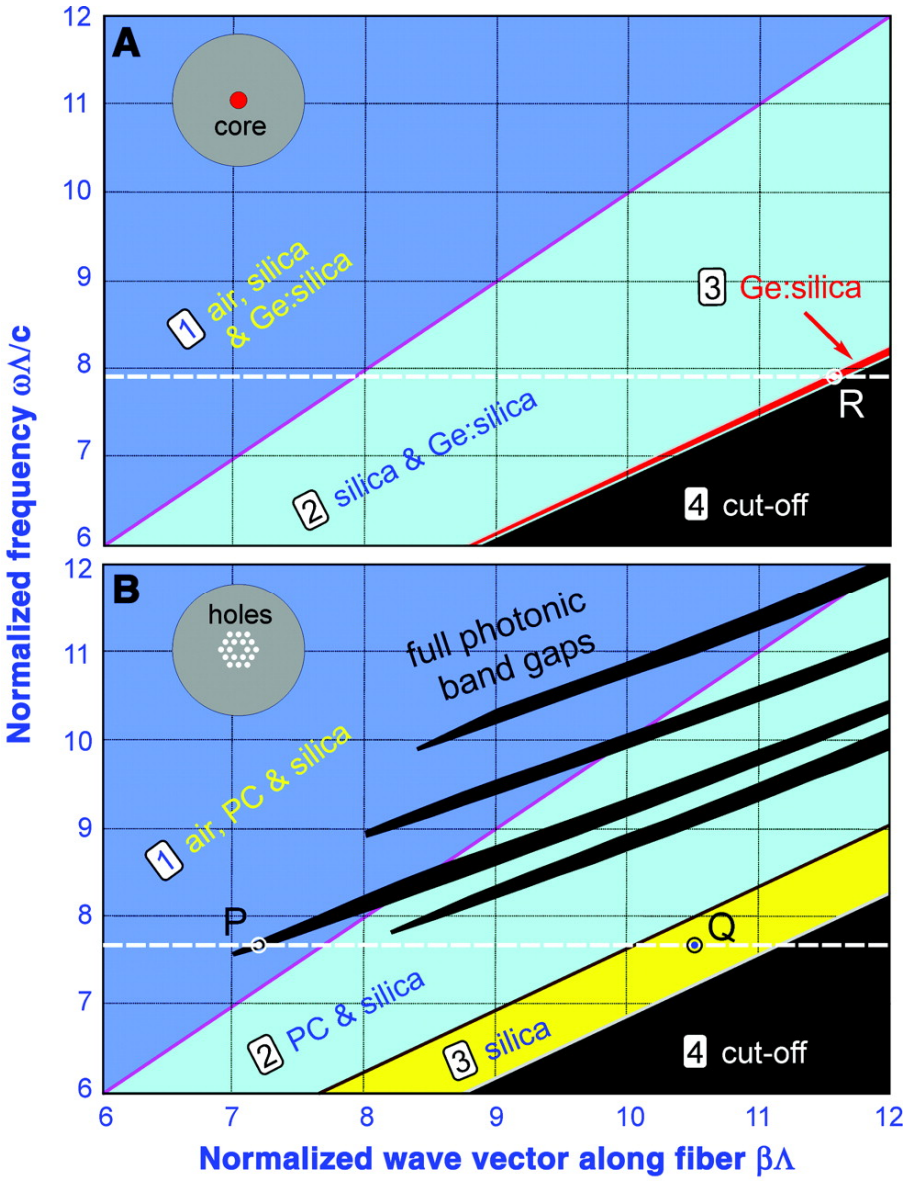

Figure 29: (A) Propagation diagram for a conventional single-mode fibre (see schematic in the top left-hand corner) with a Ge-doped silica core and a pure silica cladding. Guided modes form at points like R, where light is free to travel in the core but unable to penetrate the cladding (because total internal reflection operates there). The narrow red strip is where the whole of optical telecommunications operates; (B) Propagation diagram for a triangular lattice of air channels in silica glass with 45% air-filling fraction. In region (1), light is free to propagate in every region of the fibre [air, photonic crystal (PC), and silica]. In region (2), propagation is turned off in the air, and, in (3), it is turned off in the air and the PC. In (4), light is evanescent in every region. The black fingers represent the regions where full two-dimensional photonic band gaps exist. Guided modes of a solid-core PCF (see schematic in the top left-hand corner) form at points such as Q, where light is free to travel in the core but unable to penetrate the PC. At point P, light is free to propagate in air but blocked from penetrating the cladding by the PBG; these are the conditions required for a hollow-core mode. Presented in [95].

In Figure 29 A the region 1 indicates the regions were light can propagate in air, the silica cladding and the Ge; silica core; 2 indicated the region where it can propagate in the

cladding and the core; region 3 is the actual guiding of light inside the core and 4 is the cut-off where no propagation at all is allowed.

In contrast to the solid-core propagation diagram the PCF structure shows full photonic bandgaps in the region of air photonic crystal and silica region; these black regions where no propagation is allowed are sometimes called "fingers" [95]. The yellow region in the diagram represents the region where the light is confined inside the silica core (for solid core PCF), as it cannot propagate trough the photonic crystal (PC) region. At a point like P the light can propagate in air but blocked from penetrating the PC due to a photonic bandgap at this frequency; this are the conditions needed for a hollow core photonic crystal fibre. At these points the guided mode must have $\beta / k < 1$, and the number of supported modes (m) can be approximated by [95]

$$m \approx k^2 \rho^2 (n_{high}^2 - n_{low}^2) / 2 \qquad (3)$$

where n_{high}^2 and n_{low}^2 are the refractive indices at the edges of the photonic bandgap at fixed frequency, and ρ is the core diameter. Since the refractive index difference is usually quite low (a few percent) the hollow core must be sufficiently big for any modes to be guides [96].

A unique feature of this guidance mechanism is that it allows guidance in a low index core (not possible with step index fibres or TIR based PCFs). In particular this enables guidance in an air core which has significant advantages in overcoming limits imposed by material absorption and laser breakdown as is discussed later in §3.6.

An additional advantage of these HC-PCF fibres is that there is a negligible additional loss due to bending [96]. This is particularly important for industrial and medical applications, where the output power and beam profile should stay constant. Conventional fibres have additional losses when bent beyond a critical radius R_C, which depends on wavelength, core-cladding, refractive index difference and, most importantly, the third power of the core radius, a^3 [97]. The bending losses for solid core PCF can be distinguished in the long and the short-wavelength band edge. In the long-wavelength band edge, the ten times higher refractive index difference of the PCF, relative to a conventional fibre, is the reason why it has lower bend sensitivity. In the short-wavelength band edge, the bending introduces a coupling from the fundamental mode into higher order modes, which leak out [98]. But the critical radius of the PCF can be much lower with $R_C \sim \Lambda^3/\lambda^2$ (where Λ is the pitch, and λ is the wavelength) compared to $R_C \sim \lambda$ for conventional fibres.

1.3.2 Silica Hollow Core photonic crystal fibres for mid-IR

As mentioned in the previous paragraph §1.3.1 the concept of a photonic bandgap fibre enables the guidance in a low refractive index region, like air. This has the advantage that the interaction of the laser light with the material is minimised opening up guidance in wavelength regions where the material has high intrinsic losses. This enables power delivery at much higher levels than in solid core fibres of the same material. The first hollow core-photonic crystal fibre (HC-PCF) was demonstrated in 1999 by Cregan et al. [99]. It was made of silica and had an outer diameter of 105 µm with a core diameter of 14.8 µm, the pitch was 4.9 µm (Figure 27e). The transmission of a guided mode was 35% over 40 mm length of fibre. In the telecommunication region (around 1.5µm) there was also a silica fibre presented with an attenuation of 1.2dB/km (conventional fibres have a loss of around 0.15dB/km) [100]. This was a 19 cell HC-PCF and it was determined that the attenuation is dominated by an effect called "surface capillary waves (SCWs)". This is a kind of surface roughness, in the form of frozen waves in the fibre due the fabrication process and results from thermodynamics of the fabrication process. One way to reduce this effect would be to use a 37-cell fibre, i.e. with a much larger core, but these result in a multimode fibre. Also, delivery of high energy nanosecond pulses at 1064 nm has been demonstrated with this class of fibre [101, 102] showing the marked increase in single mode power delivery possible with hollow core guidance.

Initial attempts have been made to fabricate fibres from silica operating beyond the normal transmission limits into the mid-IR region (Figure 8). Recent work has shown a silica fibre produced for the mid IR region, from 3-3.25 µm with an attenuation of 2.6 dB/m at 3.14µm [103]. It was fabricated using the stack and draw method, with the core consisting of 19 missing cells or defects (Figure 30). The outer diameter was 150 µm, with an inner core of 40 µm and a pitch of around 7 µm, leading to a single mode/Gaussian like output beam profile.

Other advantages are that the Fresnel reflections at both ends are mostly eliminated and coupling efficiencies up to 98% can be achieved [104, 105] (this is if the fibre is not sealed using an endtip, as will be described in §1.4 and §6). An additional feature is that the light has a high interaction with the core medium, which can be air or a gas, which has the potential for fibre based gas sensors [106]. Consequently, the fibres reported in [103] were used to demonstrate gas sensing of methane [107, 108].

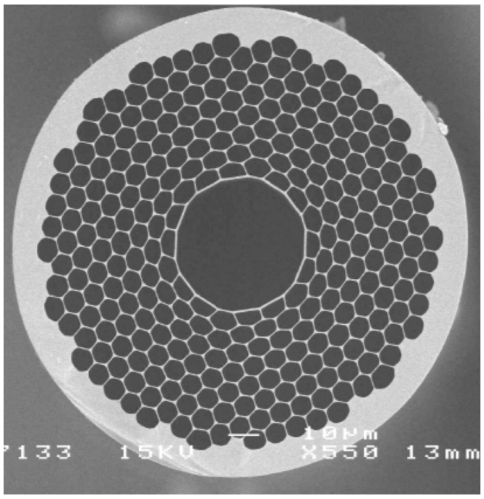

Figure 30: SEM image of a HC-PCF with a core of 19 missing cells as presented in [103]. The fibre was produced from Suprasil F300.

The bend sensitivity of hollow core PCF was measured and explained by different groups and for different wavelengths [109-111]. The overall conclusion was that the fibres are bent-insensitive, which is explained due to the large refractive index change between the core and the cladding structure in the order of $2*10^{-2}$. This leads to a very tight confinement of the guided mode in the core and therefore a robust guidance even through tightly bent fibres.

Due to the promising properties reported in previous studies of such silica HC-PCFs fibres this is the first fibre type that is investigated in this work as a solution for flexible delivery of Er:YAG laser radiation for surgical applications (§3).

1.3.3 Negative Curvature (NCF) and Kagome-lattice type fibres

In 2002 Litchinitser et al. [112] proposed that if the pitch in the photonic bandgap structure is larger than the wavelength and the index of refractive contrast between the core and cladding structure is high, the spectral characteristic of the fibre can be described by the thickness of first high-index layer instead of the pitch of the structure. In such cases the fibre guidance can be described by the antiresonant reflective optical waveguide (ARROW) model [113]. To describe the guidance mechanism, one can consider a simple structure as shown in Figure 31 top, consisting of a low refractive index (n_1) core surrounded by a layer of high (n_2) and low index region. The two interfaces of n_1-n_2 and n_2-n_1 can be considered as a Fabry-Perot resonator (FPR), therefore frequencies which are resonant can propagate in the FPR and exhibit high attenuations, due to coupling into cladding modes. However if the frequencies are antiresonant they exhibit a destructive interference in the FPR and therefore cannot propagate, leading to low attenuations.

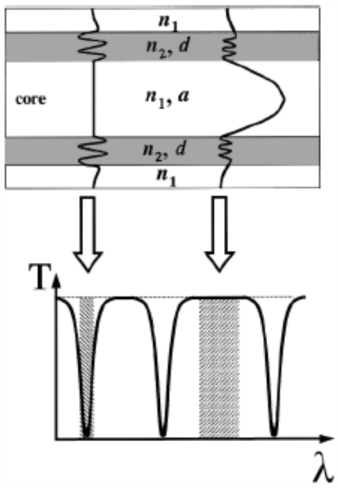

Figure 31: Schematic of an ARROW structure (top) and its transmission spectrum (bottom), as presented in [112].

The antiresonant condition for a given wavelength λ_{res} can be quantified using the following expression [114]:

$$\lambda_{res} = \frac{2}{m}\sqrt{n_2^2 - n_1^2} \tag{4}$$

with m=0,1,2,… the number of supported modes. This guidance mechanism is also used in large pitch Kagome-lattice fibres as shown by Couny et al. [115]. A typical Kagome-lattice is shown in Figure 32 (1).

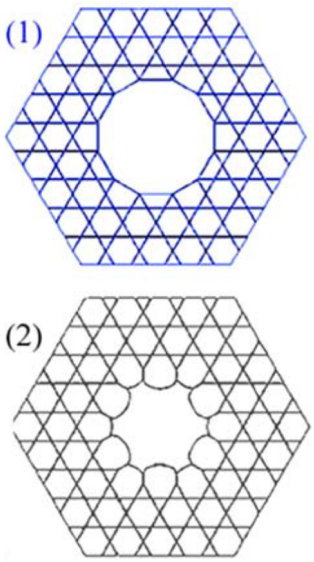

Figure 32: Traditional Kagome-lattice (top), and a Kagome-lattice with a negative curved core (also called hypocycloid core) (bottom) as presented in [116].

The theoretical and experimental understanding of the losses in these fibres was demonstrated by Fevrier et al. [117] in 2010. It was concluded that the lattice structure after the initial core wall is just for support and does not decrease the losses. Also the studs (the connection nodes of the structure elements) increase the losses, as modes can be supported within these studs. Therefore the ideal structure would be a freely suspended cylinder with the right thickness Figure 33a. As this is not practical, the simplest structure would be as seen in Figure 33b.

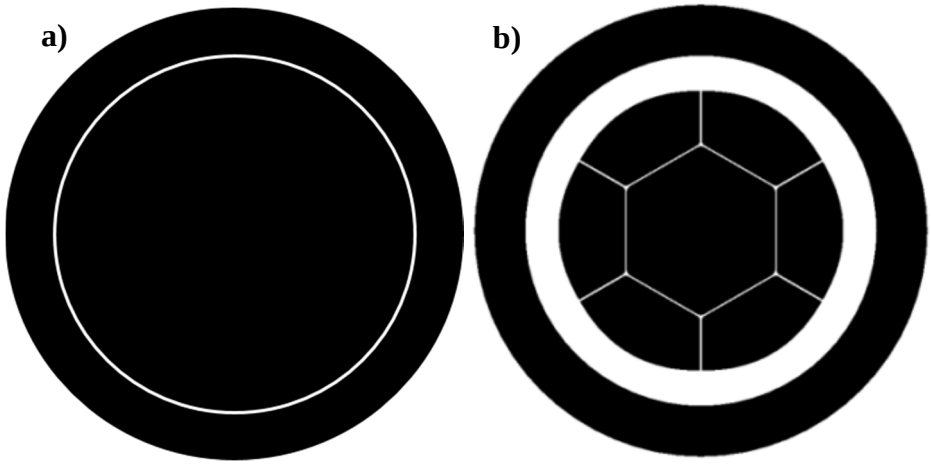

Figure 33: White is silica and black is air: a) Ideal ARROW structure consistent of a freely suspended cylinder and b) Morphology of the minimalist large pitch Kagome-lattice fibre as presented in [117]. This represents the simplest structure which is practically achievable, as a) cannot be fabricated. The scale of this structure is dependent on the desired wavelength and is therefore not included in the schematic.

One year later Wang et al. [116] demonstrated that the a hypocycloid core can reduce the losses of the fibre. A hypocycloid core is shown in Figure 32 (2), in this case the inner wall is curved into the core. The produced fibres and their attenuation can be seen in Figure 34.

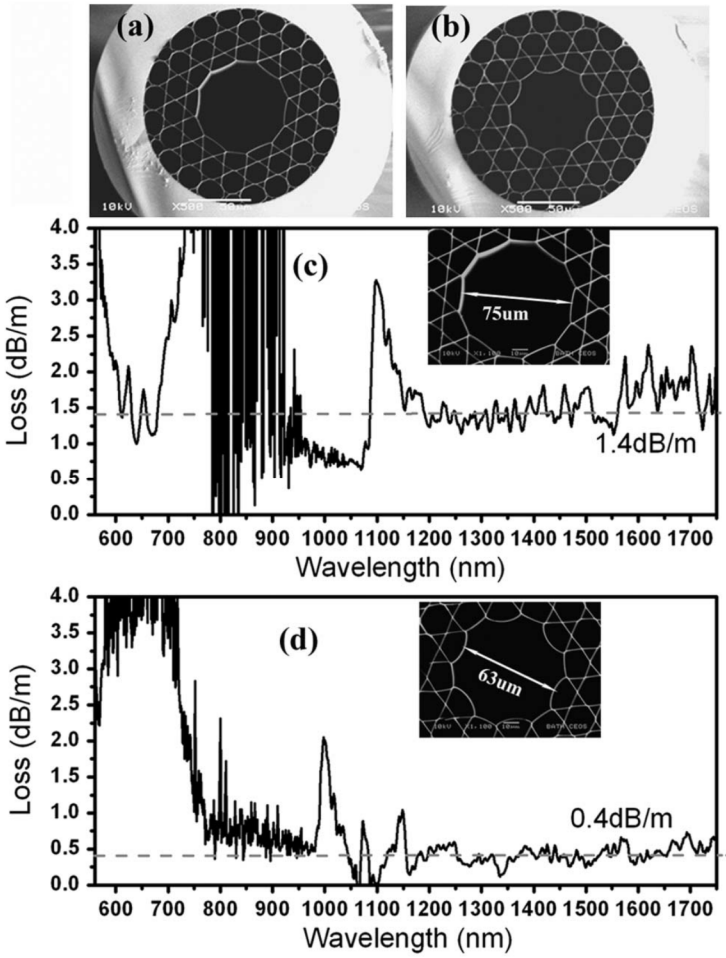

Figure 34: Scanning electron micrographs (SEMs) of seven-cell core and three-ring silica Kagome cladding HC-PCF with: (a) a circular core; (b) a hypocycloid core. Attenuation spectra for the: (c) circular-core and (d) hypocycloid-core Kagome HC-PCF. Insets in (c) and (d) show the detailed SEMs of the core. As presented in [116].

The hypocycloid core decreases the losses by physically moving the studs away from the supported core mode. The term "negative curvature" in this context was first used by Pryamikov et al. [118] to describe the core wall shape, as the inner core wall curvature is opposite to the fibres natural curvature. The cross-section of their fabricated fibre consisted of a single ring structure with negative curvature cores, as seen in Figure 35a. The calculated attenuations are presented in Figure 35b.

The latest publication by Kolyadin et al. [119] could show experimentally that if the capillaries are not in contact with each other, the losses of the fibre can be further reduced. This was to be expected as in this configuration there are no studs which can support modes into which the light can couple.

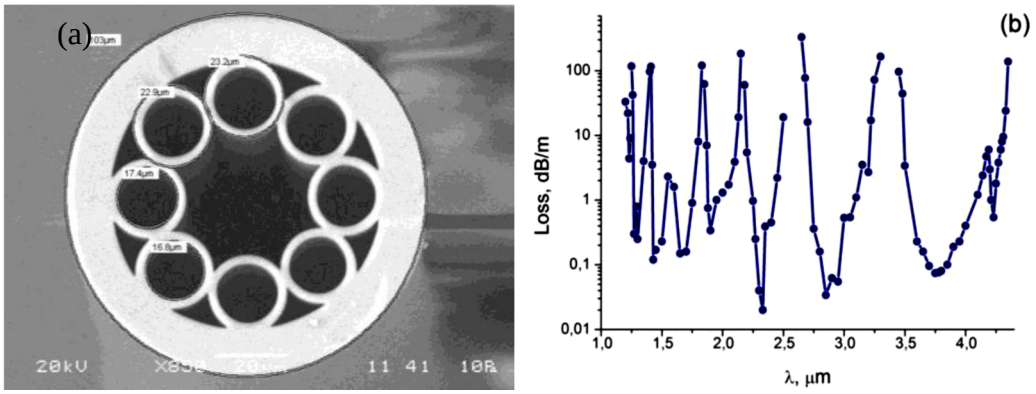

Figure 35: (a) Cross-section of a hollow core micro structured fibre (HC MOF) and (b) attenuation calculation for the HC MOF as presented in [118].

The advantage of this fibre is the simplicity of its design, so that it can be adopted for materials which are harder to work with when compared to silica (e.g. chalcogenide glasses). Kosolapov et al. [120] fabricated a negative curvature fibre (HC-NCF) from a chalcogenide glass, but later turned out to be Ga-La-S-O [121], that can guide at 10.6 µm with attenuations as low as 11 dB/m, this is the first reported MOF that could show guidance in this wavelength regime. The authors hope to be able to reduce the losses of such fibres under 1 dB/m, which would increase the usability of CO_2 for several applications (like medicine) as a low loss flexible guidance could be achieved. The actual impact on medical application has to be seen, as many studies show the advantage of Er:YAG lasers compared to CO_2.

Due to the promising properties reported for NCFs this is the second fibre type that is investigated in this work as a solution for flexible delivery of Er:YAG radiation (§4).

1.3.4 Microstructured chalcogenide fibres

In the recent years many groups have been concentrated on fabricating hollow core fibres out of chalcogenide glasses, due to their optical properties (see §1.2.1) the guidance and optical losses can be reduced at the mid and far IR region.

The first PCF fabricated out of chalcogenide was demonstrated by Monro et al. in 2000 [122]. The fibre was composed of a Ga-La-S glass (gallium lanthanum sulfide) and was assembled in a stack and draw method, no attenuation data was given for this particular fibre, however theoretical calculations predicted that the fibre can guide light from 0.5 – 5 µm. More recent low-loss chalcogenide microstructured fibres have been presented by Coulombier et al. [123-125], using a casting method. Commonly a stack and draw method is used for the fabrication of microstructured fibres, specifically if they

are made of silica. However as was demonstrated by Brilland et al. [126] if this method was used with chalcogenide glass fibres the losses of the fibre were always higher than the bulk material, the author concluded that interfaces between the capillaries have a big impact on the attenuation of the fibre. Therefore they invented a new fabrication technique; in this case a mould, resembling the inverted desired design, made of silica, the chalcogenide glass is purified and heated up to a liquid and poured into the mould (Figure 36). After quenching and annealing the silica is removed from the chalcogenide glass using hydrofluoric acid. This method enables the fabrication of various fibre designs like large or small core MOF and suspended core fibres, as seen in Figure 37.

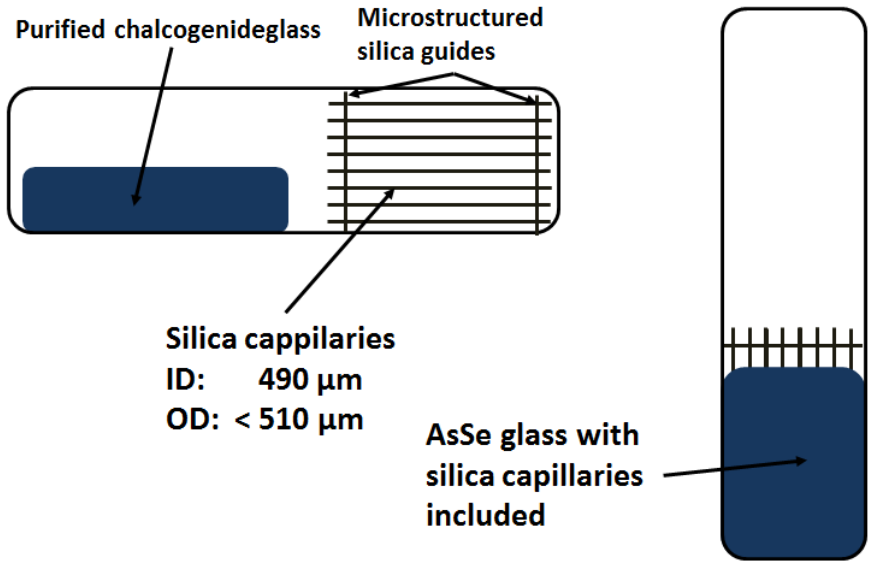

Figure 36: Scheme of the silica mould. The glass is poured into the mould which is then removed. Reproduced from [125].

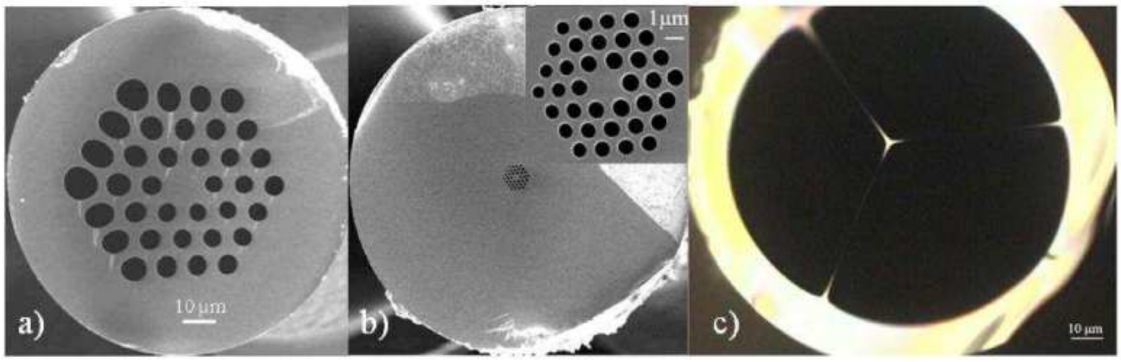

Figure 37: $As_{40}Se_{60}$ fibres: a) SEM micrograph of a large core fibre. The core diameter is 13 µm; b) SEM picture of a small core fibre. The core diameter is around 2 µm and c) Optical microscopy picture of a suspended core fibre. The core diameter is 4 µm. Presented in [125].

These glass in these fibres were highly purified and the (large core) fibre has approximately the same absorption spectrum as the raw material as can be seen from Figure 38, where the attenuation of the raw material is presented on the left and the fibre

attenuation on the right. The losses of the fibre are below 0.5±0.1 dB/m in the window of 3-5µm and between 0.5±0.1 and 1±0.2 dB/m in the range of 1.7-2.7 µm. The absorption band of O-H around 2.9 µm is still existent and of the order of 3 dB/m, also the authors state that the fibre shows no bending losses down to a bending radius of 2.5 cm.

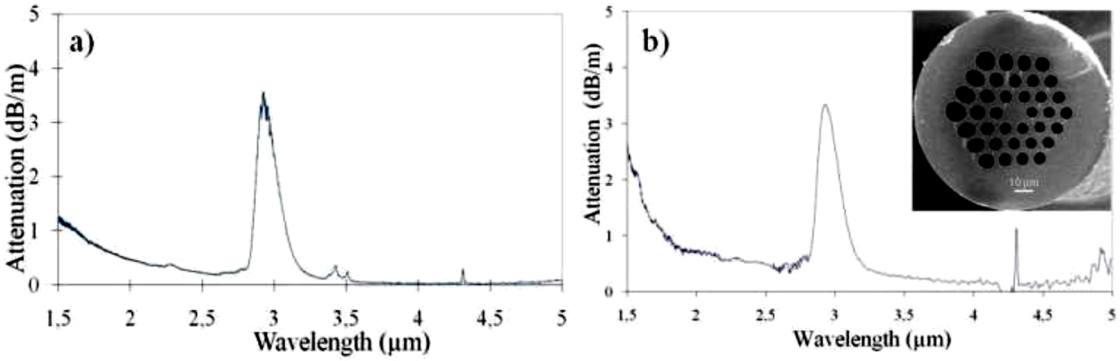

Figure 38: a) Attenuation of the $As_{40}Se_{60}$ glass; b) Attenuation of the core of a multimode $As_{40}Se_{60}$ MOF. Presented in [125].

The same group presented single mode guidance in these fibres at 1.55 µm as seen in Figure 39 from [124], this however is only the case if the light coupling is optimised. No data about the guided modes at 2.9µm were given.

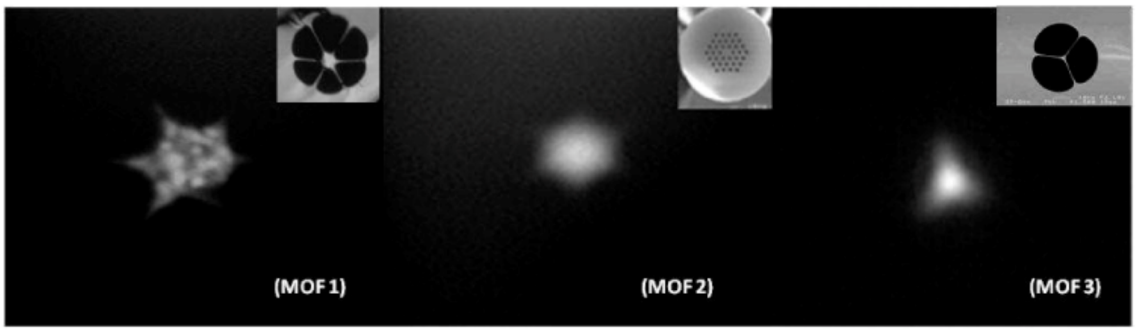

Figure 39: Near-field imaging at 1.55 µm for the three $As_{38}Se_{62}$ chalcogenide MOFs. Presented in [124].

Coseil et al. [68] could show single mode guidance in MOF chalcogenide fibres at the wavelength of 3.39 µm and 9.3 µm, as is seen in Figure 40, there was no information given on the guided modes at 2.94 µm or the energies delivered using these fibres.

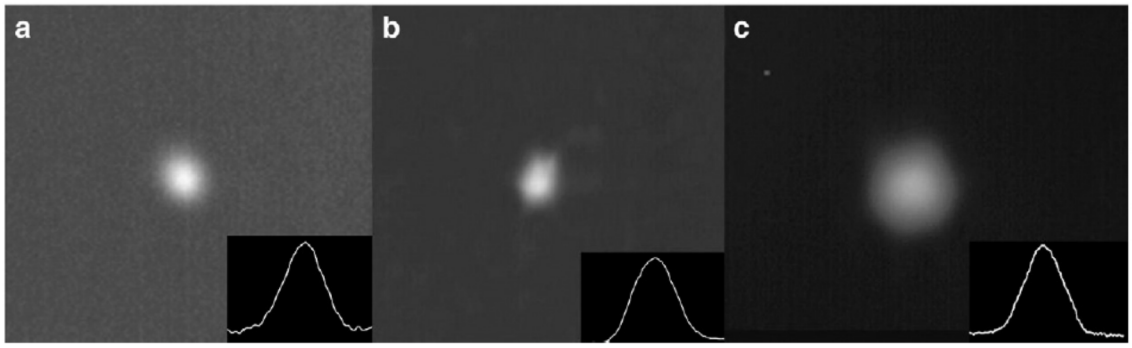

Figure 40: Near-field imaging for $Te_{20}As_{30}Se_{50}$ chalcogenide glass fibres: (a) Step index fibre at 9.3 µm, (b) and (c) MOF at 3.39 µm and 9.3 µm respectively. Presented in [68].

1.4 Fibre encapsulation

For certain applications (such as the medical or surgical applications proposed in this work) it is very important to protect the end of the fibre with a tip, especially if it is a hollow core fibre, to avoid damage or ingress of particulates. This is the case for silica and chalcogenide glass fibres. This is particularly relevant if the fibre is used in "contact mode" (in contact with the tissue or very close to it), where this contamination may enter the fibre. This debris inside the fibre will be heated up rapidly and cause premature destruction of the fibre. Also if the fibre is used in an aqueous or wet environment such as is the case with biological tissue, liquid may enter the fibre if it is not sealed leading to catastrophic failure. However, the endtip itself can introduce loss into the system and may become contaminated and eventually damaged.

One proposed method to seal the fibre is to use a quartz or Pyrex tip [79, 127]. An example for a Pyrex endtip is shown in Figure 41 [127], where the HWG was melted at the end to form a natural endtip. The advantage is that there is no need for bonding or joining an endtip to the fibre which could introduce a weakness and failure in the system. It also lends itself to a relatively simple fabrication route. It was shown that when the tip is used for ablation of pork fat the tip actually has a self-cleaning effect which is even more pronounced if the experiment is carried out underwater [127]. The fibre was a COP/Ag (cycling olefin polymer/silver) hollow core fibre designed for Er:YAG laser delivery. The fibre was 2m long and had an inner diameter of 700 µm. Figure 42 shows the attenuation before and after irradiation on fat, and it is clear that the additional loss due to the fat is relatively small. The absorption bands in the 3.4 µm band are a result of C-H bonds in the fat. Additionally, it is also easy to clean the tip in an ultrasonic bath and return it to its original state. In the experiments, a free running Er:YAG laser with the pulse duration of 250 µs and a repetition rate of 10 Hz was used as the laser light source [127].

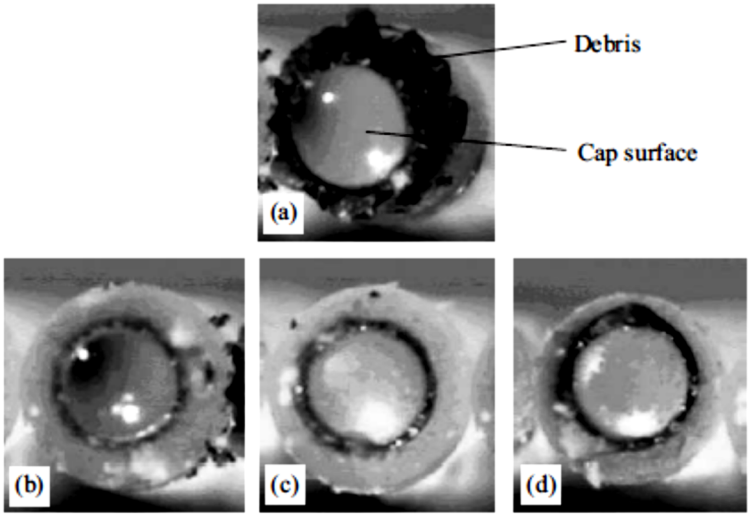

Figure 41: Output surface of sealing tip after contact ablation of 600 pulses on soft tissue. The fibre is a HWG designed for 2.94 µm and the seal is made of silica glass, which is collapsed at the end of the HWG. Irradiation power was 3.1W (a), 2.8W (b), 2W (c), and 1.5W (d). The pulse repetition rate was 10Hz. Presented in [127].

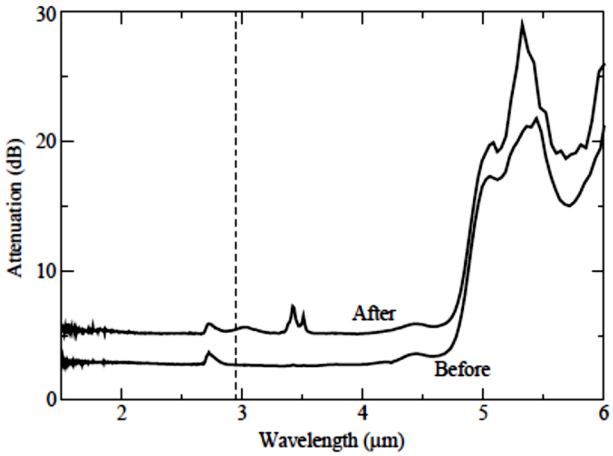

Figure 42: Loss spectra of sealing tip before and after irradiation on fat. The fibre used was a HWG designed for 2.94 µm. Presented in [127]

However, one problem that occurs when using an endtip is that the useable power is limited by the damage threshold of the tip. The tip in the example above exhibits serious damage after 600 pulses (Figure 43b) of 300mJ and failed catastrophically after 1200 pulses (Figure 43c).

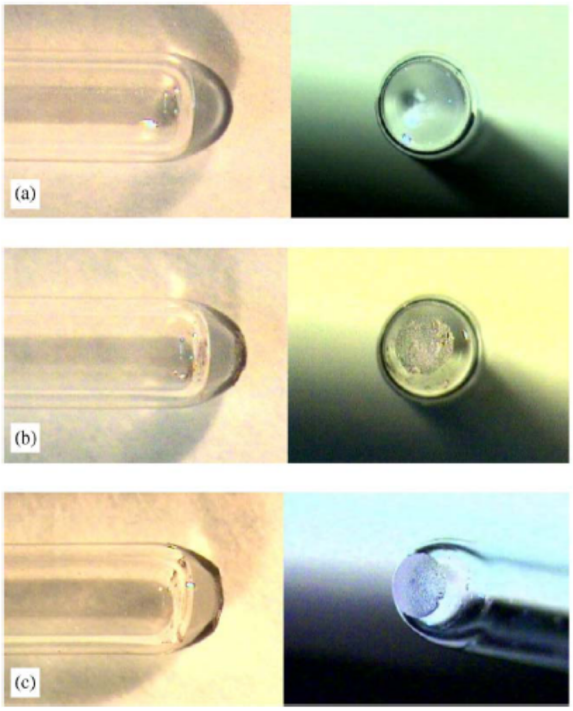

Figure 43: Abrasion of sealing tip after irradiation on hard tissue with a pulse energy of 300mJ and a repetition rate of 10Hz. The fibre was a HGW designed for 2.94 µm with an inner diameter of 700 µm. Abrasion results: (a) original; (b) after 600 pulses and (c) after 1200 pulses. Presented in [127].

Scot et al. [70] demonstrated an endtip used in conjunction with a germanium oxide glass fibre. In this case it was done to protect the fibre from the heat generated during ablation of tissue, as the glass transition temperature of the germanium oxide glass is relatively low: ~680°C. Two different designs of endtip were used and are shown in Figure 44. Both were fabricated from sapphire and were constructed for a side firing setup. The disadvantages of these endtips were that they were relatively large (OD: 0.87-1.2 mm and length: 1 cm); also the endtip had to be glued onto the fibre.

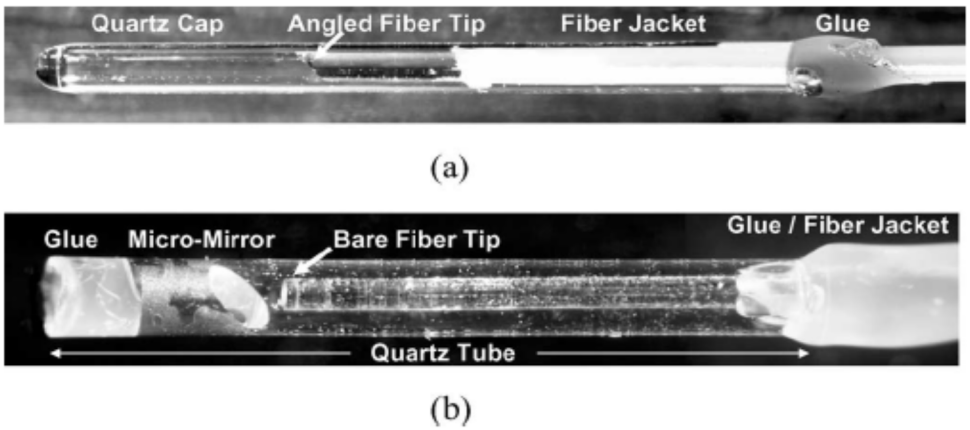

Figure 44: Side-firing germanium oxide fibres. (a) With angle-polishes tips. (b) With micro-mirror assembly. Presented in [70].

Another major drawback of these endtips is that the beam quality exiting the system, as presented in Figure 45, is significantly degraded.

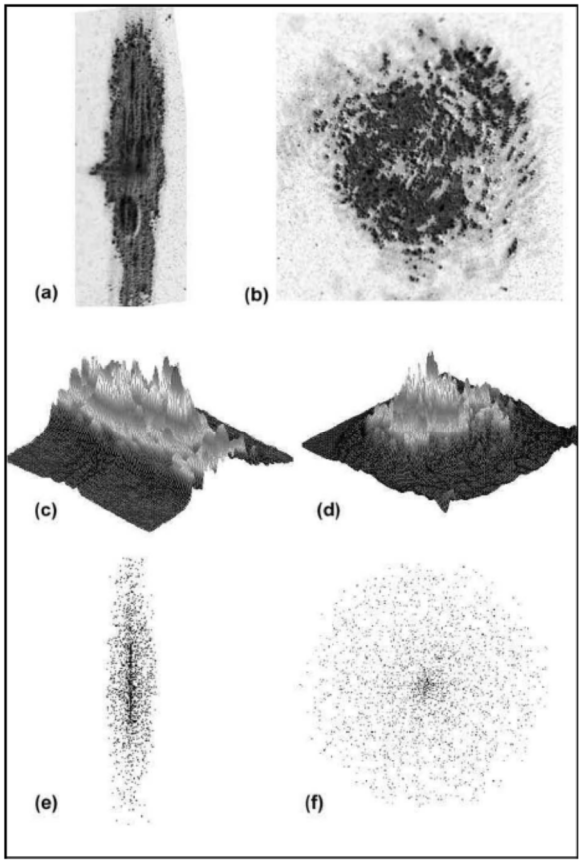

Figure 45: Spatial beam profile of erbium laser beam exiting side-firing fibre: (a), (c), (e) for angle-polished fibre; (b), (d) and (f) for micro mirror configuration. (a), (b) for carbon paper; (c), (d) for infrared camera and (e), (f) for ray-tracing simulation.

HWGs are often sealed by placing a sapphire rod into the waveguide and fixing it using clinically approved cement [128], the tip can withstand the autoclaving process and does not change the beam output profile. This tip version has the best properties reported to date to be used in clinical applications as it does not increase the size of the device/fibre nor does it change the beam profile and could be shown to be used for lithotripsy; however this tip can only be used for HWGs. Solid core fibres and microstructured fibres have to be completely encapsulated to be used in medical applications.

Consequently there is a drive to increase the durability of the endtip as well as to minimize the beam degradation that occurs when using such a component. Another possible area for investigation would be to use the endtip for shaping of the output beam profile by polishing the endtip to a specific curvature or shape. This could enable

focusing, collimation or divergence of the exiting beam, which may be useful for a variety of applications.

1.5 Fibre comparison for the potential use in mid-infrared medical applications

Table 4 compares the fibres discussed in the previous paragraphs in terms of their usability for surgical applications. In detail it compares the energy delivery capability of the fibres, the stability of the beam profile if bent and the minimum bend radius achieved (without causing catastrophic damage to the fibre). All fibres (besides MOF chalcogenide fibres, where no data could be found) could be reported to deliver sufficient energy densities for surgical applications, although in the case of the germanium oxide fibres the energy density was only adequate for the ablation of soft tissue. The main issues with the current fibre delivery systems is the multimode behaviour and the resulting beam profile change if the fibre is bent. Recent developments in (MOF) chalcogenide fibres could show their capability of single mode guidance at the mid-IR wavelength; however the drawback in this case is that the core has to be relative small (~20 µm for solid core fibres and ~40 µm for MOF) which in terms reduces the energy density capability of the fibres. In terms of minimal bend radius most fibres could be shown to able to be bent down to under 15 cm, which gives them suitable flexibility for certain endoscopic processes. However it has to be noted that for some of the fibres (e.g. HWG and sapphire) the flexibility is achieved by reducing the fibre diameter which also leads to decrease in high energy handling capability.

Table 4: Properties of the fibres described in §1.2-1.3 in regards of their potential use in mid-infrared medical applications. MOF stands for microstructured optical fibre. (na – not applicable).

Fibre	Energy delivered for surgery?	Stable beam profile?	Minimum bend radius/mm	Notes
Articulated arm	Yes	Yes	na	Cannot be used in endoscopy
Chalcogenide	Yes	Yes (if single mode fibre)	100	Trade-off between power delivery and flexibility. Can include toxic material
Germanium oxide	(Yes)	No	100	The power delivery presented is just at the threshold of ablation of hard tissue
Fluoride	Yes	No	200	Can be damaged by water
Sapphire	Yes	No	150	Trade-off has to be made between flexibility and power delivery
HWG	Yes	No	100	Already in use for e.g. dental surgery. Limited fibre length
Chalcogenide MOF	No available data	Yes (can be single mode)	No available data	

From Table 4 it can be seen that none of the current fibres investigated for the delivery of Er:YAG laser radiation can fully satisfy the requirements needed for minimally invasive surgical applications. Consequently, there is still a pressing need to develop such fibres which in turn will enable a new range of laser surgery procedures and further enhance the implementation of lasers in medicine. To address this shortfall this work presents the development, characterisation and demonstration of silica based HC-PCFs and HC-NCFs.

2 Materials and methods

2.1 Methods

The following paragraphs will describe the methods which have been applied throughout the presented work. They are related to different measurement techniques of a laser beam diameter, the quality of the measurements and the visualisation using an IR camera system.

2.1.1 Beam diameter measurement using a scanning knife-edge technique

A laser beam diameter can be defined by its standard deviation σ in x and y translation, therefore the two dimensional intensity profile of the beam must be known. For beam profiles that are highly multimodal, irregular, have multiple peaks and/or unclear edged profiles this can be challenging. It can be done by using a sensor array (e.g. camera sensor), but for certain beam wavelength or for tightly focused spots this is not applicable.

A widely used technique to overcome this problem is the *"scanning knife-edge"*, where a knife-edge is scanned (in x or y direction) transversally along the laser beam. The transmitted intensity is measured with a (large) area photo/pyroelectric detector. If the blade is translated along the x-axis, plotting the position of the blade over the first derivate of the transmitted intensity gives an estimation of the beam profile. The profile is integrated over the y-axis in this case. However if only the beam diameter is of interest, the "clip width" D_c can be used, which is defined as the distance between two points in the scan where the transmitted intensity passing the knife-edge rises from a lower clip level εP_0 to an upper clip level $(1- \varepsilon P_0)$. P_0 is defined as the total transmitted power. By multiplying the clip width by a scaling factor, the standard deviation of an arbitrary laser beam profile can be calculated and therefore the beam width determined.

Siegman et al. [129] showed that the lower clip level should be between 8.5 % and 11.6 % and the upper clip between level 88.4 % and 91.5 %. However for an unknown laser beam profile the lowest uncertainty is given if the clipping level is chosen to be 10 %. The beam diameter D can then be calculated by

$$D = 4\sigma = \frac{4D_c}{2.563} = 1.561D_c \qquad (5)$$

where σ is the standard deviation. The authors of the paper [129] also concluded that there will always be an error between the theoretical calculation of the beam diameter and the knife-edge technique. Therefore all the beam diameters given in this work are assumed to have an uncertainty of ±5%.

2.1.2 M^2 measurement

The M^2 factor is defined as: "a parameter for quantifying the beam quality of laser beams" [85] and the standardisation is regulated by ISO Standard 11146 .

It can be fitted using the following equation

$$W(z) = W_0 \left[1 + \left(\frac{z\lambda M^2}{\pi W_0^2} \right)^2 \right]^{\frac{1}{2}} \qquad (6)$$

where W(z) is the beam width at a distance *z* from the beam waist, W_0 is the beam width at the beam waist, *z* is the position of the blade relative to the beam waist and λ is the wavelength.

One has to measure the beam width at several positions (at least 5) around the beam waist e.g. inside the Rayleigh length (Z_R) and several points (at least 4) outside of $2Z_R$. By fitting equation 1.2 onto the measured beam radii, the M^2 value can be determined. "The Rayleigh length (or Rayleigh range) of a laser beam is the distance from the beam waist (in the propagation direction) where the beam radius is increased by a factor of the square root of 2. For a circular beam, this means that the mode area is doubled at this point." from [130]. The Rayleigh length determins the depth of focus.

The z and x position of the blade was measured using translation stages with micro-meter screws with an accuracy of ±5 µm. In addition, where necessary, an LVDT (linear variable differential transformer, from Tesa Tronic TTD20) with an accuracy of ±0.1 µm was used. A blade was made of a ceramic material (Radiall F780 from Thorlabs) had to be used to withstand the high energy density at the focal position, which was not possible with a standard razor blade. The analytical fitting was done using the Origin (OriginLab, Northampton, MA) software.

2.1.3 False colour image

During certain steps a visualisation of the beam profile was necessary as the beam diameter alone did not give enough information. For this purpose a mid-IR camera (Electrophysics Cop., PV320 – L2E) was used, which captured the reflection of the laser radiation from the ceramic surface. Direct imaging was not possible as the energy levels exceeded the damage threshold of the camera chip. The low resolution of the images is due to the relatively large pixel size of the camera chip (50x50 µm) compared to camera chips in the visible regime (~2x2 µm). The raw data was read into MatLab (The MathWorks Inc., Natick, MA) and a false colour image was produced.

2.2 Lasers

In this work three different lasers have been used. The first one was a diode laser (JDS Uniphase) emitting at a wavelength of 1064 nm. This one was used to characterise the optical properties of the fabricated endtips (§6) with the use of a HC-PCF. The reason for using this laser first was because at the time the measurements were carried out, no HC-PCF or HC-NCF in the 3 µm region was available. It also had the advantage that the alignment and handling at this wavelength was easier and gave some practice and experience for later experiments.

The other two lasers used operate at 2.94 µm as this is a relevant wavelength for medical applications, as already described in the introduction and literature review (§1.1). The first system was an Impex High Tech ER-15 high power laser and the second a Sheaumann MIR-Pac. The following Chapter describes the three different lasers with their attributes and different configurations.

2.2.1 JDS Uniphase

For the initial test a Nd:YAG (neodymium-doped yttrium aluminium garnet) from JDS Uniphase (NP-108220-100) was used. It emits at a wavelength of 1064 nm. The repetition rate is 8 kHz with a pulse width <1 ns and a pulse energy >8 µJ. The output beam profile is shown in Figure 46. The image was captured by Piotr Jaworski using a Pulnix (TM-6CN) camera and Spiricon (LBA-PC, version v3.03) software.

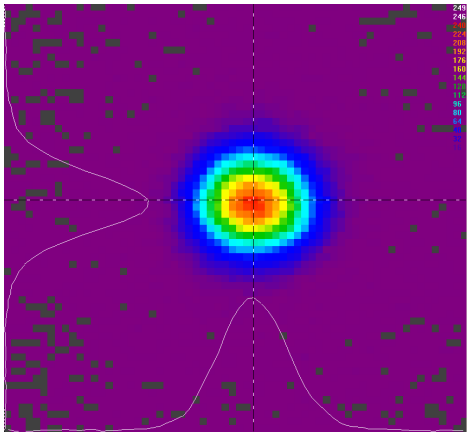

Figure 46: JDS-Uniphase laser beam profile. The Laser wavelength is 1064 nm with a pulse width of <1 ns and a pulse energy of >8 µJ. This laser was used to determine the beam profile distortion due to the endtip.

To get a value for the beam quality, the M^2 of the laser was measured according to the ISO Standard 11146 [131]. The beam diameter was measured using the knife-edge measurement method described in section §2.1.1.

The laser output beam, of measured diameter 0.2 mm, was collimated and focused using a 60 mm focal length lens. For the fit as shown in Figure 47 an M^2 value of 1.1 was used, leading to a good agreement between measurement and calculation.

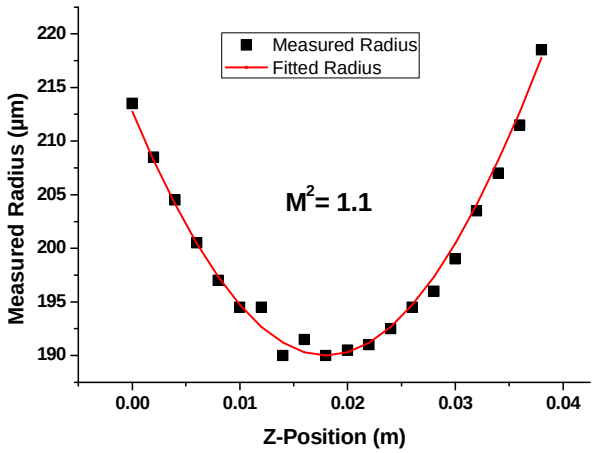

Figure 47: M^2 measurement and fit for the JDS-Uniphase laser. The M^2 of the laser was calculated to be 1.1.

2.2.2 Impex High Tech ER-15

The Impex High Tech ER-15 is an Er:YAG (Erbium : Yttrium Aluminium Garnet) laser emitting a laser radiation of 2.94 µm. This is a flash lamp pumped laser with an Er:YAG crystal as the gain medium. The repetition rate is dictated by the flashing frequency of the lamps, which is 15 Hz. A single pulse operation is also possible. A schematic of the laser cavity is given in Figure 48. The laser consists of 3 mirrors in total where the two outer ones are curved. The output coupler has a reflectivity of 90%.

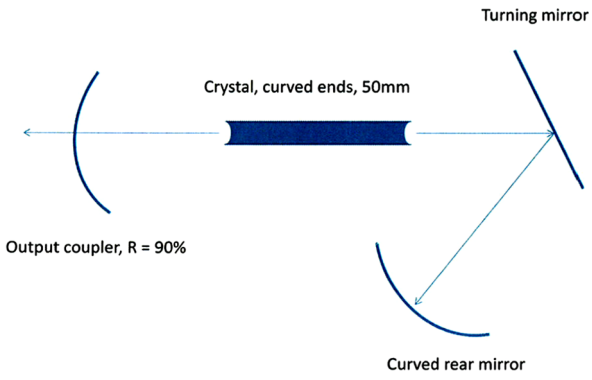

Figure 48: Schematic of the IMPEX laser.

The pulse width was measured to be 225 µs for the full width half maximum (FWHM) value. A temporal pulse profile is shown below in Figure 49.

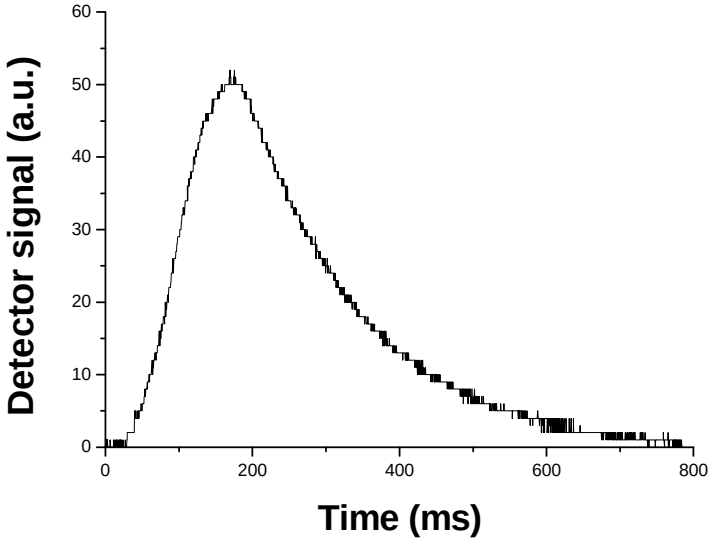

Figure 49: Temporal beam profile of the IMPEX laser. The FWHM is 225 µs.

The laser output power is regulated by changing the voltage to the flash lamp. The graph of the flash lamp voltage versus the laser output energy is given in Figure 50.

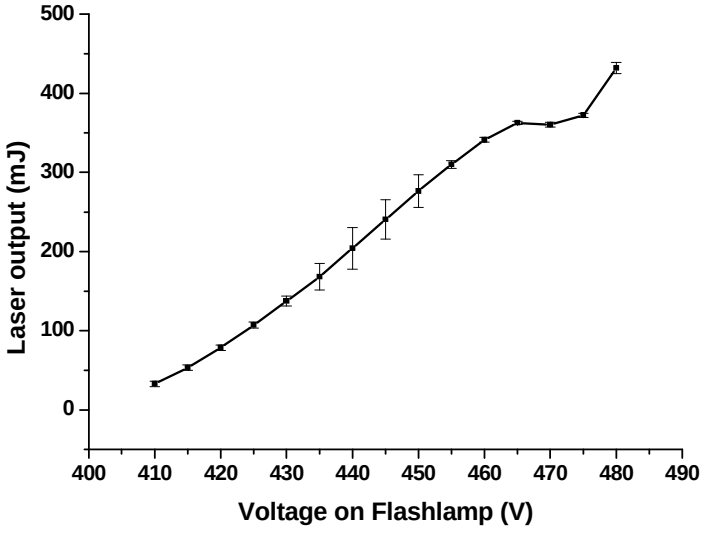

Figure 50: Laser flash lamp voltage against the laser output power including error bars for the IMPEX laser.

The error bars represent the shot-to-shot stability for the different output energies. These were measured with the integrated function of the laser power head. As can be seen the maximal output energy is 431 mJ, which is high enough to ablate (biological) tissue, assuming the beam is focused to a focal spot diameter of <630 µm. However the laser

was mainly operated in the range of 460 V to 465 V, as it was the most stable in this regime. The laser beam profile provide issues for a number of tests carried out in this work, as described later, as it is doughnut shaped (see Figure 51 for a false colour image).

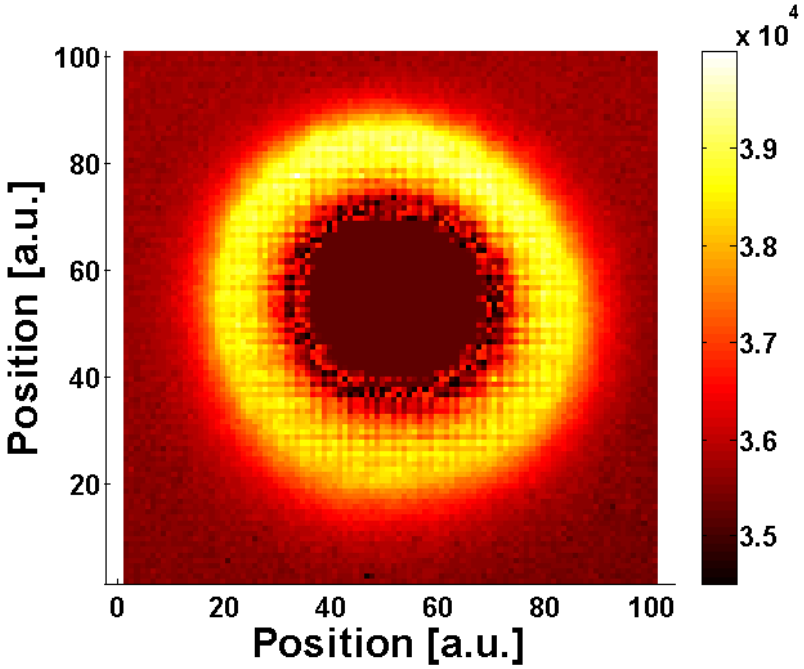

Figure 51: False colour image of the Impex laser output beam profile. The beam was reflected from a ceramic surface and captured using a mid-IR camera (Electrophysics Cop., PV320 – L2E). The wavelength of the laser is 2.94 µm with a pulse width of 225 µs at 15 Hz.

The M^2 of the Impex laser was measured and is shown in Figure 52. The M^2 for this laser was found to be 2.5.

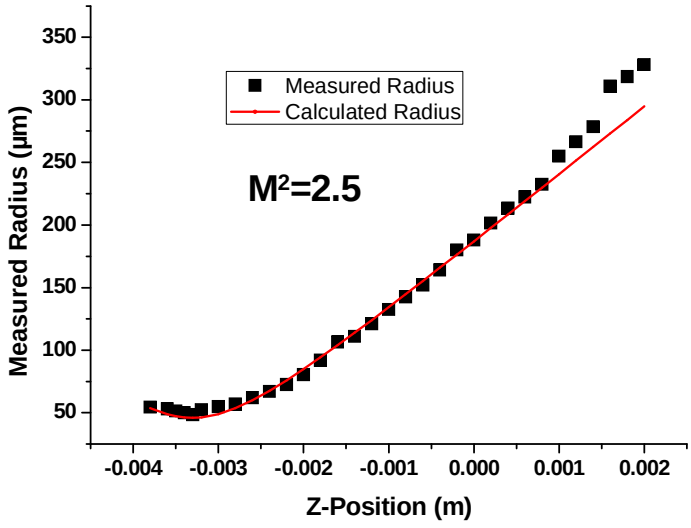

Figure 52: M^2 measurement and fit for the Impex laser.

This laser system and setup was used for the high power delivery experiments as will be described in §3.7 and §4.7.

2.2.2.1 Polarisation and attenuation

The minimum output from the laser is around 30 mJ. This causes an issue for beam measurements e.g. measuring the spot size of a tight focus as the blade (including ceramic blades) is ablated. Furthermore, during the alignment of fibres for laser coupling, the high energy density ablated the core surrounding structure (see §3.7). It would also be advantageous if the laser could be attenuated outside of the cavity, as the beam profile can change with variation of the flash lamp voltage, due to thermal effects. Therefore solutions for external attenuation whilst keeping the lasers operating parameters unchanged were investigated.

A common method for attenuation is through the use of λ/2 wave plates. If the laser emission is linearly polarised only one λ/2 wave plate is necessary. The Impex laser however, has a random polarisation state, therefore two plates are needed: the first to linearly polarise the output beam, and the second to regulate the attenuation. The advantage of this method is that continuous attenuation from 0% to 100% can be achieved. However, part of the initial power is already attenuated by the first λ/2 wave plate. Furthermore, if the beam is not evenly randomly polarised, the spatial profile of the transmitted beam changes. The power loss was not a significant problem for most of the tests presented here as there is sufficient energy transmitted through both waveplates, however the change of beam profile. The beam profile changed from a doughnut to two separate elliptical spots. The profile after the first λ/2 wave plate is shown in Figure 53, where the profile was captured on heat sensitive paper.

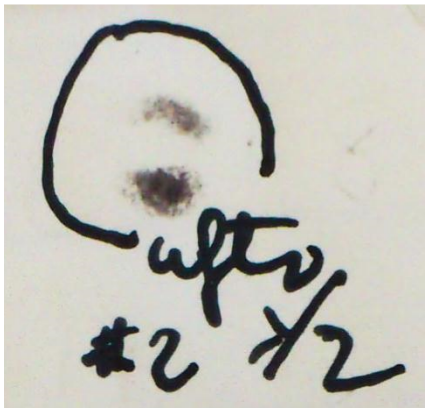

Figure 53: Beam profile after a λ /2 wave plate using the IMPEX laser. This image was taken on heat sensitive paper. The original beam profile was a doughnut and is transformed into two separate elliptical spots due to the random polarisation.

To reduce the degradation of the beam profile it is possible to polarize the laser inside the cavity and so get an even attenuation through the first λ/2 wave plate alone. To do this a sapphire window was placed inside the cavity. The angle between the laser propagation path and the window has to be the Brewster angle. The Brewster angle θ_B can be calculated by $\theta_B = \arctan(n_2/n_1)$ where n_1 and n_2 are the refractive indices of the two media along the boundary. The refractive index of sapphire and air at 2.94 μm was taken as 1.712 [132] and 1, respectively.

However this was not successful, and instead of a clean round beam profile the output of the laser was a beam with three high intensity regions (Figure 54).

Figure 54: Output beam profile after insertion of the Brewster window into the cavity of the IMPEX laser. Three separate spots are the resulting output beam profile.

2.2.2.2 Optimisation of beam profile

As mentioned previously, the beam profile of the IMPEX laser was a doughnut. This is not ideal for some applications, e.g. coupling into a single mode fibre. To improve the laser beam profile, a ceramic aperture was placed inside the laser cavity.

The cleaned laser output beam profile was extended to a diameter of 20 mm, a pinhole with a diameter of 2 mm was moved along the x and y axes in 1 mm steps. The power through the pinhole was measured using a power meter. This gave the beam profile in Figure 55. This was an improvement in shape compared to the original doughnut beam shape. However the M^2 of this beam profile was just marginally better with 2.3 compared to the original doughnut shaped beam profile which had a M^2 of 2.5. Therefore a laser system with a much higher beam quality was purchased (as is described in §2.2.3) to investigate the optimisation of the coupling.

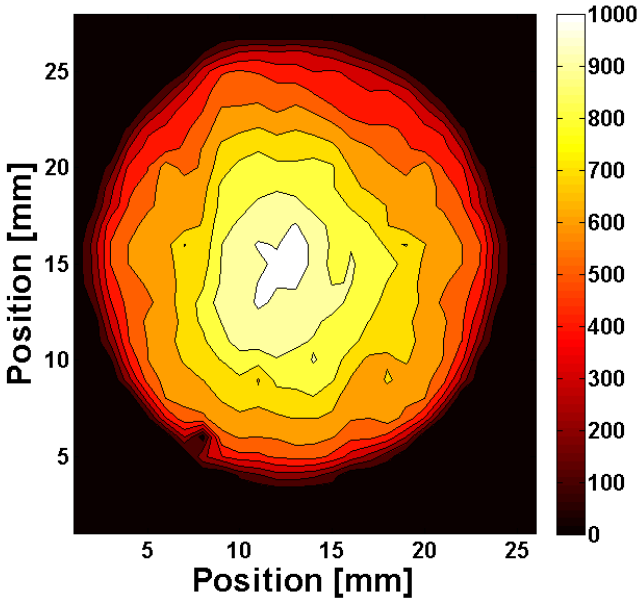

Figure 55: laser beam profile after insertion of a 2.5 mm diameter aperture into the laser cavity.

2.2.3 Sheaumann laser

The second Er:YAG laser system was a Sheaumann MIR-Pac. This is a cw-laser with a maximal output power of 1.5 W. The beam profile is single mode and Gaussian, as was shown by Sheaumann [133]. The M^2 for this laser is 1.4 as can be seen from the fit in Figure 56. The laser system was also much more stable than the IMPEX system, over a time of 10 min the laser fluctuated only in a region of ±2.1% (842.4 ± 17.7 mW)

This laser system was used for the coupling efficiency measurements as described in §3.3 and §4.5

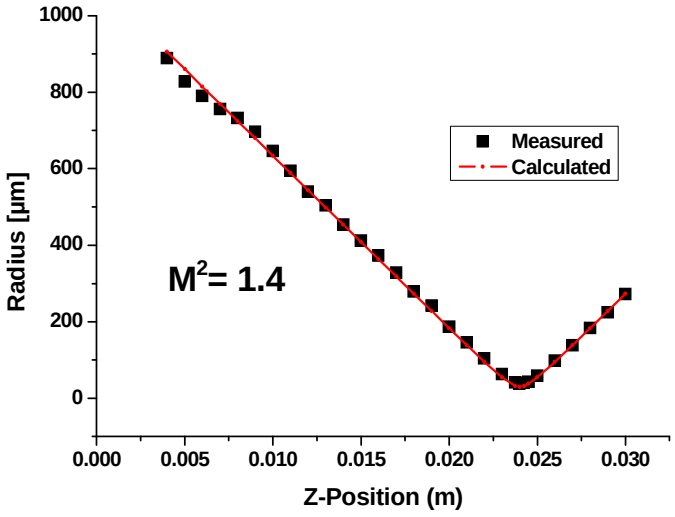

Figure 56: M^2 measurement and fit for the Sheaumann laser.

3 Hollow Core-Photonic Crystal Fibre

3.1 Introduction

The first fibre design investigated was the hollow core-photonic crystal fibre (HC-PCF). The guidance of this fibre type is based on the principle of achieving a bandgap around the core, in which particular frequencies of electro-magnetic waves cannot propagate within a range of angles effectively confining guided modes inside the core. This is possible due to the periodic structure surrounding the core, which is built up from air holes (formed by stacked capillaries) in fused silica propagating along the fibre (Figure 57). Depending on the pitch (the distance between two air holes in the periodic structure) the bandgap can be controlled and the fibre designed to guide in a desired wavelength regime [96].

One of the main benefits from such a hollow core design is that the light-material overlap is minimal. This leads to the possibility of extending the transmission window of silica based fibres beyond that exhibited by the bulk material.

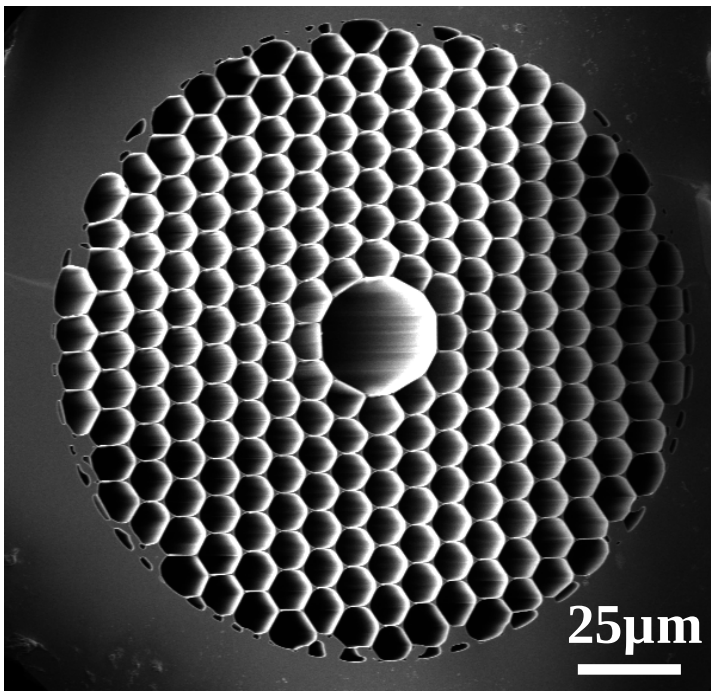

Figure 57: SEM picture of the HC-PCF used in this work,
the core diameter is 24 µm, the pitch is ~8 µm and the PCF region is ~135 µm across.

In this Chapter a silica HC-PCF will be characterised, specifically in relation of its attenuation (§3.4), bend sensitivity (§3.5), high energy pulse delivery capabilities (§3.7) and output beam profile (§3.8).

3.2 Fabrication

The fabrication of microstructured fibres, which the HC-PCF is one type, is usually done by a stack and draw method. The basic principle is shown in Figure 58. The first step was to acquire or draw the capillaries needed; the dimensions were around 1 m in length and 3-4 mm in diameter. These were then stacked into a preform which was a scaled up version of the desired design; it was placed into the furnace and drawn down to a cane. This cane was placed back into the furnace and drawn down to the final fibre. In this last step it was important to apply a pressure differences between the core and the surrounding structure to get the desired pitch and to avoid a collapse of the core/surrounding area. A protective polymer layer was applied onto the fibre after the final draw.

This specific design (Figure 57) is a so called 7-cell defect fibre, which means that 7 capillaries are missing in the middle and so build up the core of the fibre.

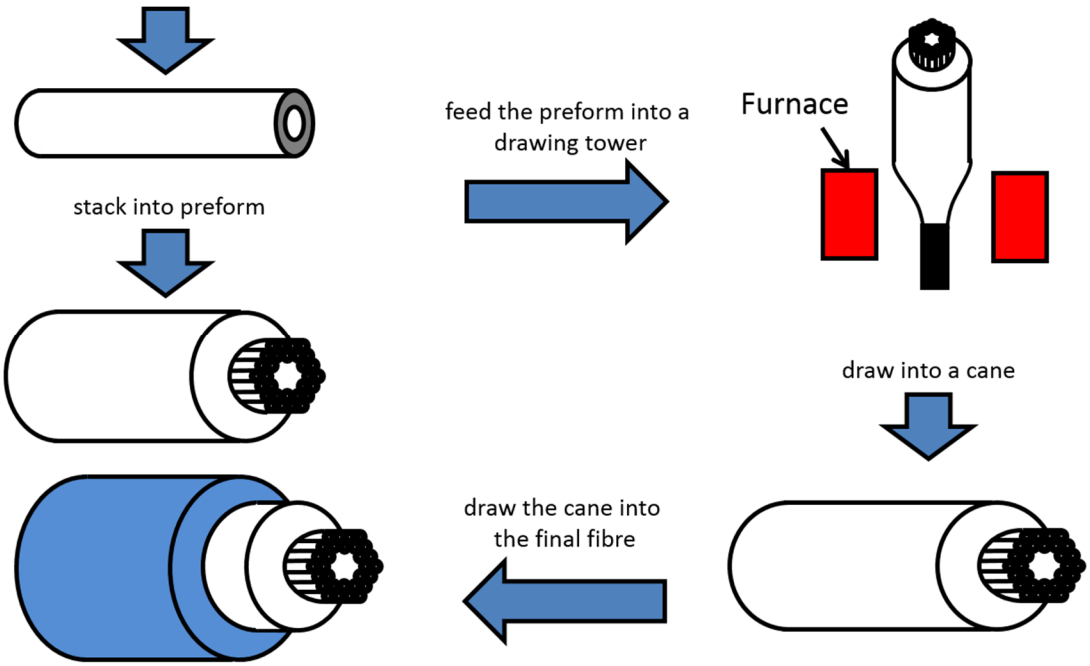

Figure 58: Basic schematic of a stack and draw process. Starting with the fabrication of the capillaries, which are stacked into a scaled up preform of the fibre design including the cladding. The preform is drawn into a cane typically 3-5 mm in diameter, which is drawn into the fibre. In the final step a protective polymer coating is applied.

Different pressures have been applied to the core and the surrounding structure, to see the effects on the guidance band. In total 3 different spools were drawn with the following specifications:

Table 5: Specifications of the drawn HC-PCF for the 3 µm region.

Type	Core diameter/µm	Pitch/µm	Attenuation at 2.94 µm/dBm^{-1}
BF2900#2	27.5	9	2.3±0.3
BF2900#3	27.3	7.9	1.7±0.2
BF2900#4	24.5	7.5	1.1±0.2

All the attenuation measurements were done using the setup described in the following paragraph (3.4) shortly (several hours) after the drawing process at the University of Bath and again weeks after the drawing at the Heriot-Watt University. The fibre BF2900#4 had the lowest attenuation after drawing, therefore only this type was used for all the further characterisations and is now referred to as the HC-PCF.

It should be noted that the fibres were drawn by the group of Prof. Jonathan Knight in the department of physics at the University of Bath, UK and the drawing process and its optimisation was not the scope of this PhD work.

3.3 Coupling efficiency

To investigate the coupling efficiency the IMPEX laser system was used in two different configurations. The initial trials were done with the IMPEX laser where the output beam profile was doughnut like (§2.2.2). To achieve the optimal fibre alignment it was mounted onto a 3-axis micro-block (Melles Griot) with an additional option of adjusting pitch and yaw. Due to the relatively poor laser beam quality (M^2 of 2.7) it was not possible to match perfectly the fibre mode field diameter (24 µm) and the NA (0.12) simultaneously. Therefore different combinations have been used as detailed in Table 6. In Figure 59 the optical setup is presented schematically, which consisted of a telescope to magnify the laser output beam and a final coupling lens to achieve the necessary spot size and NA. No plasma was observed at the focus of the (keplerian) telescope, even with the highest power output. This generic optical setup was used throughout the work with different lenses.

Table 6: Combinations of NA and spot size for coupling into the HC-PCF using the IMPEX laser at 2.94 µm.

NA	Spot size diameter/µm	Maximum Coupling efficiency/%
0.06	92	3.5
0.12	46	5
0.2	21	3.9

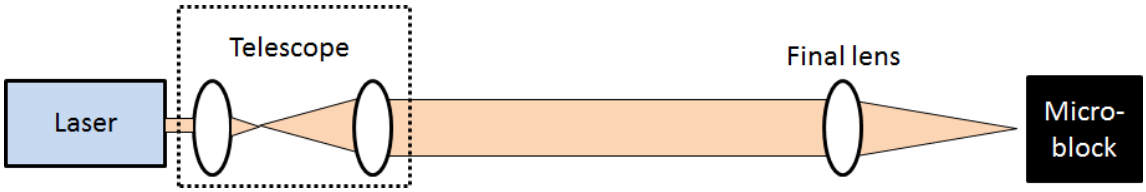

Figure 59: Optical setup, as used for all the experiments, consisting of a simple two lens telescope and a final lens to couple the light into the fibre, which is aligned using a micro-block.

These are relatively low coupling efficiencies and assumed it was because of the poor match of the fibre mode (see §3.8) and the laser beam profile. Therefore the laser was modified to produce a more Gaussian like output beam profile (§2.2.2.2). Using this beam profile and the optical setup shown in Figure 3 (NA = 1.2 and spot size diameter of 46 µm) resulted in a slightly higher coupling efficiency of 8.5%. This coupling efficiency was still quite low, but as seen from the numbers for the spot size and NA they still did not match the fibre perfectly; also the M^2 of the laser in this configuration was just 2.5 and therefore not perfect to couple into a fibre with a M^2 of 1.4 (§3.9)

In comparison to the established fibres like HWGs which can achieve coupling efficiencies of > 94% [134] and HC-PCF for 840 nm with coupling efficiencies of > 98% [135] this was very low. However in the case of the HWG the core size "usually much greater and around 1 mm" had in both cases the mode of the fibre could be nearly perfectly matched which was not the case using the laser source for this experiment. At the time the Sheaumann laser system (§2.2.3) with the higher beam quality was available the fibres were too degraded to get any meaningful data.

3.4 Attenuation

The attenuation for the HC-PCF is shown in Figure 60. The average loss in the wavelength range 2.9 µm to 3.18 µm was ~1.2 dB/m. For this specific fibre the attenuation at 2.94 µm was 1.1 ± 0.2 dB/m. The attenuation was measured using a Bentham TM300 monochromator with a spectral resolution of ~20 nm using a cut-back technique, from an initial length of 5 m to 1 m. Four 1 m samples were cut back and the

average loss of the fibre calculated. These measurements were carried out by Dr. Robert R. J. Maier, who was the research associate to the project at the Heriot-Watt University. A tungsten halogen bulb was used as a broadband light source. As OH has an absorption peak around 3 µm it is often important to control the OH concentration during the fibre fabrication, however during the fabrication of these fibres there was no particular care taken.

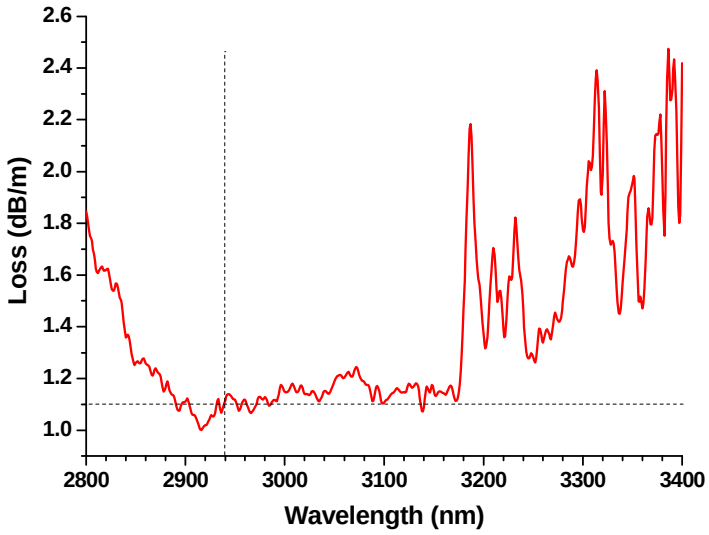

Figure 60: Optical loss spectrum for the 2.94 µm HC-PCF fibre measured by a cutback technique from an initially 5 m long fibre sample in four steps of 1 m each. Carried out by Dr. R.R.J. Maier the research associate for the project.

3.5 Bend sensitivity

The bend sensitivity of the fibre was investigated using the IMPEX laser system. The results are presented in Figure 61. The error bars indicate the fluctuation in the delivered pulse energy due to the stability of the laser. As can be seen there was no significant drop in the output energy of the fibre even if bent to a tight radius of 2.5 mm. The physical breaking point of the fibre was at a bend radius of < 1.5 mm.

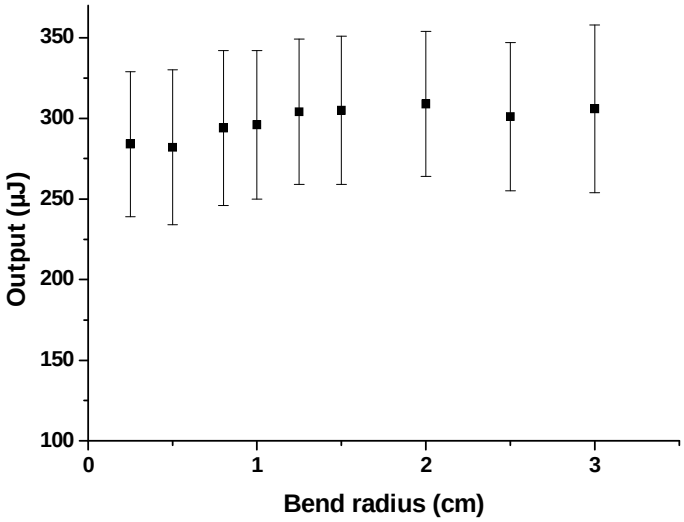

Figure 61: Bend sensitivity of the HC-PCF, down to a bend radius of 2.5 mm without any significant drop in delivered pulse energy.

To demonstrate the flexibility and bend insensitivity the fibre was placed into an M6 nut with an approximate inner diameter of 5.8 mm, as shown in Figure 62. During this test pulses with an energy of 12 mJ (at a repetition rate of 15 Hz) were delivered through the fibre.

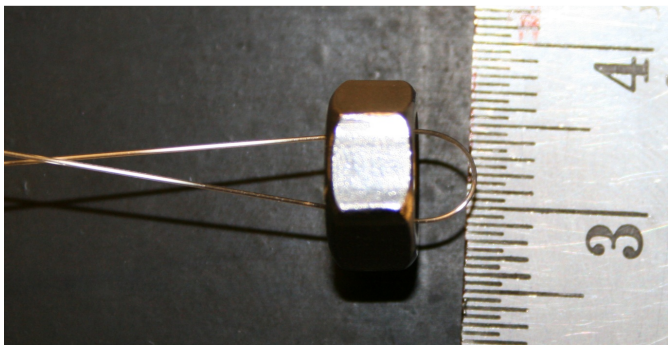

Figure 62: HC-PCF held inside an M6 nut capable of delivering 12 mJ pulses.

3.6 LIDT and maximal theoretical limit

To evaluate the ultimate *Laser Induced Damage Threshold* (LIDT) of the HC-PCF i.e. the potential energy handling capability of the fibre if light could be coupled in efficiently, light was deliberately focused onto the cladding structure and the pulse energy required to cause catastrophic damage was determined. The cladding structure was damaged at a pulse energy of ~125 mJ with a spot diameter of 23 µm. This leads to a fluence of ~30 kJ/cm^2. The damaged end of the fibre is shown in Figure 63.

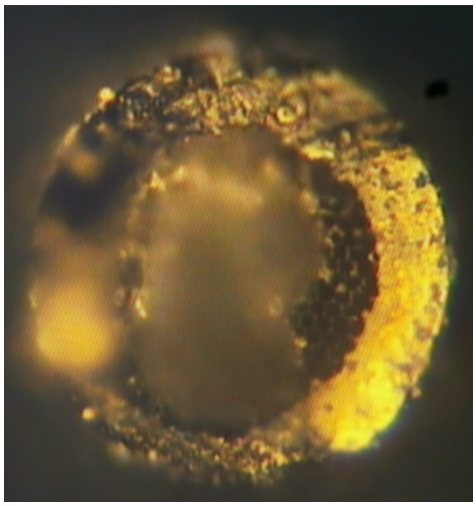

Figure 63: HC-PCF fibre end facet deliberately destroyed in order to determine the LIDT of the fibre. The IMPEX laser with a pulse energy of ~125 µJ at 2.94 µm and 225 µs pulse width was used to achieve the damage.

Previous work [101] found the LIDT for the cladding structure of a similar silica HC-PCF to be 130 – 140 J/cm^2 for an 8 ns pulse (at 1064 nm). The approximation factor of $t_p^{1/2}$, where t_p is the pulse width, can be used to scale energies [136] from a 8 ns to a 250 µs pulse. Scaling the 8 ns pulse results gives an expected LIDT of 23.5 kJ/cm^2 for a 225 µs pulse which is in close agreement to the value found in these experiments (30 kJ/cm^2). In fact one would expect a slightly different value for the LIDT in these experiments, which were conducted at 2.94 µm compared to 1.064 µm, as materials have been shown to have a different LIDT at different wavelengths [47]. The potential capability of these fibres for pulse delivery can be estimated by considering a Gaussian beam at the input face. Fibre damage will occur if the intensity at the input face incident on the silica glass surrounding the air core exceeds the damage threshold. As determined above, if the fluence in the silica glass cladding exceeds 30 kJ/cm^2, then the fibre will be damaged. The mode field diameter of the fibre was estimated to be the same size as the core at 24 µm. A Gaussian beam of $1/e^2$ of 24 µm and a fluence of 111 kJ/cm^2 cantered in the air core will result in the fluence at the silica glass cladding reaching the damage threshold of 30 kJ/cm^2.

At a fluence of 111 kJ/cm^2 and a 24 µm diameter core a 500 mJ pulse would be delivered. This value could be considered to be the absolute maximum pulse energy deliverable with these fibres using an optimised laser source with sufficiently good beam quality to achieve a Gaussian beam waist of appropriate diameter and divergence to enable ideal coupling.

3.7 High energy pulse delivery

For the high energy pulse delivery investigation the IMPEX laser was again used. The laser output was expanded to a diameter of 2.1 cm (4σ beam width) and launched into a 0.4 m long fibre using a CaF_2 lens with f=100 mm. This configuration led to an NA of 0.1 and a corresponding spot diameter of 46 µm. As described in paragraph 3.3 a compromise had to be made between the NA and the spot size due to the poor beam quality of the IMPEX laser (M^2 of 2.7). This configuration led to the highest coupling efficiency of about 5%.

Optimal fibre alignment conditions were achieved by using a 3-axis micro-block with the additional alignment of pitch and yaw (Melles Griot). For the initial alignment the laser was operated just above threshold and one or several glass microscope slides were placed in the beam path to provide variable attenuation (T=47% per slide) [50]. This was necessary in order to avoid damage to the fibre launch face during the initial alignment. Once the alignment was optimised the slides were removed and the laser output power gradually increased to determine the maximum transmission. The front or launch facet of the fibre was monitored with a camera to detect any damage due to incident laser radiation. The fibre was bent with a single 180° bend and a radius of ~10 cm during these experiments.

The maximum output power delivered through the HC-PCF was measured to be 210 mW at ~15 Hz, corresponding to pulse energy of 14 mJ with a pulse length of 225 µs FWHM. This translates to energy densities of >3.4 kJ/cm^2 at the fibre output end. If the laser output power was increased over this value the fibre launch facet sustained catastrophic damage and the cladding area surrounding the core was completely destroyed, similar to the damage seen in Figure 63.

However, even after the fibre launch end sustained catastrophic damage, it was still possible to guide light through the fibre and a power of 80 mW (5.4 mJ) could still be transmitted without any further damage to the fibre. No damage to the output facet was observed during any of the experiments and the output facet had the appearance of a pristine cleaved end (as shown in Figure 57). This again suggests that given optimal launching much higher pulse energies could potentially be delivered.

3.8 Output beam profile

The beam output profile of the fibre is an important factor for many applications. Therefore two different measurements were conducted. The first was a knife edge

measurement at the fibre output to measure the integrated power. A ceramic blade was used to avoid ablation of the material. The measurement result is shown in Figure 64 including the fitting of a curve with R^2>0.995. The derivative of this curve was then used to calculate the intensity cross-section. This prevented artificial spikes appearing in the intensity profile which would arise due to the small fluctuation in laser output energy.

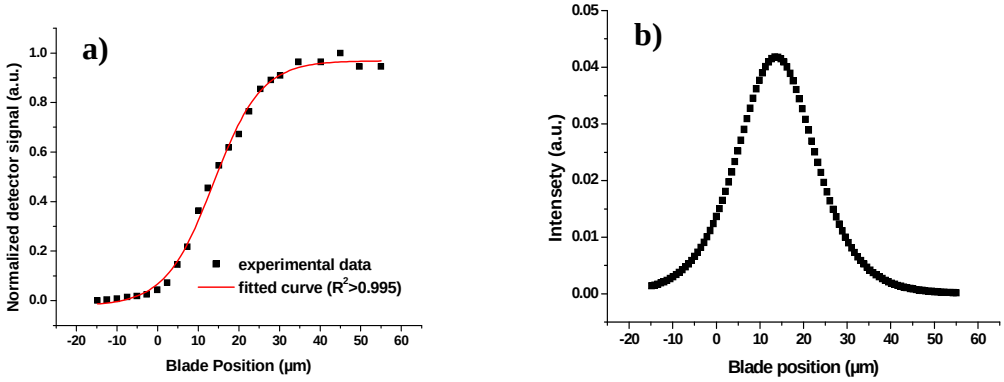

Figure 64: a) Output beam profile of the HC-PCF with fitted curve (R^2>0.995). Measurement was carried out using a knife–edge and b) Derivative of the fitted curve showing the spatial intensity profile of the beam.

To verify the confinement and the single mode profile, the beam profile was measured using a mid-infrared camera (Electrophysics PV320-L2E). The output could not be imaged directly with the available camera due to the relatively large pixel size of the detector ~50x50 µm which did not provide sufficient resolution. Therefore the beam was re-imaged onto a ceramic surface and the reflection was captured by the mid-infrared camera. A ~15× magnification telescope was used to take the near-field images. Additionally the image was not taken in the exact focal plane however the image plane was still within the Rayleigh length to enhance the resolution. Additionally images were taken in the far-field to quantify the beam propagation. The images with corresponding line scan cross-sections are shown in Figure 65. The offset of the pictures is due to background noise.

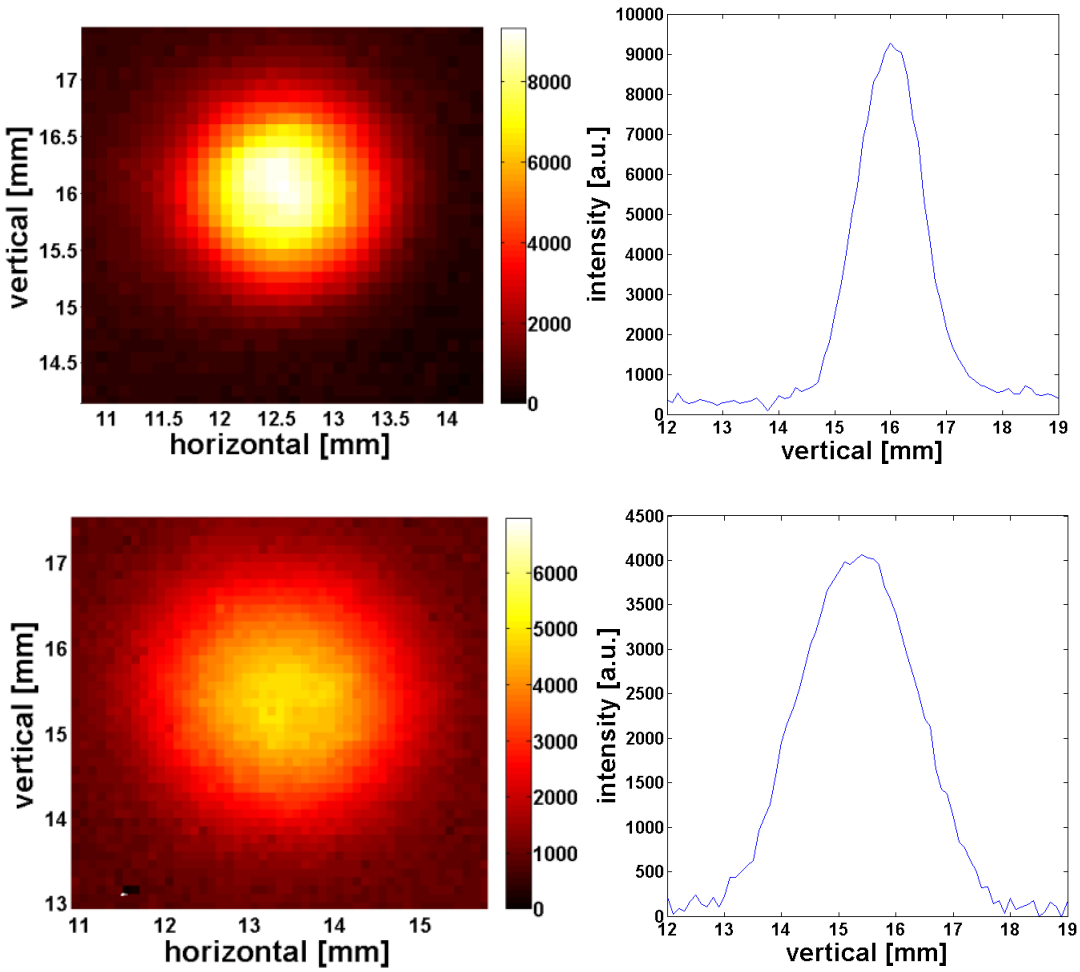

Figure 65: Near- and far-field beam profiles: a) Near-field profile at the fibre end with; b) associated line scan (images are magnified); c) Far-field profile at a distance of 4 cm from the fibre output end with d) associated line scan. The IMPEX laser was used for these measurements.

As can be seen from these false colour images the beam output profile is approximately round and single mode. The NA of the fibre was calculated as 0.12, by measuring the divergence of the output beam.

3.9 M^2

The M^2 of the fibre was measured according to ISO standard 11146. The $1/e^2$ beam diameter was measured using a knife-edge method (for more details see §2.1.1), the error was estimated to be ±5%. The M^2 for the HC-PCF is 1.4 as can be seen from the best fit to the measured data shown in Figure 66.

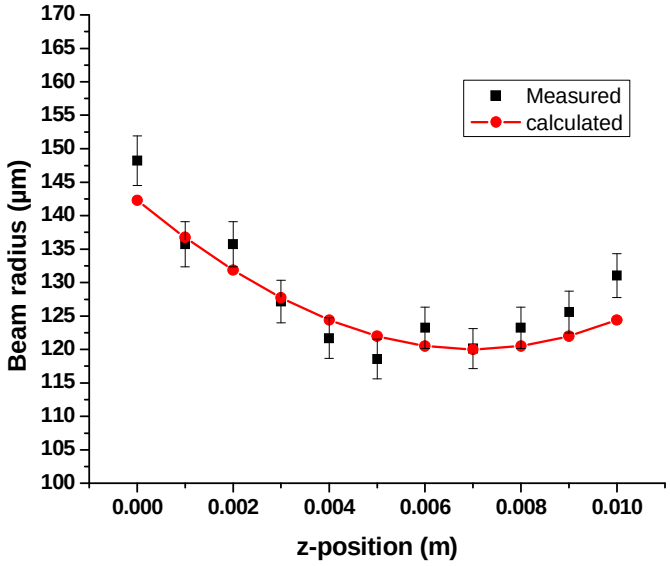

Figure 66: Fitted M^2 parameter of 1.4 onto the measured values for the HC-PCF using the ISO 11146 standard. The IMPEX laser was used.

3.10 Storage and water absorption of the fibre

Although, as discussed previously, no particular care was taken during the fabrication steps to eliminate or minimise OH the fibre has to be stored in a dry atmosphere e.g. in a desiccators once fabricated. This is to reduce the ingress of moisture over time as OH groups can bond to the silica and drastically increase the attenuation at 2.94 µm. The original spools of the fibre were stored in an uncontrolled, humid lab environment, leading to a significant increase of the attenuation at 2.94 µm, due to the absorption peak of OH at this wavelength. A cutback measurement was done with the fibre (BF2900#4 (§3.4)), after about 2 months in the lab environment. The cutback length was from 10 m down to 1 m in one step resulting in an attenuation of >24 dB/m at 2.94 µm. It is assumed that OH propagated or diffused into the internal structure of the fibre and was bound to the fused silica. The cutback measurement was carried out for different sections of one draw, i.e. short sections from a long draw where measured separately, to see if the OH penetrated through the whole length of the spool (~50 m). This increased attenuation was observed through the entire length of the spool. Several methods have been tried to remove the OH from the fibre inside:

- Annealing the fibre at 110°C for > 48 h with and without a nitrogen purge through the fibre holes.
- Laser drying of the fibre: launching of laser radiation into the fibre for > 3 h to evaporate the OH inside

- Microwave drying of the fibre
- Leaving the fibre in a desiccator for > 9 month

All these methods had no measurable effect on the attenuation of the HC-PCF therefore highlighting the need to keep the fibres sealed from the atmosphere and stored under dry conditions once fabricated.

3.11 Conclusions

The HC-PCF has several attributes which distinguishes it from other fibres operating at the same wavelength. The most important to mention is that the fibre attenuation is independent of bend radius down to a radius of < 2.5 mm. The bend sensitivity is often a significant problem for practical medical applications and limits the use of fibres, however, it has been shown the HC-PCF presented here has the potential to circumvent these issues. Also, the single mode guidance of the fibre is of interest and importance for (medical) applications, because this leads to well-defined cut geometry and no fluctuation in the beam profile during movement. As will be discussed in Chapter §5.3 the demonstrated delivered energy fluence is well above the ablation threshold needed for laser surgery.

However, if the fibre is used practically then care must be taken that it is stored in a dry environment once it has been fabricated. For integration into a laser beam delivery system the fibre must be hermetically sealed from both sides using an endtip (Chapter 5) to avoid OH penetrating into the fibre core, however this would introduce Fresnel reflections on both sides slightly reducing the maximum deliverable power. It is also important that the coupling into the fibre is optimised, which is dependent on the ability of matching the mode profile of the fibre.

4 Hollow core-negative curvature fibre (HC-NCF)

4.1 Introduction

The hollow core-negative curvature fibre (HC-NCF), is also known as a simplified hypocycloid-core Kagome fibre [116] an example of which is shown in Figure 67. The guidance of this fibre is due to the so called anti-resonance reflection optical waveguide (ARROW) principle and was first described in detail by Lichinister et al. [112]. The inner core wall (see Figure 67) of the fibre can be described as two interfaces of air and glass which can be seen as a Fabry-Pérot resonator (FPR). All wavelengths in resonance with the frequency of the FPR will transmit through the walls, coupling into cladding modes and eventually experiencing high attenuation. However frequencies which are in anti-resonance will not propagate through the curved wall and will therefore guide inside the core along the fibre. The curvature of the inner core wall is important as this has an influence on the attenuation. The first unwanted mode which the light could couple into is the waveguide created by the nodes where the capillaries meet (see Figure 67 yellow circle), therefore the larger the physical distance of this waveguide is from the core the lower probability of mode coupling, hence leading to a lower attenuation. As Lichinister pointed out this fibre is a type of "leaky mode" fibre, as they never have true confinement of the light.

For a more detailed description of the theory of ARROW guidance see the introduction Chapter, § 1.3.3.

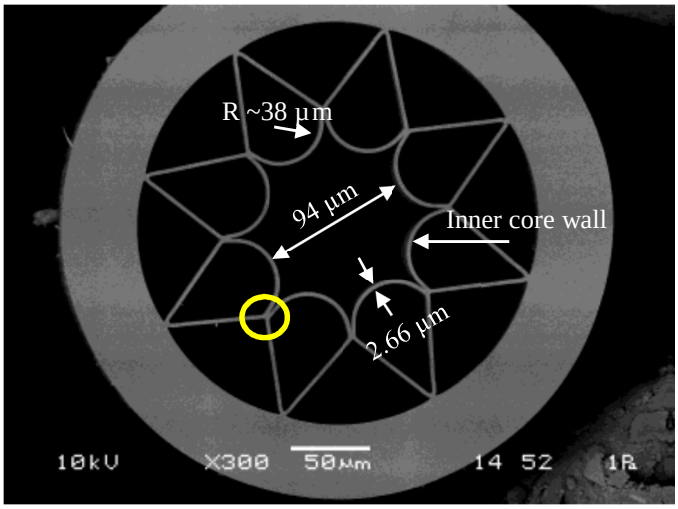

Figure 67: SEM micrograph of the negative curvature fibre used in this work. The core diameter (narrowest distance between two inner walls) was 94 µm, the inner wall thickness was 2.66 µm bent with a radius of 38 µm. The nodes where two capillaries meet (yellow circle) are the first structures which support (unwanted) modes.

4.2 Fibre Fabrication

The HC-NCF was fabricated in the same manner as the HC-PCF (3.1.1) using the stack and draw method. However in this case the preform was much simpler to prepare as the inner structure was made up of a single ring design (Figure 68). The inner structure is originally composed of 8 round thin-walled fused silica tubes (Suprasil F300). The triangle shape as seen in Figure 67 is the result of pressure difference in the core and surrounding lattice area during the drawing process. As the low attenuation area is strongly dependent on the wall thickness it is important to adjust precisely the pressure to control this. The pressure difference between the cladding and the core was about 8 kPa. In this case this resulted in an inner wall thickness of 2.66 µm and a core diameter of 94 µm. The core diameter was defined as the narrowest distance of two opposite curved walls. The radius of curvature of the inner wall is 38 µm.

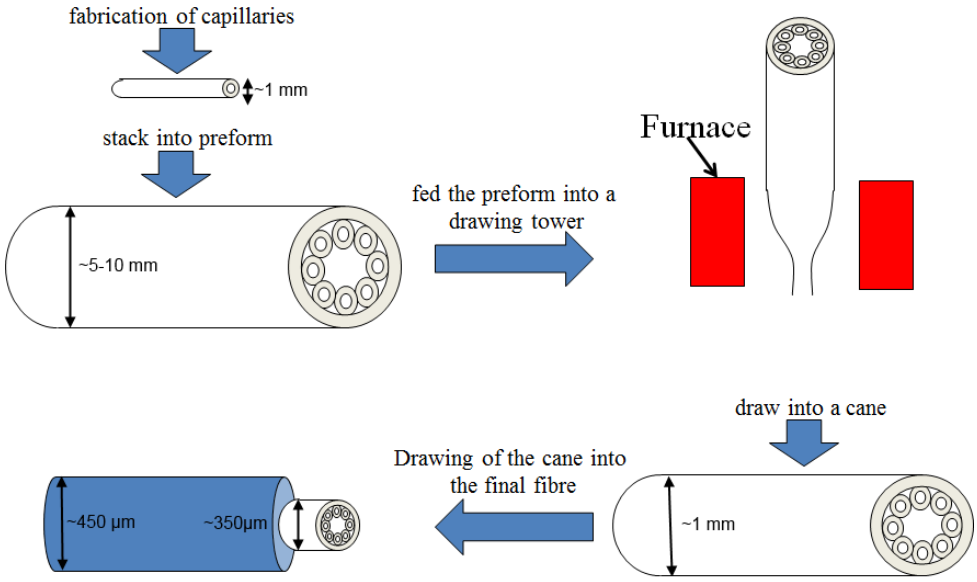

Figure 68: Fabrication of the HC-NCF using the stack and draw technique. The preform consists of 8 identical round capillaries made out of silica (Suprasil F300). The triangular shape of the inner structure is due to the pressure difference applied during the drawing of the cane into the fibre. In the final step a protective polymer coating is applied.

4.3 Attenuation

The attenuation is limited by the core modes which can couple into modes within the surrounding structure. Two different modes are present in the structure; one is the mode in the uniform curved core wall and the second one is the glass waveguide which is formed around the core at the nodes where adjacent capillaries touch (as shown in Figure 67). By increasing the core wall curvature the distance between the core mode and the

glass waveguide can be increased and therefore the attenuation decreased [114]. The attenuation of the fibre is shown in Figure 69.

The measurement was carried out using the cut-back method from 83 m down to 3.1 m, with a tungsten halogen bulb as the light source and a Bentham TMC300 monochromator set to a resolution of 10 nm. The fibre was bent with a diameter of > 1 m. This measurement was done at the University of Bath by Fei Yu a PhD student in the group of Prof. J. Knight.

Two low loss spectra are present in the fibre, the first from 2-2.5 µm and a second from 2.8-3.8 µm. Between 2.5 µm and 2.8 µm is a high loss region as is expected as the wall thickness is 2.66 µm and therefore propagation through to the inner wall is possible.

At 2.94 µm the attenuation is around 60 dB/km. The absorption peaks in the region from 3.25 µm and 3.7 µm are a result of HCl contamination within the glass, which was introduced during the glass capillary production. As is described in [114] these peaks overlap with the absorption peaks of HCl and can be erased if purified with nitrogen or, for shorter pieces (~5 m), leaving the fibre in a desiccator for at least 24h.

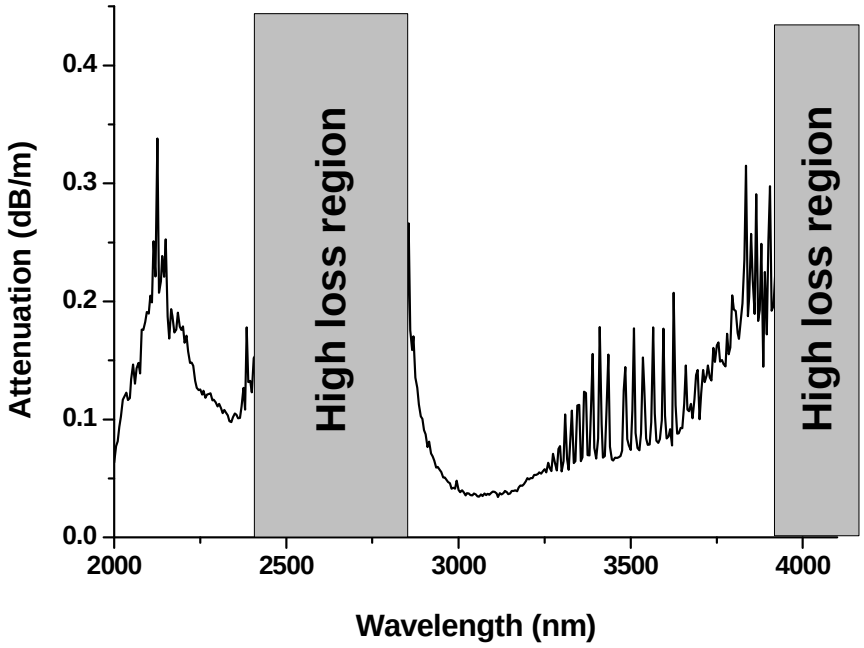

Figure 69: Optical loss spectrum of the HC-NCF fibre presented in this work. The attenuation at 2.94 µm is 60dB/km. The measurement was done by the group of Prof. J. Knight at the University of bath, UK.

To verify this measurement we conducted a cut-back measurement of the fibre in our facilities. Both ends of the fibre where held straight and the fibre was bent with a diameter of 50 cm. The bent part of the fibre correlates to 5.5 full circles. The initial length of the fibre was 9.55 m and a 3 m long piece was cut back, which corresponds to two full circles.

The attenuation measured for this configuration was 0.183 dB/m. This is a factor of 3 higher than the losses reported previously [3]. Several factors could be responsible for this difference in attenuation. First, the methodology of the two measurements is different. The bend diameter differed from <1 m to~ 0.5 m, also it is likely that micro-bends were present where the fibre was fixed, during the second measurement. As will be described later the fibre is sensitive to bends with radii < 0.15 m.

4.4 Output beam profile

An investigation of the fibre output beam profile was done by moving a HC-PCF transversely relative to the negative curvature fibre (HC-NCF).

Here a second, HC-PCF, fibre was aligned close to the HC-NCF and moved transversely relative to it (Figure 70). The "measuring" fibre was the HC-PCF as described in Chapter 3. Figure 70 shows an image from the top of the two fibres. The fibres shown in the image are deliberately cleaved non-perpendicularly to show the different structures. They were cleaved perpendicularly for the actual measurement. The output power of the HC-PCF was measured with a pyroelectric detector (Coherent P5-01). The position of the fibre was controlled with an LVDT (Tesa Tronic TTD20). The relative output power versus the fibre position is shown in Figure 71.

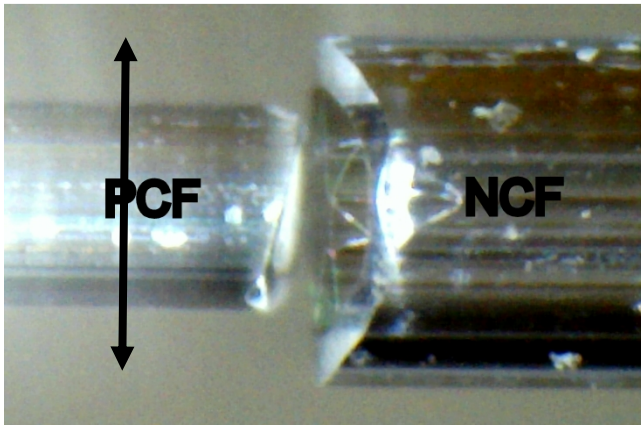

Figure 70: Measurement of the HC-NCF output beam profile using a HC-PCF which is moves transversely along the HC-NCF.

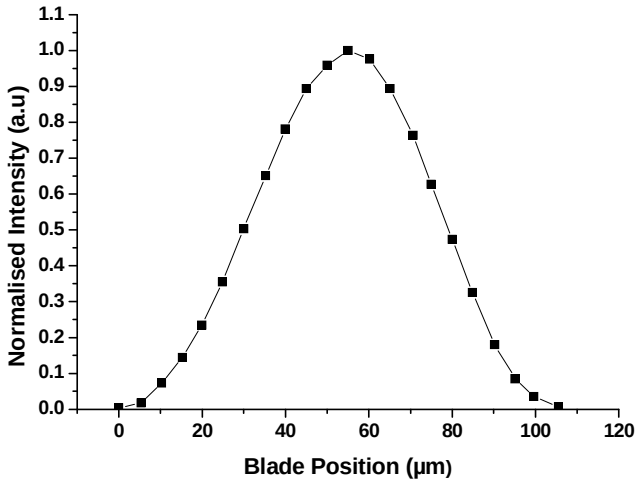

Figure 71: Fibre output beam profile measured by moving a HC- PCF transversal relative to the HC-NCF, resulting in a $1/e^2$ mode field diameter of 77.9 µm.

As can be seen from the measurement the output beam profile is single mode like and close to a Gaussian beam profile. From this measurement a $1/e^2$ mode field diameter of 77.9 µm can be calculated. However the exact mode field diameter is dependent on the fibre bend radius described in §4.6.

4.5 Coupling efficiency

To analyse the coupling efficiency into the fibre both Er:YAG laser systems (IMPEX and Sheaumann) were used. This was done to quantify the influence of the laser beam profile on the coupling efficiency. In both setups the alignment of the fibre was optimised by using a 3-axis micro-block with additional adjustment of pitch and jaw.

The average coupling efficiency into the HC-NCF fibre using the IMPEX laser is 31.6 ± 3.6%. Figure 72 shows the coupling efficiency versus the input pulse energy (15 Hz) which varies due to slight changes in the beam profile and dimensions with variation of the power output. For this experiment a 100 mm final focus calcium fluoride lens was used leading to a focus spot size of 67 µm and an NA of 0.07. As mentioned in Chapter §2.2.2 the beam quality of the IMPEX laser was not ideal with an M^2 of 2.5 this led to problems as the launch could not match the core diameter and NA of the fibre simultaneously, therefore a compromise had to be made.

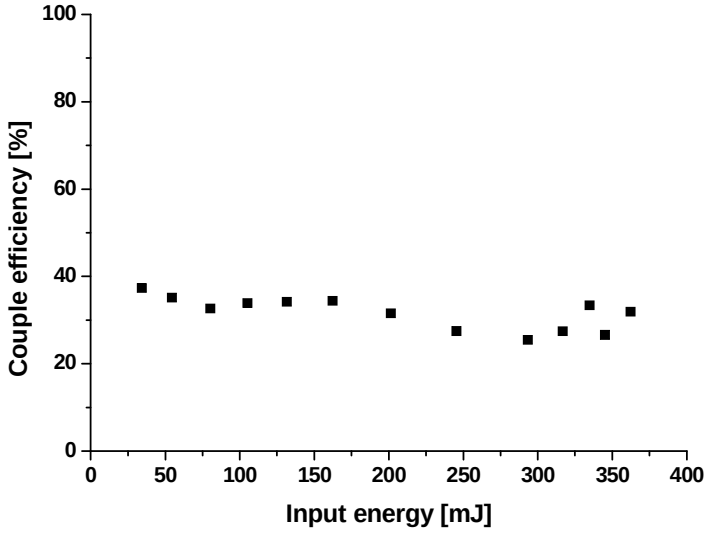

Figure 72: Coupling efficiency into the HC-NCF using the IMPEX laser system. The average coupling efficiency is 31.6 ± 3.6 %.

To optimise the coupling efficiency into the HC-NCF the Sheaumann laser system was used, which has a Gaussian beam profile and an M^2 of 1.4, matching the one of the fibre. Table 7 lists the different parameters investigated and the coupling achieved.

Table 7: Coupling efficiency into the HC-NCF using the Sheaumann laser system, with different final calcium fluoride lenses.

Final lens focal length/mm	Spot diameter/µm	NA	Couple efficiency
50	135	0.01	64%
26	73	0.049	82%
12	29	0.063	21%

It is obvious that the better beam profile led to a highly improved coupling of up to 82% if the focus spot diameter was 73 µm and a NA of 0.049. In this case the spot size was similar to the IMPEX laser setup, however the coupling was higher. The dependence of incident angle and coupling efficiency was also investigated and results are shown in Figure 73.

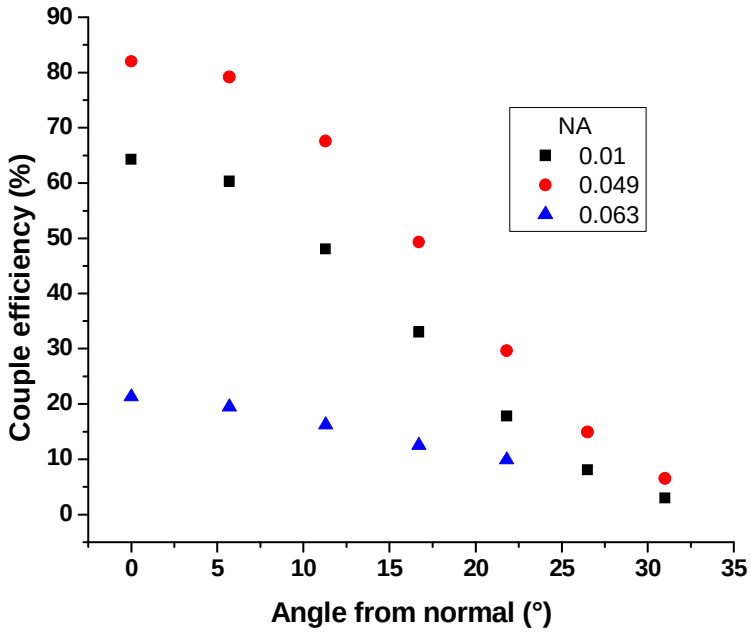

Figure 73: Coupling efficiency for non-normal HC-NCF fibre alignment, for different NA. The measurement was done using the Sheamann laser with a wavelength of 2.94 µm.

4.6 Bend sensitivity

An investigation of the bend sensitivity was performed using an MSquared Firefly-IR laser. This is a tuneable Optical Parametric Oscillator (OPO) laser system for the mid IR operating from 2.4 µm up to 3.7 µm. Due to the good laser beam quality (M^2 = 1.2) the spot size diameter and NA could be matched close to the HC-NCF fibre's values of 87 µm and 0.03, respectively.

The fibre measured was 123 cm long with a 180° bend of various radii. Figure 74 shows the losses due to the bend. The presented losses are the additional losses due to the bend e.g. the loss for the fibre in straight condition is subtracted. The measurements presented here are in the region 2.8 µm to 3.4 µm as the noise in the rest of the laser spectrum was too high to get any significant data.

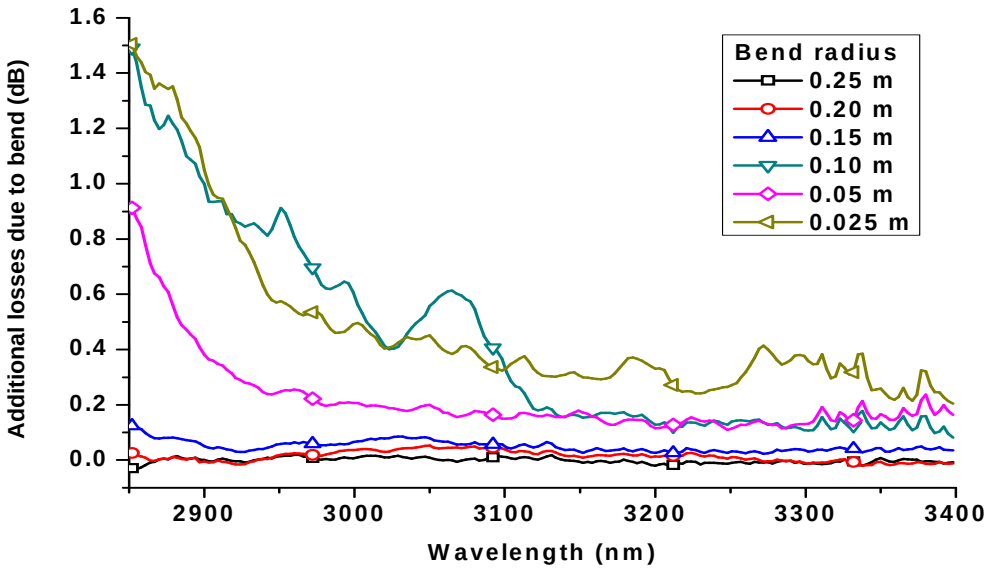

Figure 74: Additional losses for a 180° bent of the 123 cm long HC-NCF. The additional losses were noticeable if the fibre was bend tighter than 20 cm bend radius, especially for the shorter wavelengths.

From Figure 74 it can be seen that the fibre experiences no significant increase in attenuation down to a bend radius of 0.15 m. At tighter bends the attenuation increases specifically in the shorter wavelength regime (< 3 µm). An unexpected behaviour occurs for a 0.2 m bend, where the attenuation up to ~3.15 µm is higher than for a tighter bend of 0.1 m. Modelling of the losses due to the bending of the fibre was done at the University of Bath by Walter Belardi. The results are presented in Figure 75 for a HC-NCF designed to guide at 3 µm, as can be seen from this graph there is a peak of the losses at a bend diameter of 0.17 m. This is in close agreement with the experimental data measured in this work. The peak in the bending loss is due to a strong mode coupling between the core mode and cladding modes at this particular bend geometry identified by modelling the laser radiation distribution inside the fibre during bending. The difference between the experimental and modelled data in terms of absolute additional loss is attributed to the fact that the theoretical model is based on perfect system which does not take into account the imperfections of the fibre such as the variation of the wall thickness over the fibre length.

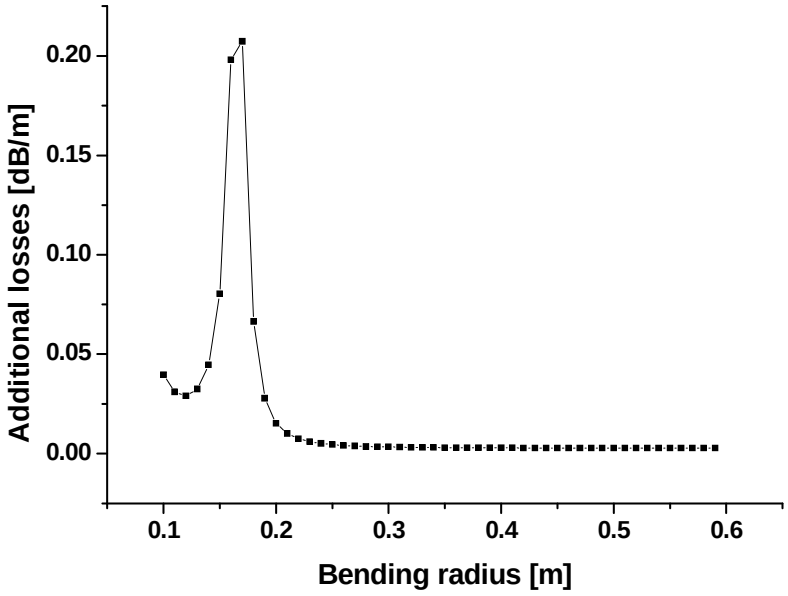

Figure 75: Modelled bending losses d of a HC-NCF for 3 µm guidance. The modelling was done by Walter Bernadi at the Bath University

The cross-section of the output beam profiles at a wavelength of 2.94 µm, for different bend diameters is given in Figure 76. For details on how these measurements were done see §4.4. The fibres were again bent to 180°. As can be seen the output beam diameter varies with the bend diameter. The detector area is about 24 µm in diameter (e.g. the core diameter of the HC-PCF), so the integration of the power over this area will lead to a "blurred" profile.

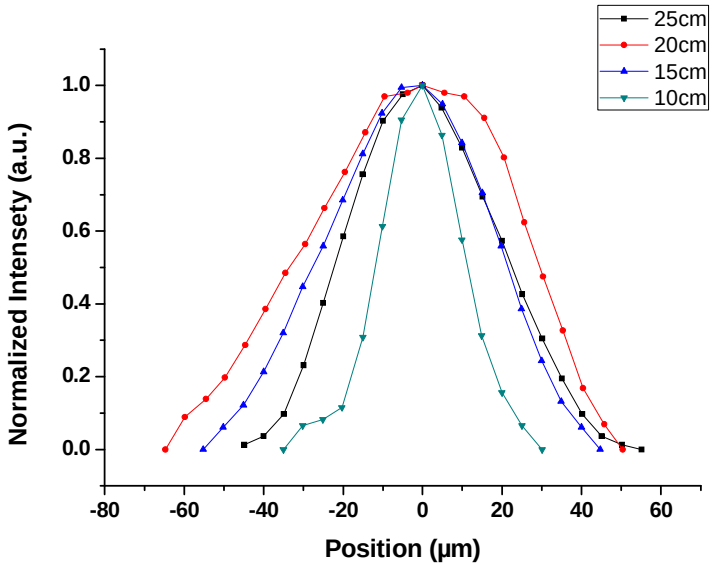

Figure 76: HC-NCF output beam profile for different bend diameters. Clearly the mode field diameter is dependent on the fibre bend radius.

4.7 High pulse energy delivery

For the pulse delivery investigation the IMPEX laser was used as described in (§2.2.2). The $1/e^2$ beam diameter onto the final lens was measured to be 13.8 mm. Using a final focusing lens with f=100 mm gives us a spot size of 67 µm and an NA of 0.07. Again due to the relatively poor laser beam quality a perfect match could not be achieved.

The maximal output energy delivered through the HC-NCF was 195.1 ± 1.32 mJ for a 33 cm long piece and 54.0 ± 3.81 mJ for a 9.88 m long piece of fibre. The short piece of fibre was held straight, whereas the long piece was bent with a diameter of ~ 0.5 m. These pulse energies translate to 2294 J/cm^2 and 763.5 J/cm^2 energy density at the end of the short and long fibre with a core diameter of 94 µm, respectively.

It should be noted that the limiting factor for the power delivery capability of the fibre was the output power of the laser itself. Both of the ends of the fibre, launching and output, were undamaged during all the transmission experiments.

4.8 M^2

The M^2 of the fibre was measured based on a $1/e^2$ beam diameter (according to ISO standard 11146) as 1.4 which is to be expected given with the near Gaussian output beam profile shown before. The fit between measurement and calculation is presented in Figure 77.

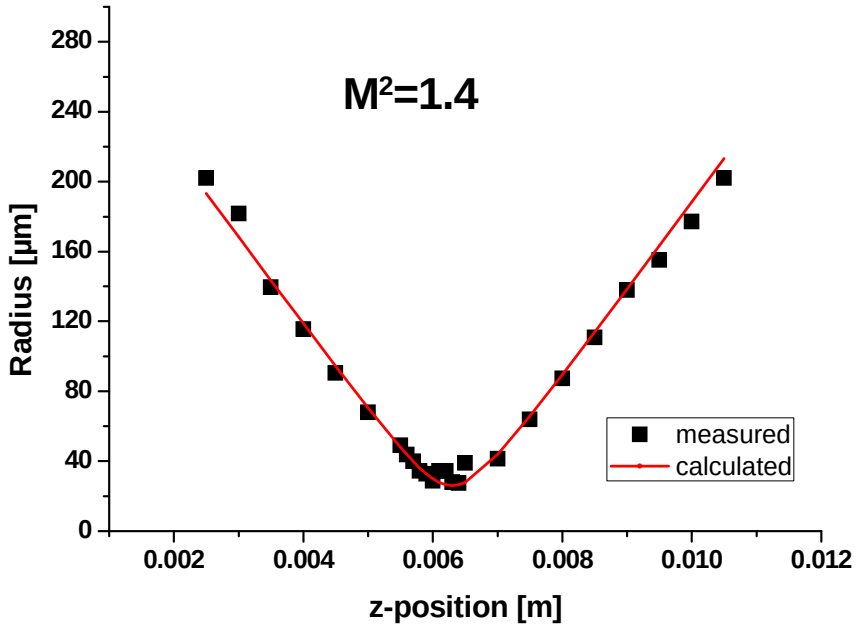

Figure 77: M^2fit and measurement for the HC-NCF using a value of 1.4. The laser used for this measurement was the IMPEX system with a wavelength of 2.94 µm.

4.9 Far-field behaviour

Of additional interest is the far-field behaviour of the output, as this is the beam profile that would be incident on the tissue if a surgeon would work with the fibre not in contact mode. Two different sets of test were carried out, one investigating the beam profile propagation at 10 mm to 100 mm from the fibre. The second test investigated the beam profile at a fixed distance for different fibre lengths. The images are captured from the reflection on a ceramic surface using an IR-camera (as described in material and methods §2.1.3).

The distances chosen (10 mm, 20 mm, 50 mm and 100 mm) represent envisaged working distances for non-contact surgical procedures. False colour images are presented in Figure 78. The fibre length was 6.48 m.

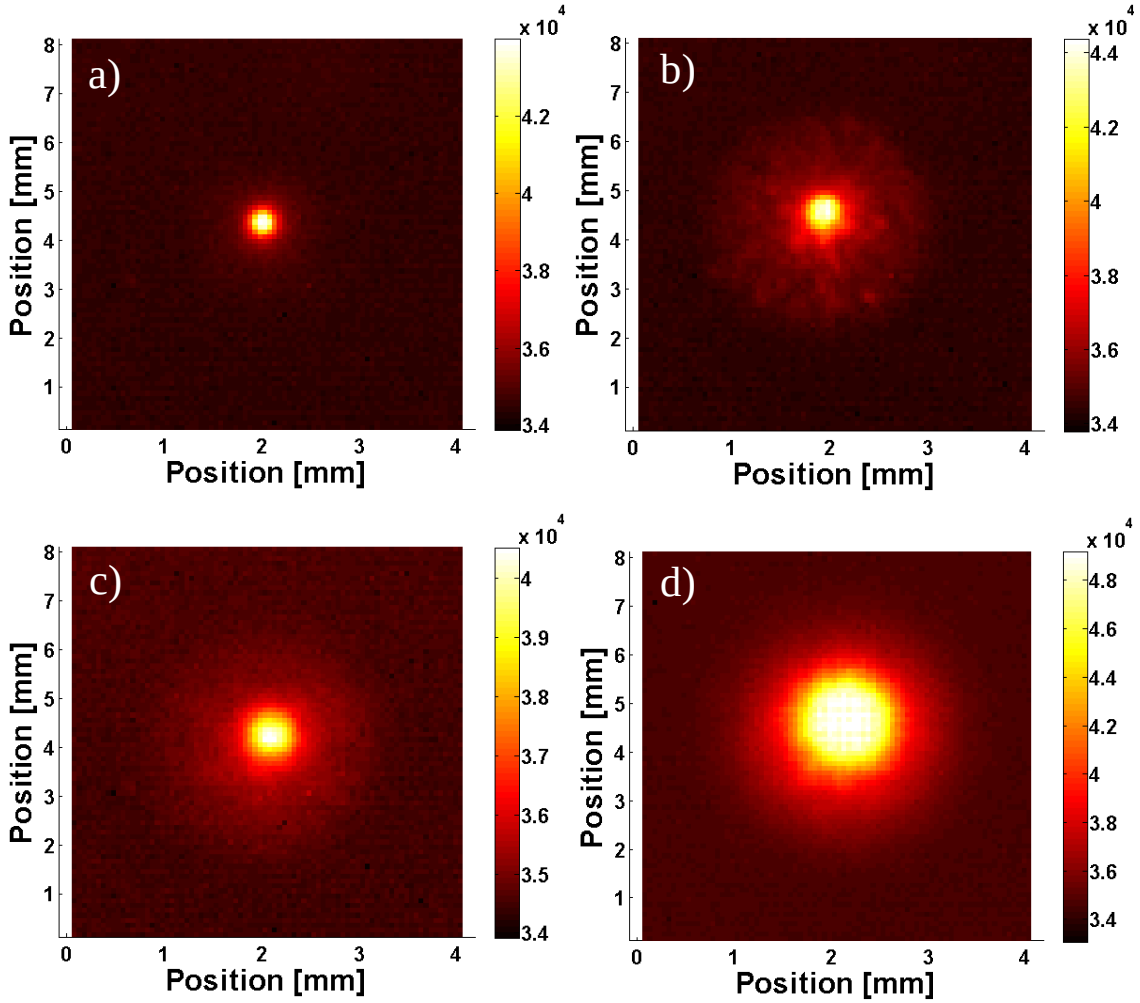

Figure 78: False colour far-field beam profile at different distances a) 10, b) 20, c) 50 and d) 100 mm) from the fibre end. The fibre length is 6.48 m. The laser used for this measurement was the IMPEX system with a wavelength of 2.94 µm.

The above figures show that the beam propagates in a single mode like manner and does not change drastically over the measured distance, as is typical for a Gaussian beam.

The next set of experiments compared the output beam profile at a distance of 25 cm from the fibre end to the ceramic surface for different fibre lengths. The measured lengths were 1 m, 2 m and 6.48 m. The 2 m long fibre was encapsulated with a sapphire endtip (§6). False colour images are shown in Figure 79.

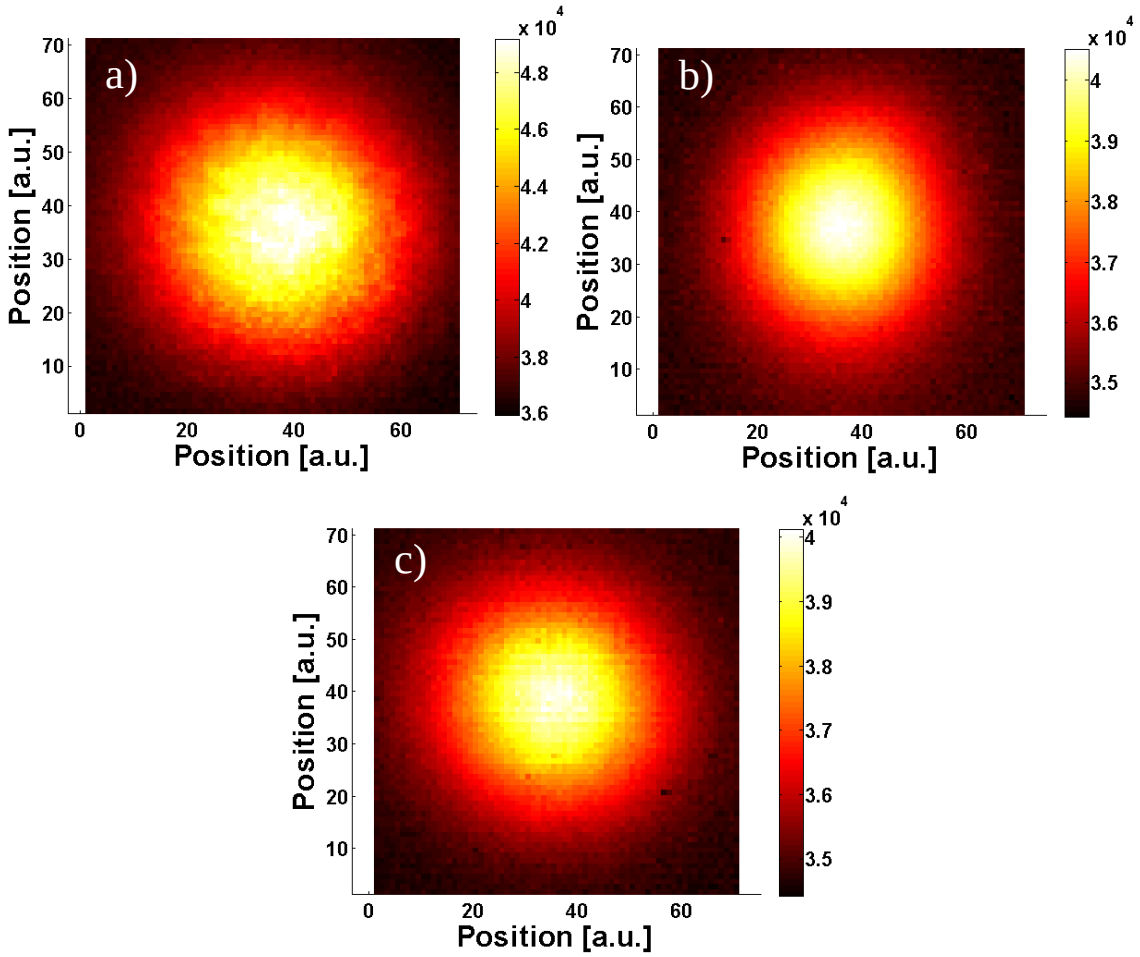

Figure 79: False colour output beam profile for different HC-NCF fibre length. All at a distance of 0.25 m from the fibre end: a) 1 m; b) 2 m with endtip and c) 6.48 m. The laser used for this measurement was the IMPEX system with a wavelength of 2.94 µm.

Again there is no significant difference in the beam profile even if the fibre is encapsulated with an endtip (Figure 78 b), for more details on encapsulation see Chapter §6. It should also be noted that the fibres were bent during this test with different undefined bend diameters but this does not affect the output only the intensity.

4.10 Autoclave

Autoclaving is a process used for medical instruments and devices to clean and sterilize them, using steam at elevated pressure and temperatures > 110°C. The fibres were autoclaved 3 times for 15 minutes at a temperature of 121°C and a pressure of 15 psi. To avoid any water vapour entering the hollow fibre, it was sealed by melting the ends of the fibre using a fusion splicer. Although no degradation could be detected during these repeated tests a larger sample size would be needed to be content of the reliability of the procedure. Also, no assessment of cleanliness or sterilisation effectiveness was carried out on the fibres after the process; here the aim was simply to demonstrate the fibre could survive the autoclaving process. Additionally, if the fibre were to be used in medical applications it is likely that it would be integrated into a microcannula or other similar device which would include extra packaging and coating.

4.11 Conclusions

The HC-NCF presented here was the first fibre with this single ring structure design operating at 2.94 µm. The outstanding feature was the single mode like beam profile which did not change with fibre bending. Even though the bend insensitivity was not as high as with the HC-PCF, it was still better than commercially available alternatives (like HWGs). Also in combination with the high coupling efficiency and the high pulse energy delivery capability it represents a very suitable flexible delivery system. The additional losses due to bending are minor with < 1 dB for a bend radius of 25 mm and could be overcome with a closed loop system to increase the power if the fibre is bent too tight. The autoclaving showed that there was no degradation measurable (at this point) which makes it attractive for medical applications, as it can be cleaned and reused, therefore reducing the overall cost of the system.

5 Evaluation and discussion of HC-PCF and HC-NCF performance

5.1 Fabrication of HC-PCF, HC-NCF and competing fibres

Several fabrication methods were used by different groups/manufactures for the manufacture of fibres suited for Er:YAG laser delivery (like chalcogenide fibres, sapphire fibres and HWGs) and will be summarized with their advantages and disadvantages analysed in the following paragraph. The practicality (and ultimately cost) of the fabrication process is an important consideration particularly if these fibres are to be used in commercial surgical laser systems and key if the process is to be scalable for mass manufacture.

Sapphire fibres are usually fabricated using the laser heated pedestal growth (LHPG) method, in which a sapphire rod is heated locally using a laser (commonly a CO_2-laser). A seed crystal is placed into the molten sapphire pool and drawn out, recrystallizing into a (single crystalline) sapphire fibre. A more detailed description with figures is given in §1.2.4. The advantage of this technique is that the fibre diameter can be easily changed by variation of the pull speed of the seed crystal/fibre. Also the theoretical length of the fibre is only limited by the initial rod volume (due to volume conservation). However, in many real systems the seed is fixed onto a translation stage with a finite movement which then determines the maximal fibre length although this can be easily overcome if the fibre is pulled using rollers instead of a translation stage. Another advantage is that there is little preparation of the material before the actual drawing of the fibre (e.g. no need for controlling dopant concentrations) and a multi crystalline sapphire rod can be used for the production of a single crystalline fibre. However, as the seed properties determine the structure of the fibre it is important to have a high quality single crystalline seed with a known and desired crystal orientation. This is a relatively slow process, the drawing speed of the seed is in the order of mm/min [private communication with James Sharp from Glasgow University] whereas in the case of silica fibres the draw speed can be up to 15 m/sec [137].

In comparison chalcogenide glasses need significant preparation before they can be drawn into a fibre, as the exact concentrations of the different elements inside the mixture has to be known. This dictates the optical and mechanical properties of the fibre. It is also important to have a high quality material for this first step as was demonstrated by [138-140] to achieve the minimum losses possible. Another issue during the fabrication of these fibres is that they can contain toxic material (e.g. As, Sb etc.) and therefore have to be handled with special care with special environmental concerns (e.g.

inside a glove-box/fume chamber). Several fabrication techniques are used to produce these fibres, an often used one is the double crucible technique [141] in which case the core is drawn from a molten pool and the cladding is then melted around the core in a second drawing step. A schematic of this technique is shown in Figure 80. The advantage of this method is that the fibre length is not limited by the process and also that the core and cladding diameter can again be easily changed by varying the draw speed. However this two flow method has the limitation that it only works if the material composition of the core has a higher melting point than the cladding mixture as otherwise when the cladding is applied the core would melt and lose its definition.

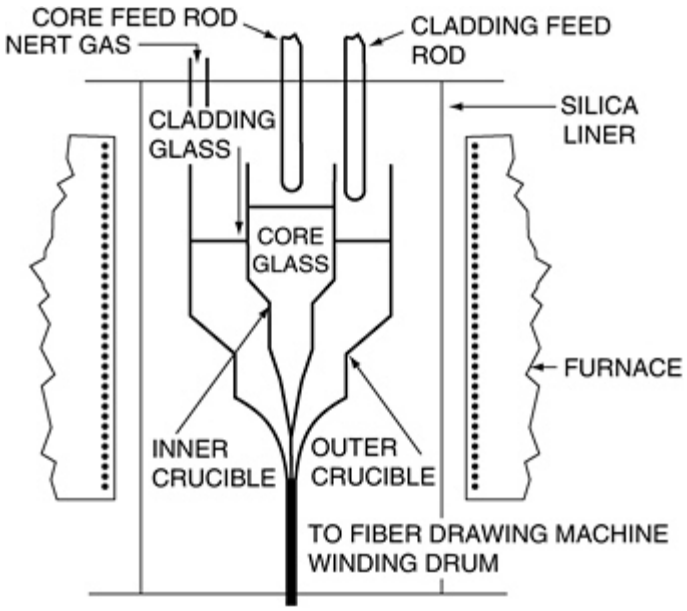

Figure 80: Simple schematics of the double crucible technique for chalcogenide fibres, in which the cladding layer is molten around the core. picture is taken from [142].

Alternatively the fibres can be drawn from a monoindex [143] or core/clad. chalcogenide rod [144] similar to standard telecommunication fibres, but at lower temperatures. Also the extrusion technique is used to fabricate the preforms for the fibres and was pioneered by Seddon, Furniss et al. [145, 146]. The schematic setup for the process is shown in Figure 81. The glass billet is placed into a stainless steel barrel which is surrounded by an electric furnace. A stainless steel bobbin is used to seal the barrel and is driven by a punch which is driven by a hydraulic cylinder, and pushes the glass melt through the die. The temperature of the die is measured by a thermocouple and the force applied onto the bobbin by a load cell.

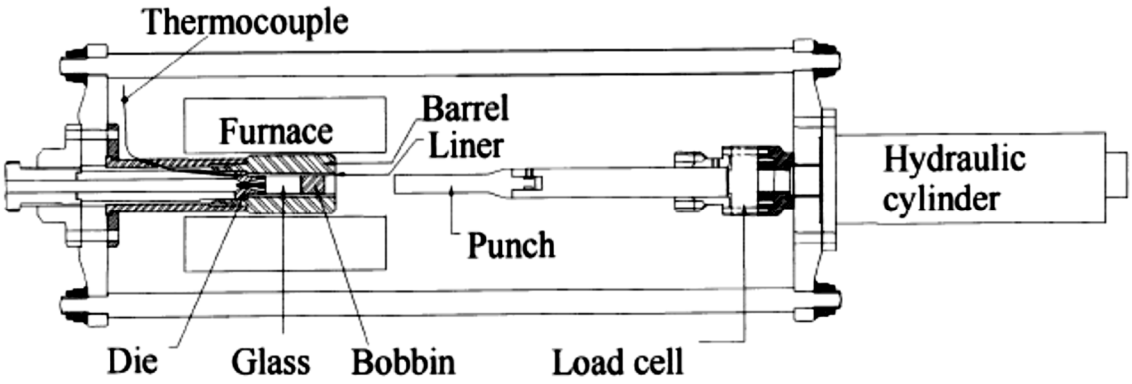

Figure 81: Schematic of the extrusion process used for chalcogenide fibres. The extruder is shown in the horizontal position with the punch withdrawn. The end-to-end dimension is about 1.75 m. The furnace is shown schematically in place around the barrel. The measuring thermocouple is located close to the die. For clarity, the extruder support frame, water-cooling and optional inert gas flow have been omitted. Presented in [146].

HWGs are fabricated using several different fabrication techniques like: physical vapour deposition, electroplating, liquid phase formation, sputtering and the wet-chemistry process. The details about the wet-chemistry process, which is the most common, is described in §1.2.5. One of the main factors which influence the attenuation of the fibre is the smoothness and uniformity of the layers which are deposited inside the fibre, therefore it is important to control these during the fabrication. Advantages of this process are that it can be easily modified for different wavelengths by changing the layer thicknesses and that the capillary can be fabricated from different materials (e.g. silica or Pyrex-glass) enabling it to be potentially quite cost-efficient. However a significant limitation at the moment is the ability to fabricate small diameter (> 100 µm) long (> 3 m) fibres as a uniform layer is required inside the fibre. Small diameters and long fibre lengths lead to a decrease in deposited material from the fibre top to end (see Figure 24) as the concentration of the Ag and iodine solution decreases. A method to overcome this is by applying the layers on the outside of the silica/polymer capillary [88, 147], however for this the capillary has to be relatively thin-walled (> 10 µm) and uniform, which can be controlled by the fibre drawing speed.

The hollow core fibres presented in this work are fabricated from a single bulk material (fused silica Suprasil F300), which was supplied in hollow tubes with an OD of around 1-3 mm (depending on the preform). This is readily supplied in high purity although it is important to understand the OH concentration in the material. This is also nontoxic and therefore easier to handle during the fabrication. Also, the fabrication process can be carried out in an uncontrolled atmosphere although a clean room environment is required to minimise contamination from particulates such as dust. The

maximum fibre length which can be drawn is dependent on the preform size (volume conservation) and can easily achieve kms demonstrating that this can be scalable for high volume production if the demand required. The guidance band can be adjusted by changing the pressure difference between the core and cladding structure to control the relative sizes (pitch, diameter, wall thickness) of the cladding although understanding the effect of these parameters on the final fibre requires significant experimental effort. However, the core size is determined by the guidance region and cannot be easily changed without changing guidance properties, as in the case of the HWG. The core of a HC-PCF can be increased by removing 19 cells, without changing the bandgap of the fibre, however this leads to a multimode guidance of the fibre. The initial stacking of the preform can be complex and time consuming if a HC-PCF is to be fabricated, however due to the very simple one ring structure of the HC-NCF the stacking time can be significantly reduced. This simple structure also enables the use of other, normally hard to implement, materials like chalcogenide glasses [120] into a microstructure fibre to extend the guidance regime.

5.2 Attenuation

The fibres used in this work were shown to have attenuations of 1.1 dB/m and 0.18 dB/m at 2.94 µm for the HC-PCF and the HC-NCF respectively. These compare well to the other fibres designed for these wavelengths (see Table 8). Fibres with similar or lower attenuation have been reported for this wavelength, 0.4 dB/m [86] for a HWG and 0.11 dB/m for a fluoride glass fibre [72]. However, these alternative fibres have the issue associated with multimode guidance, as was discussed in the introduction (§1.2.3 and §1.2.5), and will be compared in §5.4 in more detail. The applications (e.g. medical and sensing) for which such fibres are used and designed generally do not require very long fibre lengths (longer than several meters), therefore the attenuations of the fibres are not as important as other factors like the ability to guide high energy pulses, the bend sensitivity or the guided mode(s)/beam profile at the fibre output providing that the increased absorption does not lead to damage or the fibre. Therefore it would be misleading to compare the fibres simply by their attenuation per meter. Specifically some of the fibres can be produced only in short lengths and/or tend to be (highly) bend sensitive or cannot deliver high enough energy pulses. They therefore are not necessarily better suited for the medical application, which is the application investigated in this work.

Nevertheless it is clear that the HC-PCF and HC-NCF represent an attractive alternative to existing fibres for guidance in this region. It should also be noted that the fibres presented here exhibit the lowest losses reported in the world to date [148, 149] for fibres fabricated entirely from silica at 2.94 µm. This is clearly a step change in silica fibre technology and readily demonstrates that, by using novel microstructures, silica can be extended for use in the mid-infrared region.

5.3 High energy power delivery

High energy pulse delivery has been demonstrated using HWGs (up to 1.7 J [134]), sapphire fibre (up to 600 mJ [75]) and germanium oxide glass fibres (20 mJ [69]), however these tend to have a large core and therefore multimode guidance. The large core is necessary for solid core fibres to overcome the material LIDT by increasing the area and therefore decreases the fluency. The HWG however can have a relatively small core diameter and still deliver high energy pulses (250 µm with 64 mJ delivery [87]). In these fibres, as is the case for the HC-PCF and HC-NCF, the light is guided mainly through air and therefore the LIDT is increased. In direct comparison the fibres presented here, deliver relatively low energy pulses with 14 mJ and 195 mJ through the HC-PCF and HC-NCF, respectively. However, it should be noted that in the case of the HC-NCF the maximal output energy was limited by the laser source. Considering the fluence through the different fibres however it can be seen that both fibres can achieve higher values than the established fibres they are compared to. The maximal fluence delivered through the HC-PCF was > 3200 J/cm^2; for the shorter (~40 cm) HC-NCF > 2200 J/cm^2; and > 700 J/cm^2 for a 9.55 m long HC-NCF. The HWG delivered ~ 216 J/cm^2 for a 1 mm diameter and 130 J/cm^2 for a 250 µm diameter fibre, respectively. With the sapphire fibre (600 mJ through a 340 µm diameter fibre) a fluence of ~660 J/cm^2 could be achieved and in the case of the germanium oxide fibre (20 mJ through 250 µm) a maximal fluence of ~ 40 J/cm^2 could be reported. All these fluencies are sufficient to ablate human dental enamel, which has an ablation threshold of ~35 J/cm^2.

As seen from the presented values the two hollow core fibres used for this work have much higher energy densities than established fibres, this is not due to the delivery of higher energy pulses but is result of the confinement in the relatively small diameter cores of these fibres. All the fibres can, however, deliver sufficient energy densities to ablate human dental enamel which has the highest ablation threshold as seen in Table 1. The very high energy densities of the HC-NCF will lead to carbonisation of tissue, as will

be demonstrated in §7, and are therefore not always desired as it leads to increased collateral tissue damage. However this enables new possibilities, using longer more flexible fibres while maintaining a high enough laser output to ablate biological tissue. This was demonstrated during this work by using a 9.5 m long fibre with an output energy density of over 700 J/cm^2 without damage to the fibre either at the launch or at bends. Losses due to bending and/or encapsulation could be compensated by the excess of energy if a closed loop (the fibre output energy is measured and a feedback system regulates the laser output) system can be implemented.

Finally, as the maximum delivered fluence is far in excess of that required for optimal tissue ablation, in a real application these fibres will be working well within the damage limit. This would ensure a significant safety factor and naturally this is of paramount importance when considering application of surgery on patients. Again, taking the above into consideration it is clear that the HC-NCF and the HC-NCF are promising candidates for the intended application.

5.4 Bend sensitivity

As is expected from the theory (§1.3.2) [96] and was shown experimentally in §3.5 the hollow core HC-PCF is essentially bend insensitive, even with very tight bends (down to 2.5 mm) there is no increase in the attenuation of the fibre, which is a unique feature of this fibre type. The reason for this insensitivity is the large index step between core and cladding ($\sim 2*10^{-2}$) [109], leading to a very tight confinement of the guided mode which results in robust guiding even with very tight bends (< 5 mm bent radius). In addition the beam profile does not change if the fibre is bent; it keeps its single mode like output beam profile even down to a bend radius of 2.5 mm.

HC-NCFs on the other hand exhibit bend sensitivity, as was demonstrated in §4.6 (Figure 74). The figure gives the additional losses due to a single 180° bend down to a bend radius of 25 mm, and it can be seen that there are negligible losses if the fibre is bent with a radius less than 150 m. With tighter bends the losses increase up to 0.9 dB at 2.94 µm and a bend radius of 100 mm, however it is noticeable that when the fibre is bent over this “critical” bend radius the additional losses decrease again to 0.7 dB and 0.3 dB for 25 mm and 50 mm bend radius, respectively. As is described in §4.6 this effect is due to mode coupling from core to cladding modes. However, it should be highlighted that even with a bend radius of 2.5 cm the fibre is still able to deliver sufficient energy for tissue ablation. As discussed above it could be envisaged that using a closed loop control

that would adjust the laser power as the fibre is bent could compensate for the additional bending loss and hence maintain a constant fluence on the tissue.

The losses are distributed through the bent section of the fibre, measured using a thermal imaging camera (FLIR i7), shown in Figure 82 where the fibre can be seen as the red curve. The laser light was coupled into the fibre from the left side of the bend and exits it on the right side. In the presented image the output energy was set to 50 mJ (~ 720 J/cm^2) for a fibre length of ~ 1.5 m bend with a radius of 10 cm, with the maximal temperature of the fibre reaching ~23°C. This temperature is under the critical temperature of 40°C for endoscopes and therefore could be used in such even if the fibre is bent to 10 cm bend radius.

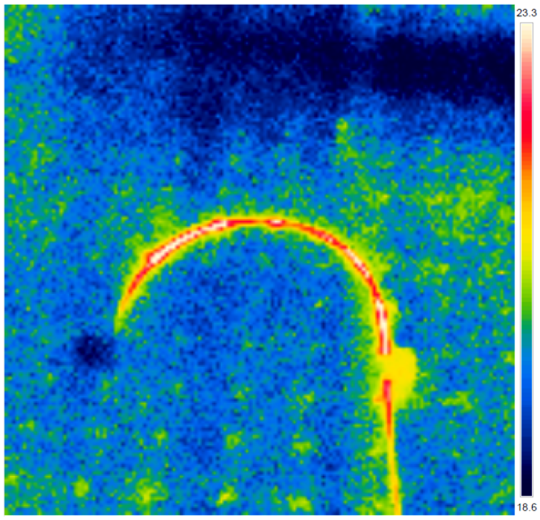

Figure 82: Thermal imaging of a HC-NCF bend with a radius of 10 cm. The maximal temperature of the fibre is ~23°C. The temperature increases from blue to white (which is not saturation). During the image taking a pulse energy of 50 mJ (720 J/cm^2) from the IMPEX laser with a wavelength of 2.94 µm was coupled into the fibre from the left hand side.

Even though the output beam profile changes in overall diameter (40 µm to 10 µm) when the HC-NCF is bent it does not change its overall shape of a single mode like Gaussian like profile. The change in beam diameter does have influence on the usability in surgical applications, as this changes the fluence and therefore can lead to too much energy (carbonization and/or collateral damage) or not enough energy (no ablation). If a region of fluencies can be established which is suitable for certain procedures and tissues the laser output power can be adjusted accordingly. An advantage of this fibre (and HWGs) in this respect is the low divergence angle, leading to a lower influence of this fluctuation of the beam diameter if the distance between tissue and fibre is variable. Further experiments have to show the practical implications and limitations due to this effect.

In (multimode) solid core fibres the bending attenuation increases sharply when near the angle of $\theta = \theta_c(1-2\alpha/R\theta_c^2)^{1/2}$ where θ_c is the critical angle (maximum launching angle), α the core radius and R the bending radius [150]. Higher order modes get cut off if the fibre is bent tighter than leading to higher attenuation, e.g. a multimode fibre with a core of 50 µm has a critical bending radius of 10 mm at a wavelength of 1300 nm [Corning Inc. data sheet [151]]. However as was shown by Kotsifaki et al. [72] this can be avoided if the launching angle into the fibre is small enough. In this way it could be shown that ZBLAN fibres with different diameters (448 µm, 465 µm and 620 µm) did not show any significant dependence of the attenuation versus bend diameter (see Figure 15), if a free running (in contrast to a Q-switched) Er:YAG laser was used. The laser emitted pulses with a duration of 80 µs at a repetition rate of 1 Hz and a maximum output energy of 500 mJ.

In comparison to the solid core fibres Figure 83 shows the attenuation dependence with bending of a HWG [86].

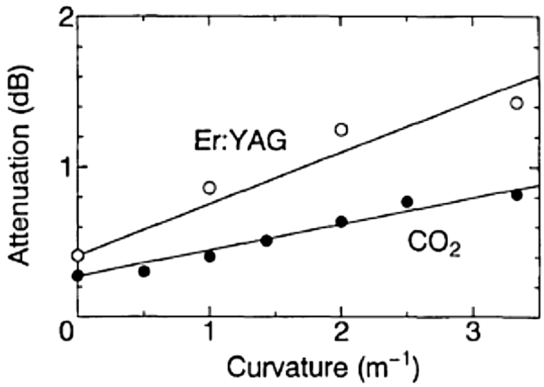

Figure 83: Bending losses of HWGs for CO_2 and Er:YAG wavelength as presented in [86]. The Er:YAG laser had an output energy of 100 mJ wit a repetition rate of 3 Hz, no information is given on the pulse duration.

The additional loss due to a 180° bend with a radius of 15 cm is 1 dB for a HWG with an inner diameter of 1 mm. Generally the reason for the bend sensitivity of HWG is the different guiding mechanism, which depends on the reflection of the light from the fibre wall; higher order modes exhibit higher losses in these fibres as they are reflected more often from wall to wall compared to low order modes. When a HWG is bent, coupling from low order modes into higher order modes is introduced and therefore leads to the higher attenuation of the fibre, this can also lead to a degradation of the output beam profile. More details about the dependence of the attenuation on the bending radius of the waveguide is given in the literature review (§1.3) and in [83].

Considering only bend sensitivity the HC-PCF shows clear advantages compared to the other presented fibres as there was no measurable additional loss if the fibre is bent even at very low radii (> 2.5 mm). However the additional losses of the other fibres presented are in the order of ~ 1 dB for a 180° bend. These losses, which are acceptable for short fibre lengths, do not necessary limit the use of the fibres in certain applications as the output power can still be sufficient for medical or surgical applications. If an attenuation of 1 dB is assumed and an output energy density of 1.6 J/cm^2 is needed (ablation threshold for human skin) for a core diameter of 600 µm (used as a mean estimate as this core diameter could be fabricated with all standard techniques discussed above) ~50 mJ will have to be launched into the fibre before the bend. This is a value which all fibres could achieve.

Overall it is clear that the HC-PCF shows a significant advancement in terms of flexible delivery of Er:YAG lasers for surgical applications. The very small bend radii (<2.5 mm) will enable novel, minimally invasive procedures to be considered and developed in collaboration with clinicians and will be discussed in future work. Although the HC-NCF does exhibit bend sensitivity its performance is comparable to other large core fibres. Notably the HC-NCF was able to deliver sufficient fluence at bend radii of 2.5 cm which exceeds the performance of many alternative fibres.

5.5 Output beam profile

The last characteristic which will be compared between the fibres is the output beam profile and its variance due to fibre bending. The beam output profile is an important parameter for many applications, particularly for medical application as this can determine the minimum cutting width and the collateral damage. This is even more important when the fibre is used in a non-contact configuration, where the divergence of the beam leads to an increase of the effected tissue area. Also it has to be considered that higher order mode can have a higher divergence and therefore further increase the effected tissue area.

In paragraph §3.8 and §4.4 the output beam profiles of the HC-PCF and HC-NCF were presented for near-field and far-field in both a straight and bent condition. All the output beam profiles were single mode like and did not change in overall shape. Two samples of the beam profiles for the two fibres and different conditions are presented in Figure 84. These two images were chosen as they are a good representative for both fibre output beam profiles.

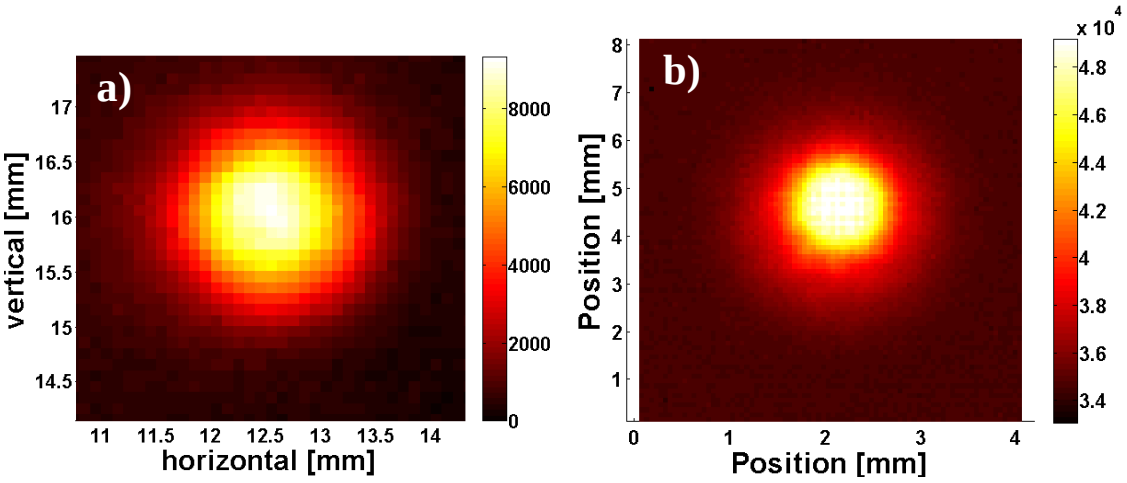

Figure 84: Output beam profile of the HC-PCF and HC-NCF fibres. a) Near-field image of the HC-PCF beam profile. b) Far-field of the HC-NCF beam profile.

Figure 85 shows the output beam profiles of germanium oxide, ZBLAN glass fibres, sapphire fibre and HWG for straight conditions.

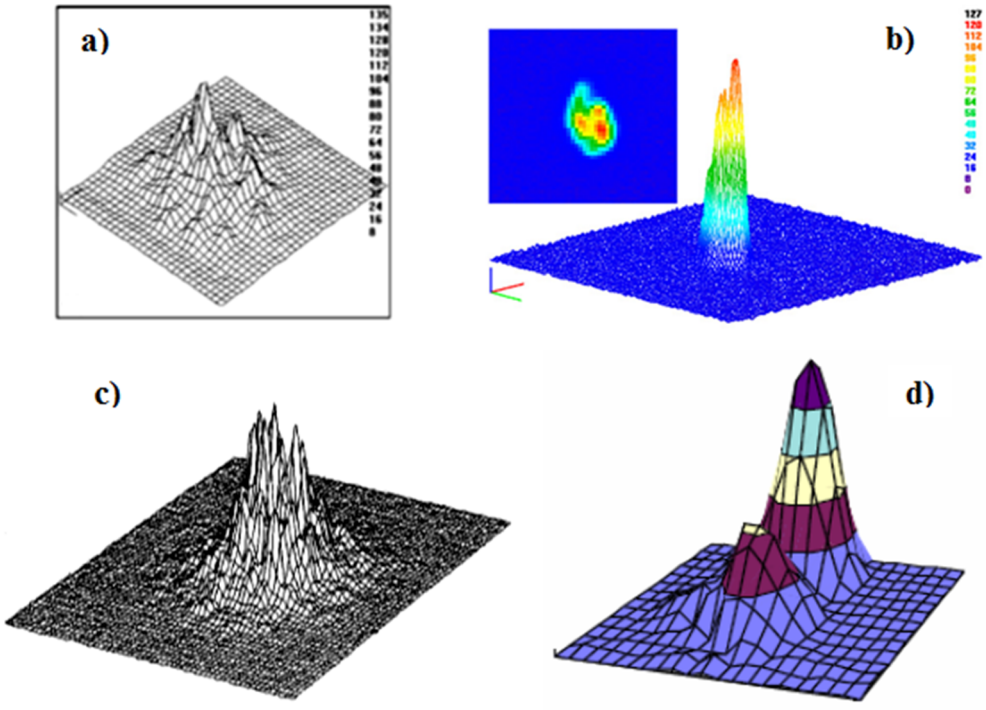

Figure 85: Output beam profiles for established fibres. All fibres were held straight and the diameter of the fibres is given in brackets: a) Germanium oxide fibre (250 µm) [69]; b) ZBLAN glass fibre (448 µm) [72]; c) Sapphire fibre (600 µm) [75] and d) HWG (530 µm) [80].

All of them have a multi-mode guidance which is seen in the output beam profile. Even though most of the beam profiles are centred around one central peak they still have multiple smaller peaks surrounding it. This uneven energy distribution can lead to uneven ablation patterns and therefore to unwanted collateral damage. If for example the output

beam profile of the HWG as seen in Figure 85d is used, the energy density in the valley between the two peaks could be too low to ablate tissue, which would lead to two separated cuts from the two individual peaks. This could be avoided by increasing the fibre output energy so that the energy density of the valley is over the ablation threshold of the tissue, however this can lead to too high energy densities at the peaks and therefore to unwanted carbonization.

In the case of the sapphire fibre it has been shown that the fibre can have a "shape cleaning" effect and that if a single mode beam profile is launched into the fibre this single mode is maintained under certain conditions (§1.2.3).

To underline the assumptions made before studies by Meister et al. [152, 153] showed that "hot spots" can lead to local ablation of dental enamel in an uneven manner, even if the average energy density is over the ablation density. As can be seen in Figure 86, a single pulse with an energy density of 50 J/cm^2 (beam diameter of 800 µm) and a TEM_{31} beam shape was applied onto dental enamel. The beam shape is clearly visible in the ablation sides of the material, where the beam regions with high intensity ablated the material deeper in concentric rings.

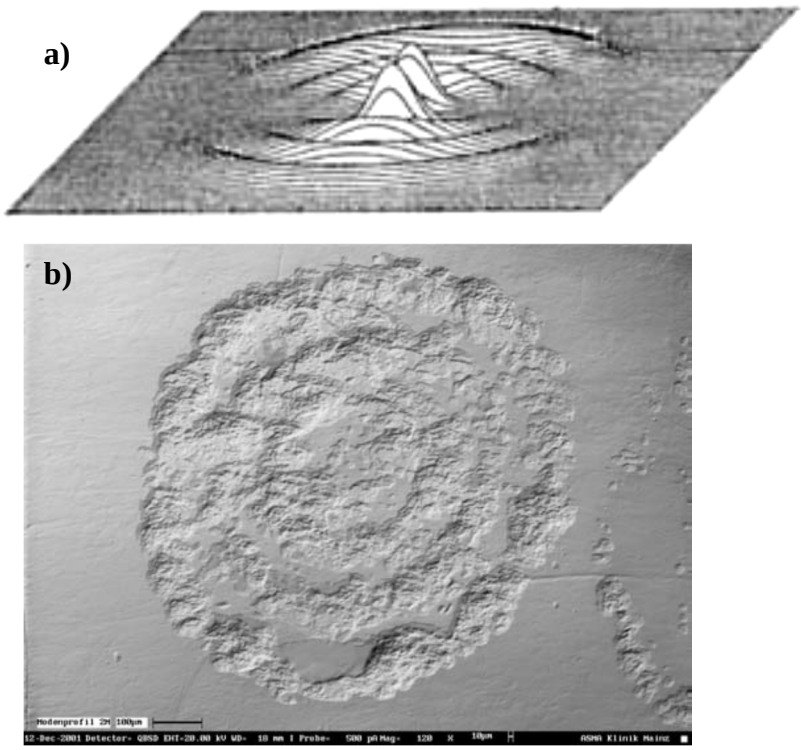

Figure 86: Influence of the laser beam profile on the ablation of dental enamel. The laser had a pulse duration of 150 µs and a variable repetition rate of 2 – 50 Hz. The beam was delivered using an articulated arm: a) Laser beam profile used (TEM_{31}) and b) Photograph of the ablation of a single laser pulse with a TEM_{31} mode structure in dental enamel at an energy E_{out} of 50 mJ. Presented in [152].

It should be noticed that, if (highly) multimode fibres are used in close proximity or contact mode, the effects of these hot spots are not necessary noticeable as the spot size is smaller. The smaller beam diameter can lead to an increase in the local energy density and therefore be over the ablation threshold over the whole beam profile.

In the literature review (§0) the bend sensitivity and the output beam profile for the different fibres was already discussed in detail. In summary all of the fibres output beam profiles change with a change of the fibre bent radius. Both the HC-PCF and HC-NCF show a reduced dependence of the output beam profile in comparison to these fibres particularly in the case of the HC-PCF which shows no bend dependence of the output profile even down to radii of 2.5 mm.

5.6 Conclusions

The comparison of established and commercially available HC-PCF and HC-NCF fibres was made in this Chapter. In detail the fabrication, attenuation, high energy delivery, bend sensitivity and output beam profiles were analysed. The presented fibres here have neither the lowest reported attenuation at 2.94 µm nor the highest achieved pulse energy delivery; however they combine the highest achieved energy density with single mode like guidance. This is the most outstanding feature of both fibres, as they maintain the same output beam profile shape even if the fibre is bent. Also there is no measurable additional loss due to bending of the HC-PCF even at very tight bend radii, < 2.5 mm. The HC-NCF on the other hand has bending losses comparable or better than the other fibres, however the additional losses are relatively low and even with tight bends (radius of 2.5 cm) the output energy is sufficient to ablate biological tissue. Combined with the fact the HC-PCF and HC-NCF are made entirely from silica it is clear that they both offer a mechanically and chemically robust solution for the flexible delivery of Er:YAG laser light for surgical applications.

Table 8: Summarised properties of fibres for the 2.94 µm wavelength. The power density is given for chalcogenide glass fibres as no information was given for the pulse energy and duration. (na -- not available).

Fibre type	**Min losses at 2.94 µm /dBm^{-1}**	**Max. delivered energy /mJ**	**Max. fluence at fibre output /Jcm^{-2}**	**Core diameter /µm**	**Min. bend radius reported /m**	**Add. Bend losses at min bend radius /dB**
HC-PCF	1.1	14	3200	24	0.0025	0
NC-NCF	0.18	195	2200	94	0.025	0.7
HWG	0.4	1700	210	1000	0.125	1.4
ZBLAN glass fibre	0.11	20	40	250	0.1	0
Sapphire	0.4	600	660	340	na	na
Chalcogenide glass fibre	0.013	NA	1.7 GW/cm^2	250	na	na

6 End encapsulation of hollow core fibres

6.1 Introduction

As described earlier using hollow-core fibre designs has many advantages over solid-cores. However there is one main issue if the fibre is to be used for medical applications: the possibility of contamination of the hollow-core with debris and fluid. When the core is contaminated, the material inside absorbs the laser radiation and is heated ultimately leading to destruction of the fibre (e.g. destruction of the HC-NCF when used as a drill as described in §7 and Figure 118). In the worst case scenario parts of the fibre could break away and damage the surrounding (biological) tissue. Naturally, this has to be addressed before the fibre can be used in practical medical devices and consequently a number of different solutions have been developed as described in §1.4.

An optical fibre end encapsulation system for medical application, in particular endoscopy, has to satisfy the following properties:

- Mechanically robust
- Chemically robust
- Non-toxic
- High temperature resistance (> 800 °C)
- High transparency at 2.94 µm (>90%)
- Hermetically sealed
- Small physical size (in the mm range)

The encapsulation system, or endtip, developed in this work for the hollow core fibre delivery system were based on a sapphire transmission window. Sapphire is a mechanically and chemically robust, non-toxic materials with a high temperature resistance. The transmission range for sapphire is shown in Figure 87 and was supplied by *Swiss Jewel Company Ltd*. The transmission window of sapphire ranges from 300 nm up to 5 µm.

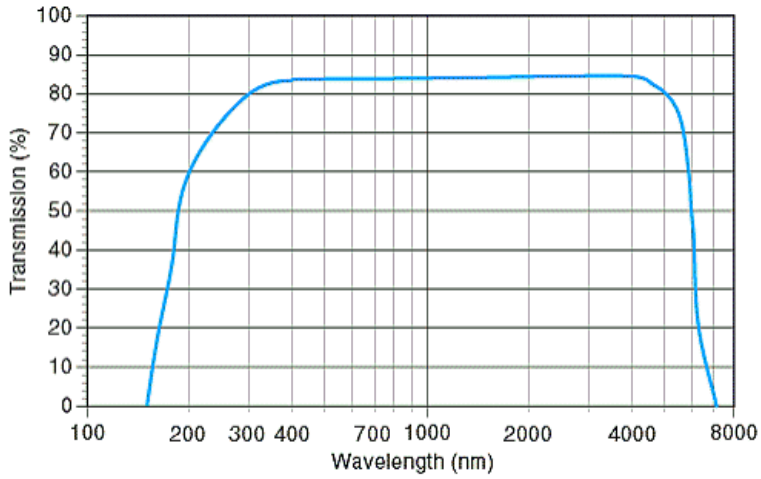

Figure 87: Transmission spectrum of sapphire from the supplier "Swiss Jewel Company for a 1 mm thick window.

A schematic diagram of the endtip is shown in Figure 88. A glass or sapphire tube/capillary is sealed with a sapphire "cork" or window. This endtip is subsequently mounted onto the hollow core fibre which provides a hermetic seal.

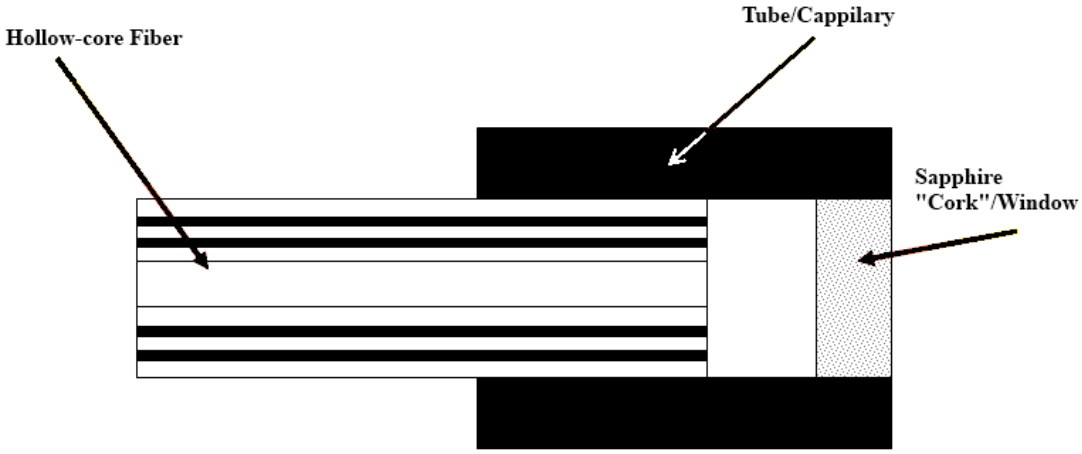

Figure 88: Schematic of an "endtip" presented in this work. It is based on a tube/capillary which is sealed with a sapphire window. This is than fixed onto the hollow core fibre. The dimensions are in the order of OD ~ 1 mm and 1 mm in length.

6.2 Tip realisation and fabrication

A number of methods to fix or bond a sapphire fibre/rod inside a capillary/tube were investigated. After the bond was cured the outstanding sapphire rod was cleaved and polished back to provide the window of the desired thickness. A schematic is shown in Figure 89.

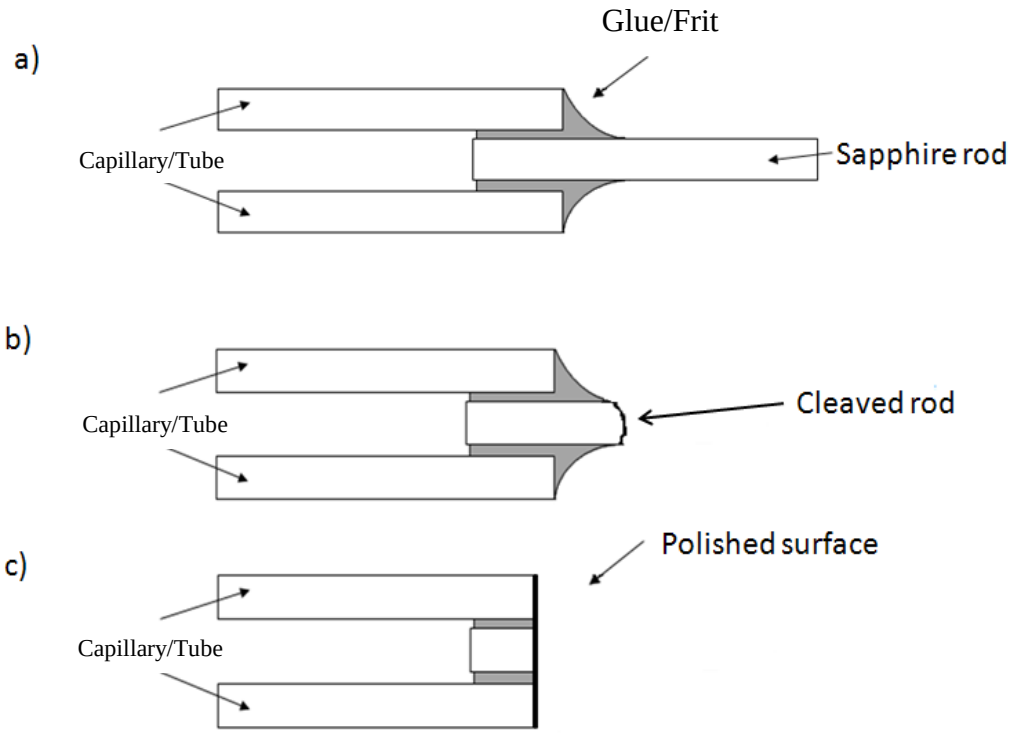

Figure 89: Schematic of the endtip fabrication process:
a) The sapphire fibre/rod is fixed with the capillary/tube using a glue or glass-frit;
b) The excess part of the fibre/rod is cleaved and c) the endtip is polished back to a desired window thickness.

6.2.1 Preparation and polishing of the sapphire fibre

The first stage in the fabrication of the endtip is preparation of the sapphire fibre, which was placed inside the capillary and to form the window. The fibre was supplied by *Goodfellow Cambridge Ltd*. and had an outer diameter of 150 µm (see Figure 90a). As can be seen in Figure 92 the fibre was not perfectly round. One face of the sapphire fibre had to be polished before it is fixed inside the glass capillary as the inner window surface could not be mechanically polished after it was part of the endtip.

One of the main reasons why sapphire was chosen as a material for the endtip window was its toughness (hardness 9 on the Mohr scale) but this also presents a problem if sapphire has to be machined or polished. Therefore the cleaving and polishing was relative difficult, compared to fused silica for example. To get a flat end surface, cleaving of the sapphire fibre was investigated. Cleaving with the York cleaver (FK11-STD) (Figure 90a) and the Fujikura (CT-07) (Figure 90b) produced a crack of around 200 µm along the fibre which would require significant polishing to remove and consequently would be time intensive. The best cleaving results were achieved by using a diamond (S90W from Thorlabs) or ceramic blade (Radiall F780) to cleave the fibre when bent by being taped on a surface (e.g. Post-it® notes block). The results using this method are

shown in Figure 90c and d and were the most viable option for the subsequent polishing procedure. As demonstrated it was not possible to get an optical grade end face from cleaving the fibre therefore polishing was unavoidable.

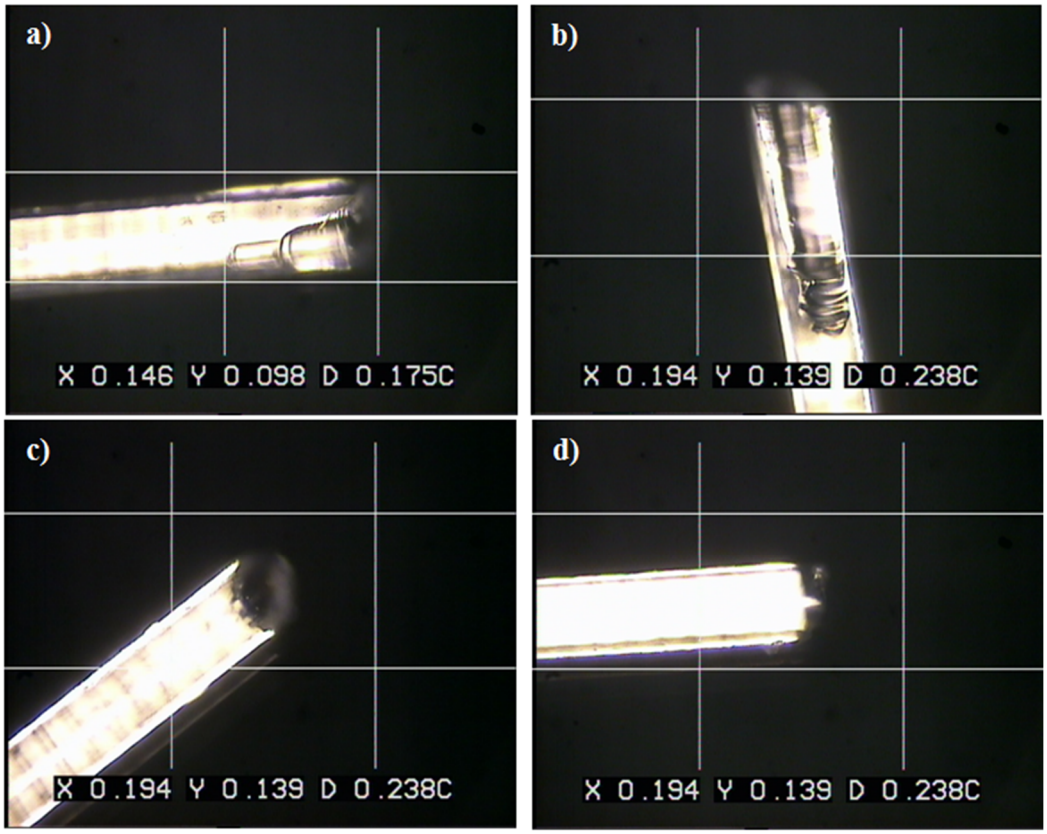

Figure 90: Cleaving of the sapphire fibre using different methods: a) York-Cleaver (FK11-STD); b) Fujikura-Cleaver (CT-07); c) Diamond blade (S90W) and d) Ceramic blade (Radiall F780).

For the polishing process a Buecher Fibrment (MA69-3000) fibre polisher was used and the fibres were mounted in a fibre mount which could hold up to 5 fibres at a time. To support the fibres during the polishing "cement wax" (Logitech 0CON-286) was poured around them (Figure 91). Figure 91a shows the closed mount with black lines which indicate the sapphire fibres inside and on the top surface the brown cement wax is visible. Figure 91b shows the open mount with a fibre lying in one of the groves. Another advantage of the wax is to increase the polishing area and therefore avoid scratching of the polishing sheets. However this could not always be avoided, as seen in Figure 92, where the yellow discoloration is part of the polishing sheet that was removed/scratched away by the sapphire fibre. Polishing sheets in descending order where used (with particle sizes of 12 µm, 9 µm, 3 µm, 1 µm and 0.3 µm) to produce a high quality optical finish (Figure 92).

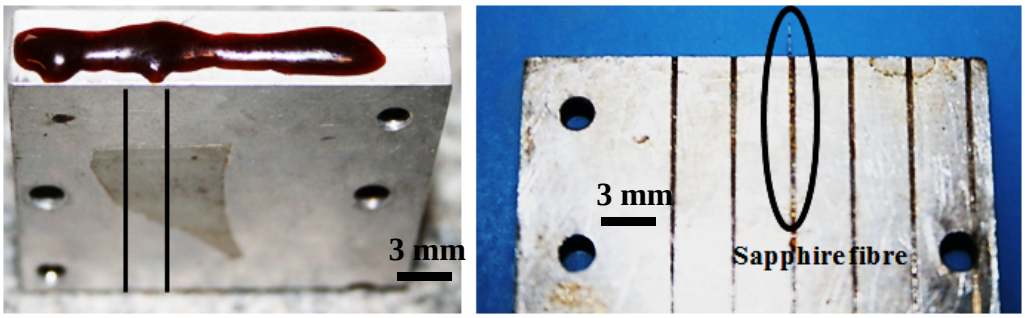

Figure 91: Sapphire fibre mounts: a) Closed mount, black lines indicating the fibres inside and b) Open mount with a fibre.

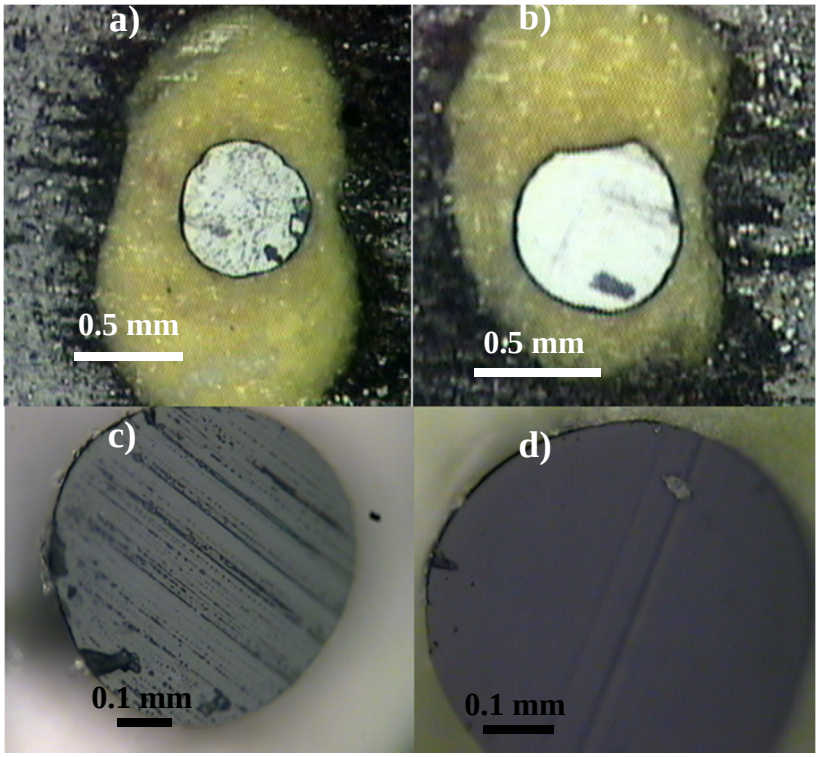

Figure 92: Polished sapphire fibres. Yellow discoloration is material from the polishing sheet. Polished with: a) 12 µm; b) 9 µm; c) 3 µm and d) 1 µm diamond polishing sheet.

Although the final polished end face (Figure 92 d)) had a scratch in the middle, most likely introduced by a broken piece of the fibre ripped on the polishing sheet. However the result demonstrates that the above is a viable processing route for fibre cleaving and polishing.

The first approach of bonding was trying to melt a fused silica glass capillary (TSP150655 from Polymicro) around a sapphire fibre, due to the natural tendency to build a sphere the glass should surround the sapphire fibre leading to a hermetic seal.

As described before the sapphire fibre was placed inside the capillary which was than melted around it. However due to the high difference in thermal expansion

coefficient (about 5.16×10^{-6} K^{-1}) between the fused silica glass capillary and the sapphire fibre, the silica glass capillary broke apart as it could not withstand the high stresses introduced. Unfortunately, as the glass failed in-situ it was not possible to take an image if it.

6.2.1.1 Tapering the silica glass capillary around the sapphire fibre aka "tapered tip"

The next approach to realise encapsulations of the fibre was the use a so called tapered tip design. In this case a short piece of sapphire fibre is placed into a fused silica glass capillary (TSP150655 from Polymicro), which is than locally heated. One side of the capillary is fixed and on the other side a force is applied. Due to this tension in the capillary it collapses at the locally heated section. A schematic of the setup is shown in Figure 93. The drag force was achieved by hanging a weight onto the loose end of the capillary; by changing the weight the tension of the capillary could be changed.

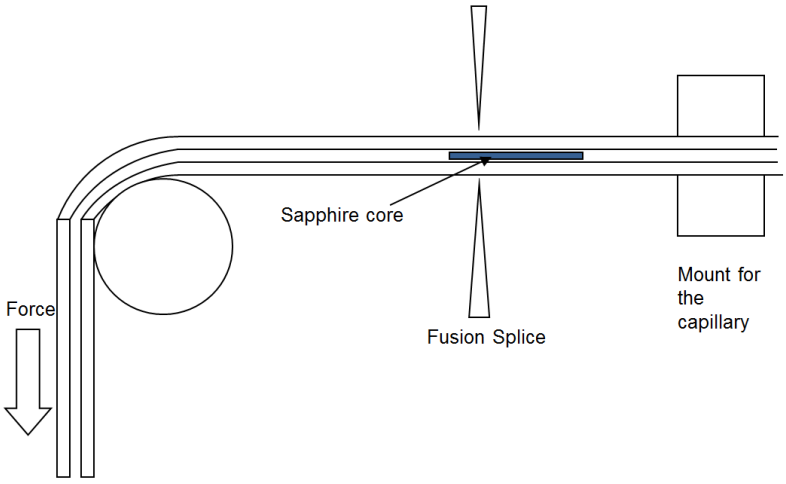

Figure 93: Schematic of the "shrink tip" setup. The silica capillary is fixed on one side and a force is applied on the other. A sapphire fibre is placed inside the silica capillary and located where the arc of the fusion splicer will be applied.

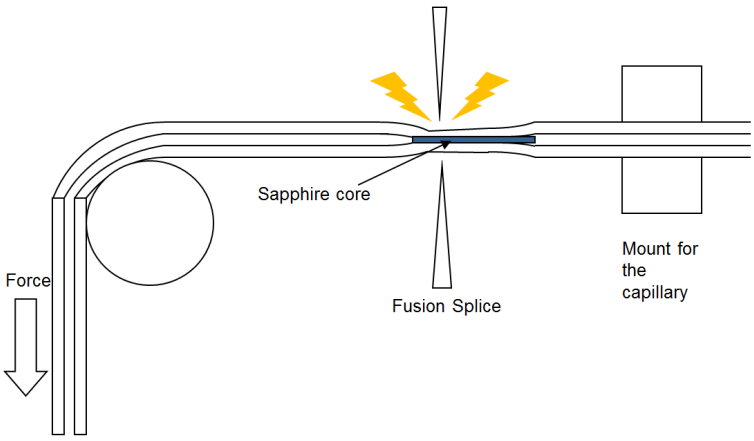

Figure 94: Schematic of the "tapered tip" setup. The silica capillary is locally heated over its T_g due to the tension of the silica capillary it will collapse at this heated location. The collapsed area encloses the sapphire fibre core.

The localised heating was done using an arc-fusion splicer (BIT Single Mode BFS 50). By changing the current through the arc and the duration the temperature of the glass and sapphire could be influenced. The settings best suitable were 12 mA for the arc current and duration of 4 s. Shorter times did not give enough time for the capillary to collapse and longer durations could not be set. Higher currents lead to failure of the capillary as the viscosity of the silica glass forming melt was too high, and lower currents gave not enough temperature rise so that the capillary did not collapse. The liquidus is the temperature at which crystals can form inside a liquid and co-exists with the melt, and in the case of Sapphire it is ~ 1800°C [154] and ~1720°C for fused silica glass [155]. The glass transition temperature for silica glass on the other hand is around 1200°C [156], so that the window of feasible temperatures where there is no crystallisation of the sapphire and no melting of the sapphire for this operation is between 1720°C and 1800°C.

The results of one of the tapers can be seen in Figure 95. The diameter of the glass capillary around the sapphire fibre is thinner (~280 µm) than the original capillary diameter of 350 µm. Also from the pictures it can be seen that the sapphire fibre piece used was not polished before inserted inside the capillary, as these tests were merely to find the right parameters and show the proof of principle the time consuming polishing process was be skipped.

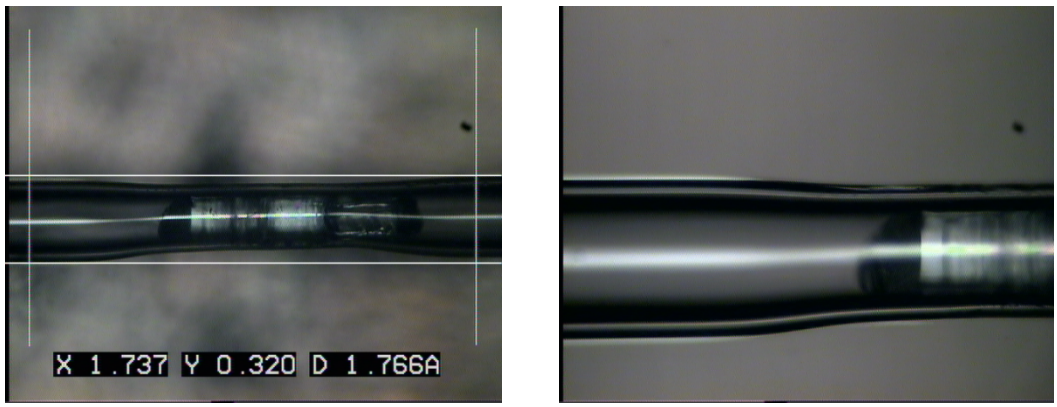

Figure 95: Fused silica glass capillary (TSP150655 from Polymicro) tapered around the sapphire fibre core using a fusion arc splicer.

After the shrink fitting the fused silica glass capillary and the sapphire were cleaved together using a ceramic blade, however most samples broke during this step. The surviving samples were mounted to be polished it back to the length of the “cork” which was required. The required length is dependent on the mode field diameter of the beam leaving the fibre and the distance between the window and the fibre. Depending on all

these parameter the laser beam diameter at the output side of the tip can be calculated/adjusted. The calculation could be done by simple geometric ray tracing. The thickness of the sapphire cork is based on the fact that the light should just travel through it and not through the surrounded capillary, hence heating up the glue or/and the capillary and therefore lead to thermal damage.

It was not possible to stabilise the tip enough so that it could hold the strain during the polishing and therefore the silica glass capillary broke. To increase the stability and support an UV glue coating (NOA-61 from Norland) was used, but this also had no effect on the breakage of the tip. The weak point is the silica capillary; it is too thin after the collapsing to provide enough mechanical strength with an OD 350 µm and ID 180 µm before shrinking and OD ~280 - 300 µm ID ~160 µm after. Due to the mechanical strength and hardness (sapphire: 9; silica: 5.3-6.5 on the Moh's scale) of the sapphire fibre it is both hard to polish and will move slightly during this procedure. This movement will put stresses on the glass causing it to break. Therefore the tip was breaking during the polishing and no working tip could be produced.

6.2.1.2 Bonding of sapphire in silica

To bond the sapphire fibre into the silica capillary (ID 180 µm) the capillary was filled with glass-solder (OZ Optics LTD. GSP-C-279-762-254). This solder is supplied as a ring shape which could fit around the sapphire fibre, the composition of the solder is confidential. The glass transition temperature is given from the supplier as 215°C. The ring was placed under the electric arc of the fusion splicer where the glass capillary and the sapphire fibre meet, see Figure 96.

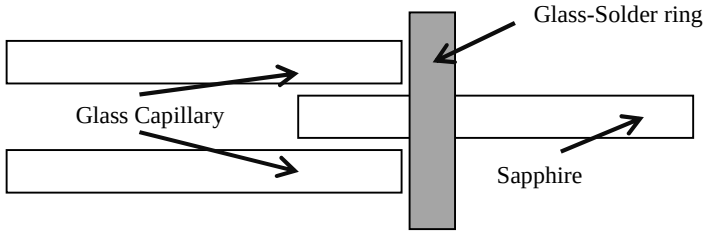

Figure 96: Schematic using a glass-solder ring to fix a sapphire fibre inside a silica glass capillary. The glass solder ring is placed at the interface, and heated up using a fusion arc splicer.

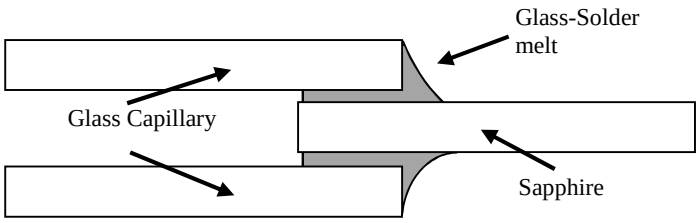

Figure 97: Combining of a silica class capillary and sapphire fibre using a glass-solder ring (composition is confidential). The glass solder ring was heated and penetrates into the gap between the sapphire fibre and the silica glass capillary, thus hermetically sealing the interface.

By using the fusion splicer mentioned before the glass-solder becomes molten and due to capillary action is drawn into and seals the space between the two components (Figure 97). After cleaving the excess sapphire, the tip was again mounted and surrounded by wax for the polishing. However, during polishing the silica glass capillary failed as shown in Figure 98 left. The failure was thought to be due to stresses induced into the silica capillary due to a mismatch between the thermal properties of silica and sapphire and the relatively high hardness of the sapphire. To test this the sapphire fibre was replaced with a silica fibre. The fibre used was a standard telecommunication fibre (SM28) with a slightly smaller diameter of 125 µm. In Figure 98 right, the result is shown, and it is clear to see that there are no cracks in the surrounding glass tube. The deformation of the outer tube in the Figure 98 is due to the heating which is needed to melt the solder.

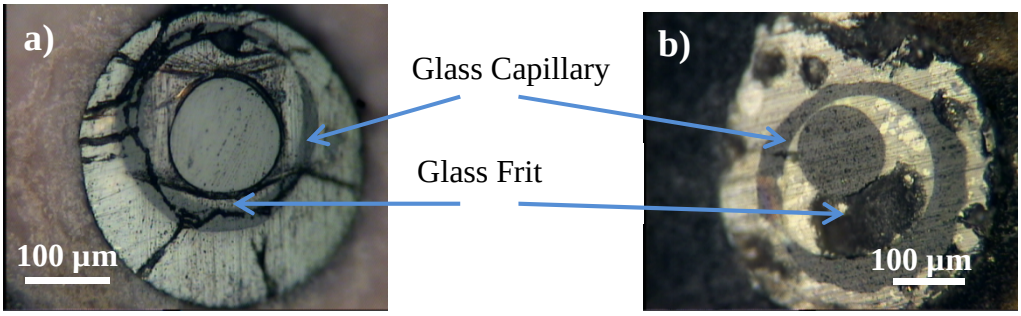

Figure 98: Sapphire core a) and silica glass core b) fixed in a glass capillary using a glass-solder. As clearly visible on the left side there are cracks in the surrounding capillary, whereas the on the right the capillary is still intact.

6.2.1.3 Bonding of sapphire in sapphire

To match the hardness and the thermal expansion coefficient a capillary made out of sapphire had to be used. To be sure that the sapphire for the window and capillary were of the same quality they were acquired from the same supplier (*Swiss Jewel Company Ltd.*). In this case the supplier did not have any fibre, therefore rods with a length of 10 mm were ordered. The rod had an outer diameter of 580 µm (tolerance of 10 µm) and

the tube an inner diameter of 610 µm (tolerance of 25 µm) and an outer diameter of 1.2 mm and a length of 1.4 mm (Figure 99). The larger inner diameter (compared to the silica capillary) also had the advantage that it could encapsulate larger fibres, as was later needed for the HC-NCF with an OD of 360 µm. As the end faces of the rod were not optical grade they had to be polished, using the same setup as described for the sapphire fibre in §6.2.1.2.

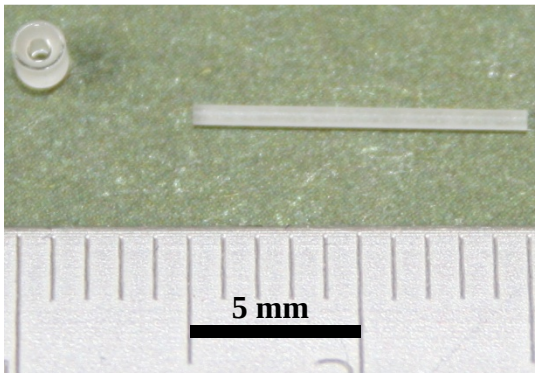

Figure 99: Sapphire rod and tube used for the "full sapphire tip".

The glass-solder rings used in the previous approach had an inner diameter of 150 µm and hence did not fit around the sapphire rods. Therefore the bonding of the two pieces was done using a glass frit paste (AGC F00392 5115HT1). As the temperature had to be precisely controlled to ensure a good bonding and the heating time was much longer than could be provided by a fusion arc splicer, an oven had to be used for the curing of the frit. The glass-frit-paste was coated around the rod and cured in 5 steps:

- Drying at 120 °C for 10 min
- Decarbonisation at 270 °C for 20 min
- Glaze at 440 °C for 20 min
- Sealing at 440 °C for 20 min
- Cooling with 10°C/min

After bonding into the sapphire tube the excess sapphire rod was cleaved back with a ceramic blade and the whole tip was mounted and polished back until a good optical quality was achieved as shown in Figure 100. There is an area of discoloration on the right side where the tip was not polished due to the tip being angled slightly relative to the polishing sheet (Figure 101). It shows the original state of the tube. One disadvantage of using a fibre polishing machine is that the material removal rate is relatively small. Polishing back to a flat endface took more than 24 hours and the sequential polishing to

achieve a good optical quality took about 1 hour per polishing sheet. Also it is not possible to polish more than one tip at a time, and the alignment was difficult. As seen in Figure 101 the polished end surface was not perpendicular as the holder was not optimised for the tips being too large hence allowing the tip to tilt (Figure 102). Therefore a hole was drilled into the mount which was perpendicular to the polishing sheets with a diameter of 1.3 mm which was 0.1 mm larger than the OD of the tip (Figure 103).

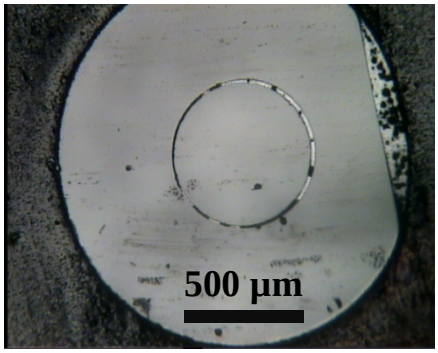

Figure 100: Polished "full sapphire" tip. The discoloration on the right side was due to an angle during the polishing and shows the original state of the tip before polishing.

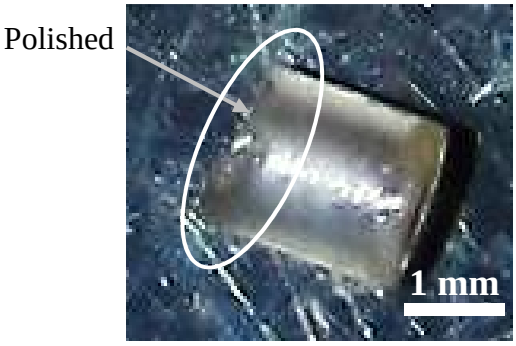

Figure 101: Side view of the first polished tips with an angled polishing face.

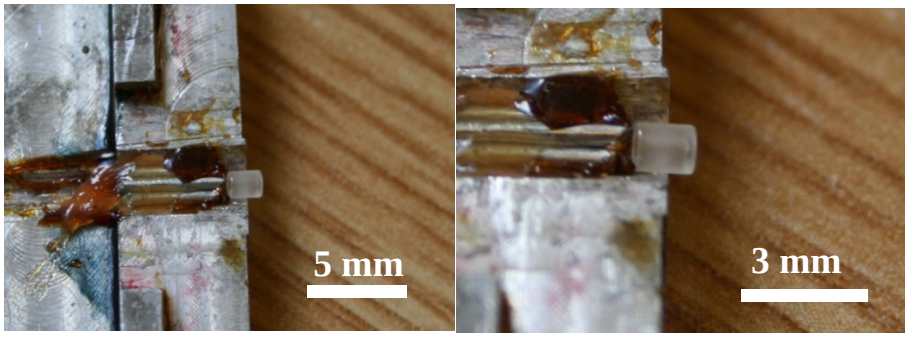

Figure 102: Original holder mount. It is not optimised for that size of tip and therefore leading to a difficult alignment and non-perpendicular polishing result.

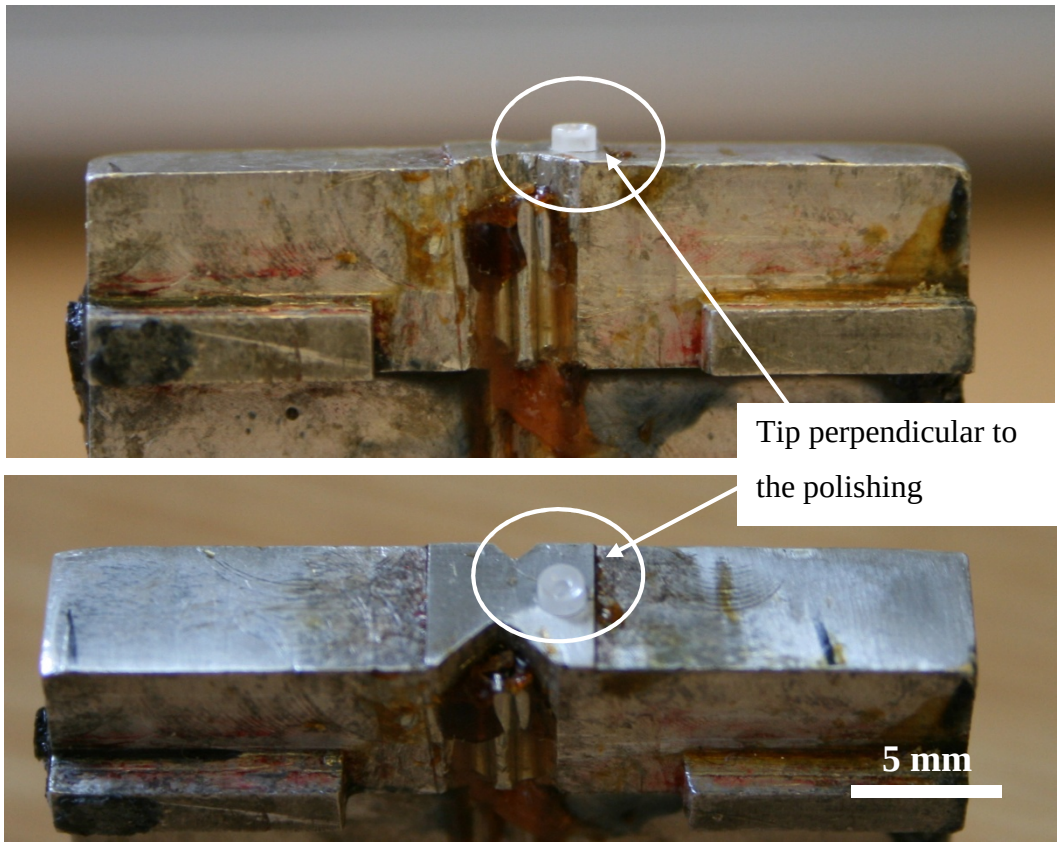

Figure 103: Modified mount for the sapphire tips, to guarantee a perpendicular polishing. The previous mount led to a tilt of the sapphire endtip in relation to the polishing plate, therefore the polished surface turned out to be tiled as well. This new mount consisted of a hole with a bore diameter slightly bigger than the OD of the sapphire endtip, so that the endtip is always perpendicular to the polishing sheet.

As mentioned above (§6.2.1) an issue with using the fibre polishing machine and the mount is that the polishing is time consuming. As an alternative a Struers LaboPol-5 polishing machine was used which although was not designed for fibres removal rates could be much higher due to the larger grinding discs used. Also the rotation speed of the disc can be regulated and if desired the holder where the tips are fixed can be rotated as well increasing the removal rate further. Diamond polishing slurry with different particle sizes (6, 3, 1 and 0.25 µm) from MetPrep was used in order of decreasing size.

For this machine a custom tip holder had to be constructed. It was made out of nylon 66 which was easily machined. In Figure 104 a schematic and picture of the mount can be seen. The screws on the back side of the mount could individually select the length of the tip to be ground back. This gave better control of the window thickness. With this method the polishing time of the tips could be significantly reduced and 5 tips per working day could be fabricated. Also it is potential method that could allow mass production of the tips.

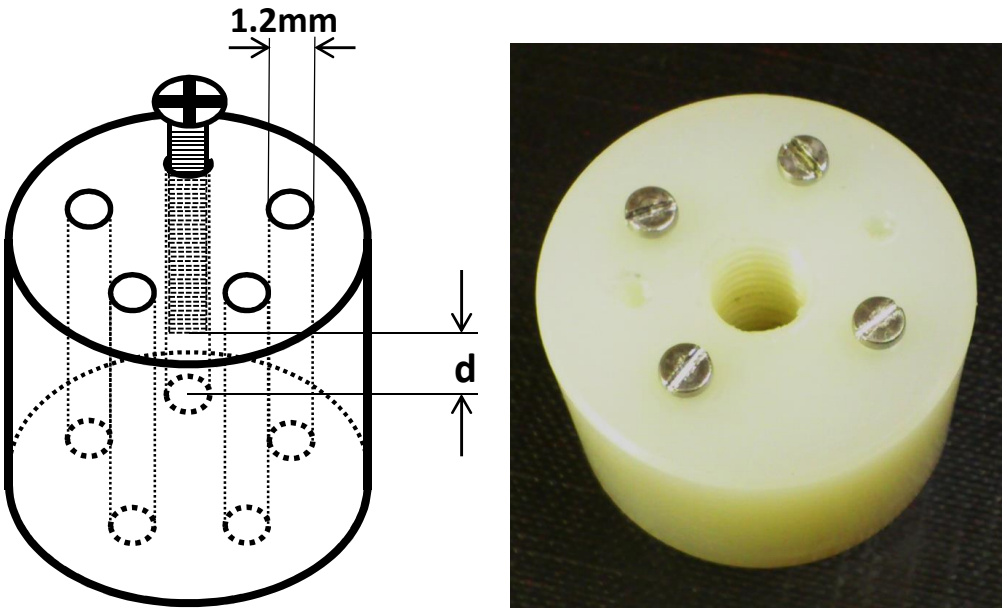

Figure 104: Nylon 66 endtip mount. The mount had 5 holes with a diameter which was slightly bigger than the endtip OD (1.4 mm). The endtips were placed into the holes and the distance d varied to achieve a desired thickness of the sapphire window. The mound was placed into a polishing machine, so 5 tips could be fabricated at one time with variable thicknesses.

6.2.1.4 High temperature sapphire tip

The temperature during tissue ablation can reach up to 800 ˚C [57]; the AGC-frit however has to be cured at a maximum temperature of 440 ˚C and would not withstand such high temperatures. To test this, a tip using the AGC-frit was heated up to 1000 ˚C for 10 min, and as shown in Figure 105 the frit cracked at this temperature resulting in cracks at the interface between the sapphire rod and tube.

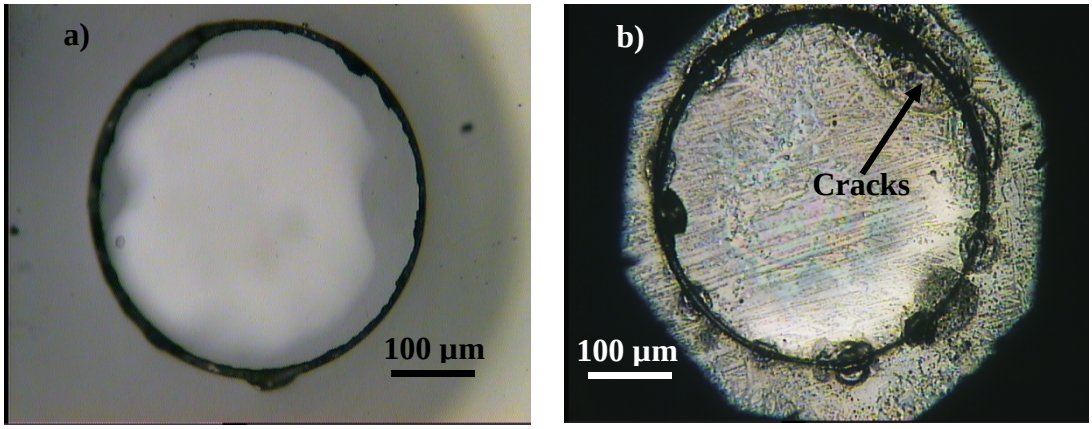

Figure 105: AGC frit, which is used to fix the sapphire window inside the sapphire tube before a) and after b) heating up to 1000°C. Cracks are clearly visible.

The alternative is a high temperature glass-frit; in this case a mixture of glass frit powder (LK8800) from Zibo Fuxing Ceramic Pigment & Glaze C. Ltd. and water to form glass-

frit paste. This frit is normally used to glaze tiles and is non-toxic (mainly SiO_2, CaO and additives), also it can withstand temperatures >1100˚C. The curing of the frit is done at 1080˚C for 30 min and tests were carried out to see if there was any cracking of the frit at high temperatures. The finished tip shown in Figure 106a was reheated up to a temperature of 1100˚C for 2h. The contamination in Figure 106a (i.e. before reheating) was ethanol residue which was used to clean the facet It is clear that there were no cracks in the glass frit or the tip after the reheating (Figure 106 b) and it is mechanically sound, confirmed by performing a shear strength test (discussed in §6.3.1.1).

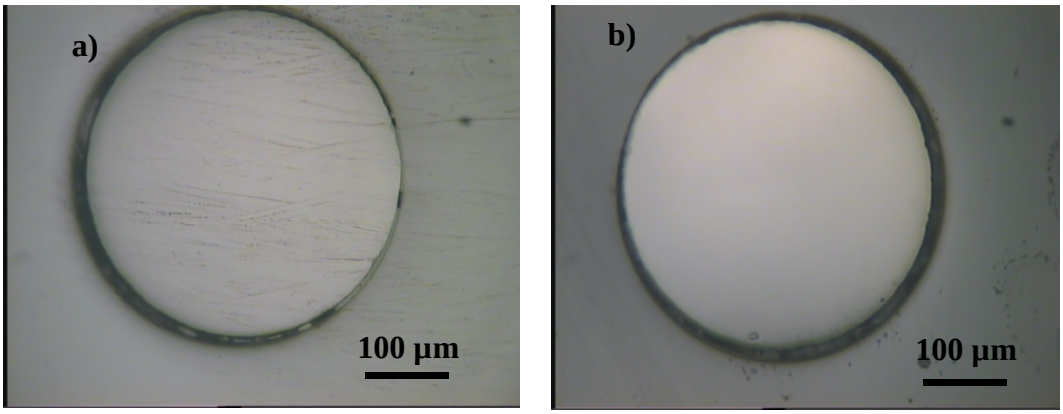

Figure 106: High temperature durability of the endtip and frit was tested by fixing the sapphire window inside the sapphire tube, and reheating it to a temperature of 1100°C a) End surface of the tip before reheating (stripes are residue from ethanol) and b) Endtip after reheating, no damage is visible.

A general problem of the endtips during and after the fabrication was the cleaning. If some of the glass-frit stuck to the inside of the window and was cured it was not possible to remove these contaminations. A sample of such a contamination is shown in Figure 114b). To avoid this care had during the fabrication process has to be taken. However, loose contamination could be removed by placing the tip into an ultrasonic bath filled with ethanol or acetone.

6.3 Tip properties

The “full sapphire high temperature” (6.2.1.4) tip was the only reliable and repeatable production method. All further tests were done using this tip design and material.

6.3.1.1 Mechanical stability

One of the requirements if the endtip is to be used in medical applications is that it has to be mechanically stable, so that no part can become loose or break away contaminating the tissue. The main force which the tip has to withstand is the pressure rise due to the micro-expansion of water under laser radiation and it has been shown that this shockwave

pressure reaches up to 12 MN/m^2 [157]. To ensure that the tip can cope with those forces a "push-test" has been undertaken to measure the force needed to push the window out of the tube. A schematic of the test is shown in Figure 107. A counter bore hole into a baseplate. The larger hole dimension of the counter bore had an ID the same as the OD of the tip. The smaller hole had an ID larger than the ID tube but smaller than the OD hence providing a platform on which the tip could sit. A sapphire rod was used to apply a force onto the endtip window.

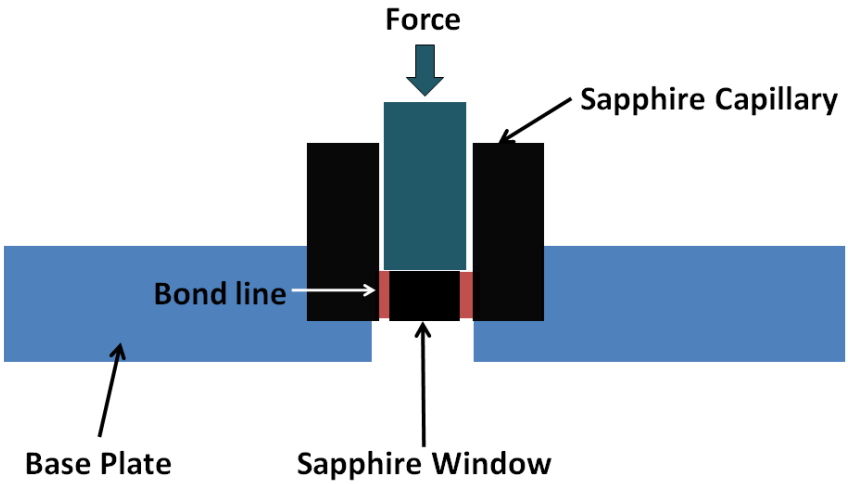

Figure 107: Schematic setup (not to scale) for the mechanical stability testing of the sapphire endtip. The finished sapphire endtip is placed into a base plate with hole the size of the OD of the endtip. A counter bore is drilled which has a diameter bigger than the sapphire window but smaller than the OD of the endtip. A sapphire rod is used to apply a force onto the sapphire window to measure the force needed to push the window out of the endtip.

The sheer stress τ is defined as

$$\tau = F/A \qquad (7)$$

where F is the applied force and A is the area over which it is applied, in this case the bonding area from the glass frit on the cylindrical side of the sapphire window. The maximal force that could be applied was 6.867N, corresponding of 0.7 kg resting on the top of the rod. At greater forces/weight the sapphire rod which was used to transfer the force onto the window failed. The area of the bond was calculated as $7.03 * 10^{-7}$ m (diameter 580 µm and window thickness 400 µm) hence the maximal shear stress that could be applied over the bond without the transferring rod breaking was 9.77 MN/m^2. A shockwave pressure of 12 MN/m^2 acting on the endtip window would produce a force of 12.68N which in turn results in a shear force on the bond area of 18 MN/m^2. Unfortunately, it was not possible to find a suitable material that could be used as a rod

to apply such a force. However, independent from this data it could be shown that the tip withstands these forces without any damage, as will be described in more detail in §7

6.3.1.2 Leak testing

Another important property the endtip needs is that it has to be hermetically sealed so that no fluids (e.g. water and blood) can propagate through it contaminating the hollow core fibre inside. To determine the hermeticity, the endtip was again mounted in the baseplate described in the earlier paragraph (§6.3.1.1), and positive pressures applied using helium on one side of the plate. For an initial test, the opposite side was sprayed with soap water around the exit, any leaks would be indicated with bubbles. To prevent any gas leaking between the endtip and the baseplate it was sealed using cement wax. Beforehand the cement wax was tested in the same manner when it sealed a hole in the baseplate to ensure that it is leak free. No bubbles were observed during this test indicating a level of hermeticity.

A more sensitive experiment was conducted, where the actual leaking rate was measured. The setup was identical to the initial test but in this case a mass spectrometer was connected via an O-ring seal (Figure 108).

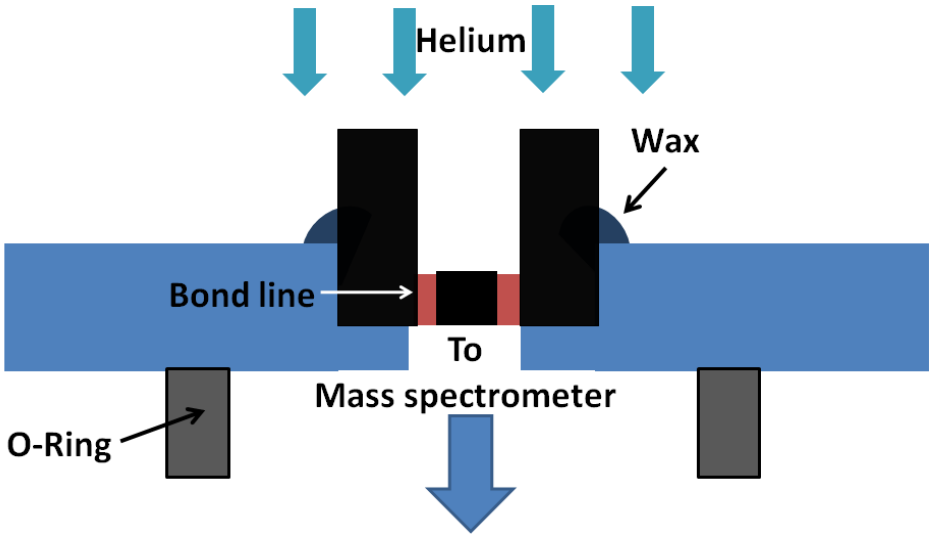

Figure 108: Schematic setup (not to scale) for the hemericity testing of the sapphire endtip. The finished sapphire endtip is placed into a base plate with hole the size of the OD of the endtip. A counter bore is drilled which has a diameter bigger than the sapphire window but smaller than the OD of the endtip. The gap between the sapphire endtip and the base plate is sealed using cement wax. One side of the baseplate is connected to a mass spectrometer helium is applied on the other side. Any leaks would be detected as a characteristic helium peak on the mass spectrometer.

Using this setup a leaking rate of $<10^{-7}$ mbar∗l/sec was measured with a Laybold UL 200 spectrometer. In context this means that helium could not propagate through the glass-

frit, and therefore it will provide a seal to any fluid it is likely to encounter, this was also proven by the use of the endtip under water as will be described in §7

6.3.2 Optical properties

The optical properties of the tip, or more precisely the window, are crucial. As the output of the fibres is single mode like it would be desirable to preserve this and not degrade it when it propagates through the window. Hence, the geometry and surface quality of the window is important.

The tests performed compared the bare fibre output with an encapsulated version to investigate the degradation of the beam output profile. These tests were also done at two different wavelengths to verify the broad use of the sapphire endtip. The original tests were undertaken using 1064 nm wavelength in conjunction with a HC-PCF. The advantage of using this wavelength is that it was easier to image and hence compare the results. A direct reimaging system was setup as described in §2.1.3 and the output of the bare fibre and the encapsulated version captured. The distance between the end of the fibre and the inner surface of the endtip window was around 100 µm. In Figure 109 the two beam profiles and the cross-section through the beam along the white line are presented. As can be seen the degradation of the beam profile is minimal and both profiles were single mode.

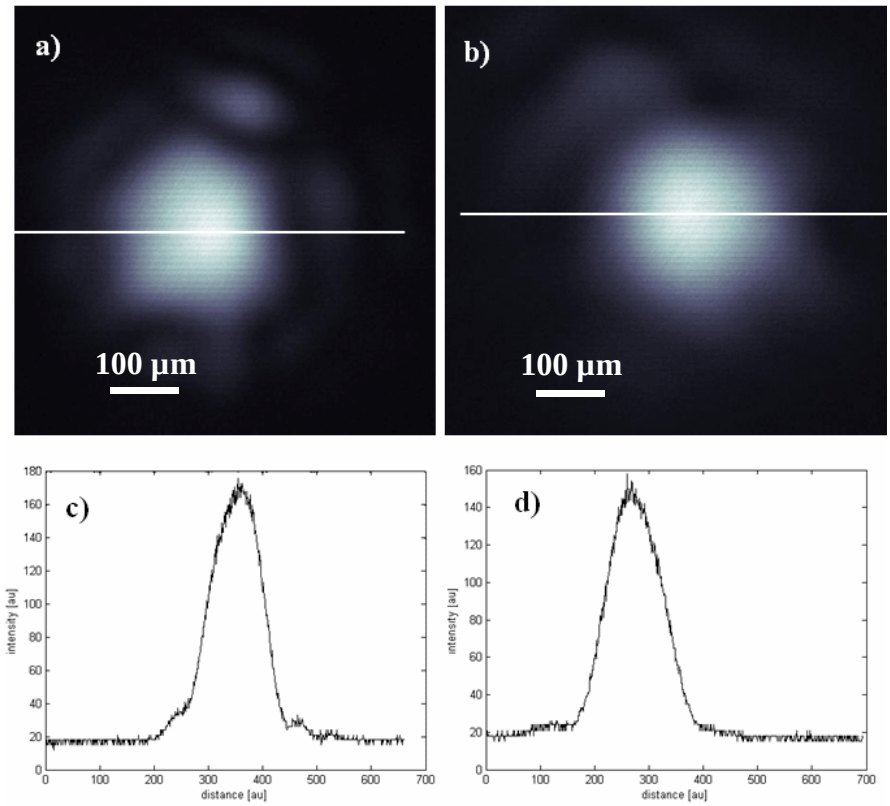

Figure 109: Output beam profile for 1064 nm wavelength with corresponding cross section along the white line. a) Bare HC-PCF output profile; b) Output of the endtip mounted onto the HC-PCF; c) Cross-section of the beam profile presented in a) and d) Cross-section of the beam profile presented in b).

The second set of experiments was carried out using the high power IMPEX laser system. A "secondary fibre movement measurement" (as described in §4.4) was done at the output surface of the endtip, which represents the beam profile on tissue if the system is used in "contact mode". In Figure 110 the original output of the bare fibre (red) and the encapsulated output (black) are shown. Both graphs are normalised to aid comparison. There was a slight degradation of the beam profile. A widening of the beam profile is expected due to the divergence of the beam. Calculating the distance between the outer surface of the endtip and the end of the fibre (using the divergence of the beam) gave a result of about 300 µm. This is in a good agreement with the values measured for the window thickness.

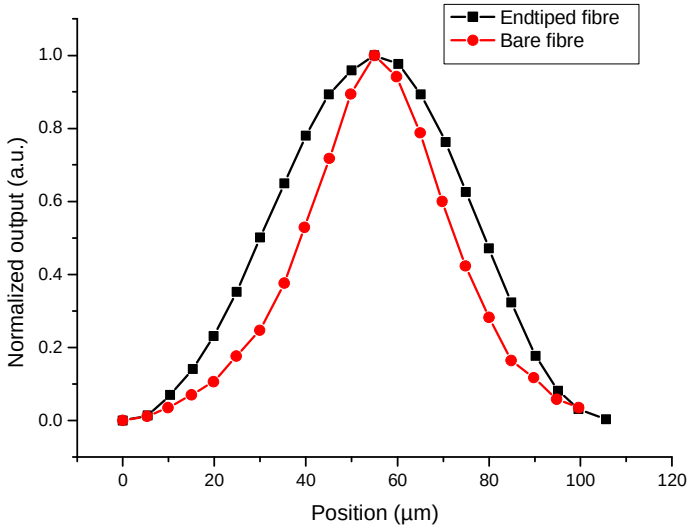

Figure 110: Beam profile at the HC-NCF output face (red) and at the endtip' s outer surface (black), using the IMPEX laser at 2.94 µm.

The beam profile was also measured at distances of 10, 20, 50 and 100 mm from the output end. These values were chosen as they represent actual working distances as would be used by a surgeon or dentist. The difference between the bare fibre (Figure 111) and the end capped version (Figure 112) is shown below. The images were taken as a reflection from a ceramic surface as is described in §2.1.3

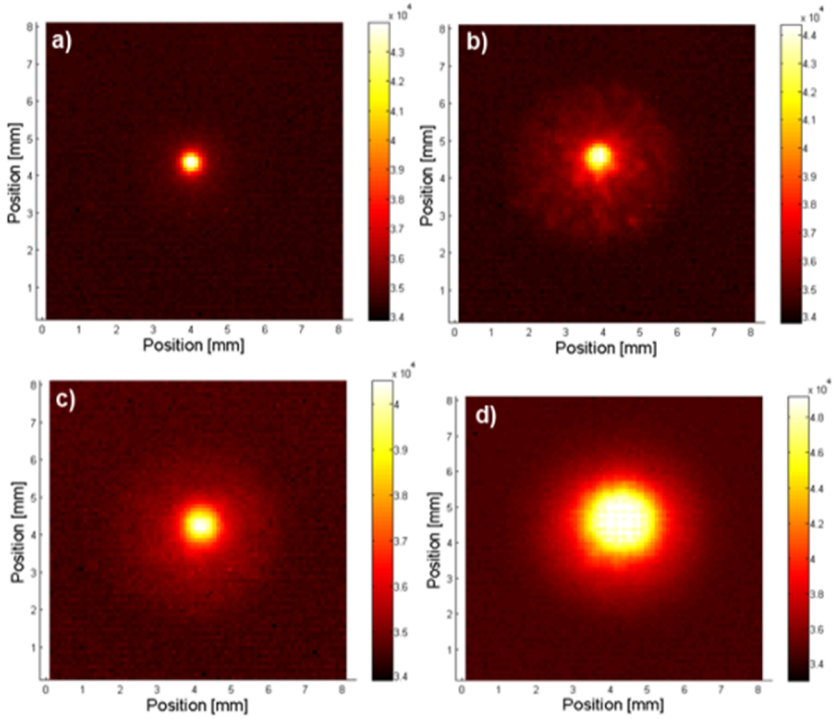

Figure 111: Far-field beam profile for the bare HC-NCF fibre output for different distances from the fibre end, using the IMPEX laser at 2.94 µm. Fibre length is 6.48m. From top left to bottom right: 10, 20, 50 and 100 mm.

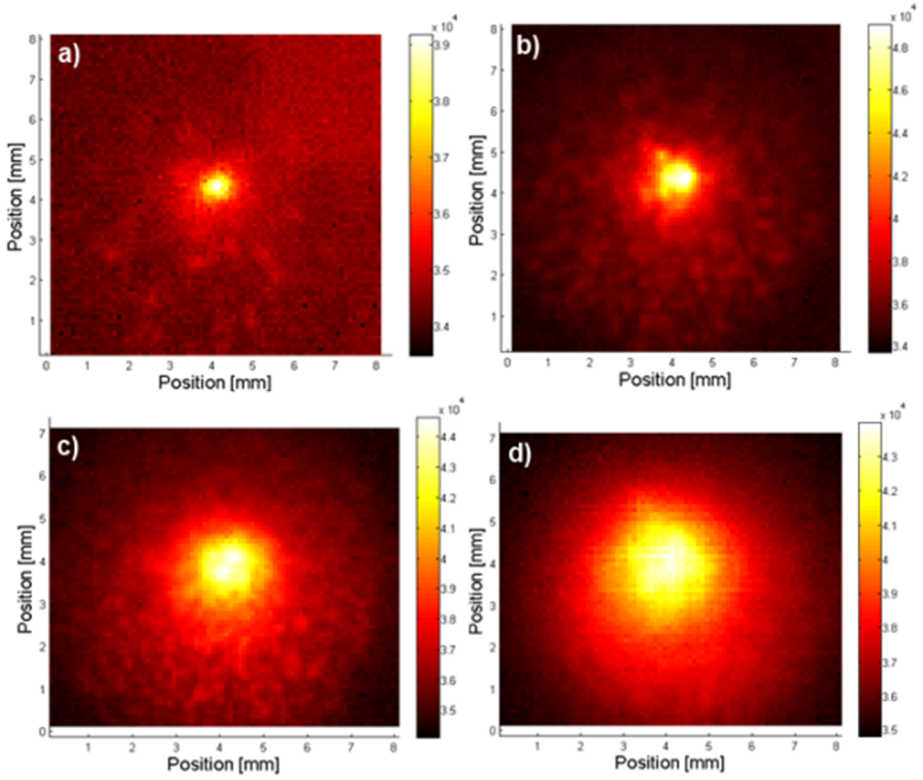

Figure 112: Far-field profile of the encapsulated fibre. Distance from the endtip to the reflective surface, from top left to bottom right: 10, 20, 50 and 100 mm.

There was some degradation of the beam profile but their single mode like profile was preserved. The beam profile after the endtip had some slight artefacts and more speckles around the central peak which was most likely due to debris on the inside of the tip.

The losses due to the endtip were measured as 23% which is higher than the expected value of around 14% which would arise due to the Fresnel reflections at both interfaces (6.5% each) and the small absorption losses in the material. It is expected that for these samples the polishing quality was relatively poor indicating that quality control of the polishing process is important. To verify this, the losses for a sapphire window (from the same company) were measured and gave a value of 13.6% which is in very good agreement with the calculated losses due to the Fresnel reflection.

6.3.3 Damage threshold

The final test performed with the endtips was to measure their laser damage threshold, as this dictates the maximum allowed power output.

To get the maximal LIDT of sapphire, a sapphire window was placed at the focal point of the beam and the laser power gradually increased till a defect/ablation could be seen. The windows were supplied by the same company as for the endtip components (*Swiss Jewel Company Ltd.*). For the final focusing lens a focal length of 26 mm was

used and the incident laser beam diameter was 8.5 mm, which lead to a focal spot size diameter of 28.8 µm. The sapphire window was observed from the back side using a USB–microscope.

The sapphire window used was polished to an optical grade. This leads to a low absorption and therefore it was not possible to establish a LIDT for the window. The maximal pulse energy on the window was 300 mJ which leads to an energy density of 46 kJ/cm^2. To get a better comparison with the endtips the sapphire window was polished with the same equipment and to the same degree as the tips which gave a slightly rougher and scratched surface. In this case it was possible to ablate and catastrophically damage the sapphire window. The LIDT in this case was 33 kJ/cm^2.

To compare this with the sapphire endtip, a 2 m long HC-NCF was inserted into it and fixed using a heat shrinking tube (Figure 113). The endtip used was not one with the best polishing of the inner surface (Figure 114b) and had contaminations on the inside surface to represent a worst case scenario. The laser light was launched into the HC-NCF and the laser power sequentially increased. The output of the fibre was calibrated beforehand by measuring the applied flash lamp voltage onto the laser and the output, so that the incident power onto the inner surface of the endtip was known. The breakdown of the endtip window occurred at a pulse energy of 20 mJ using the mode field diameter of the fibre as 89 µm gives a LIDT of 715 J/cm^2. The two surfaces of the endtip before and after the damage test are shown in Figure 114.

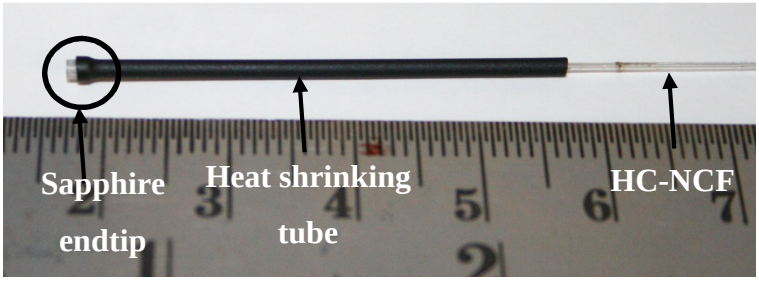

Figure 113: The sapphire endtip is mounted onto the HC-NCF fibre using a heat shrinking tube.

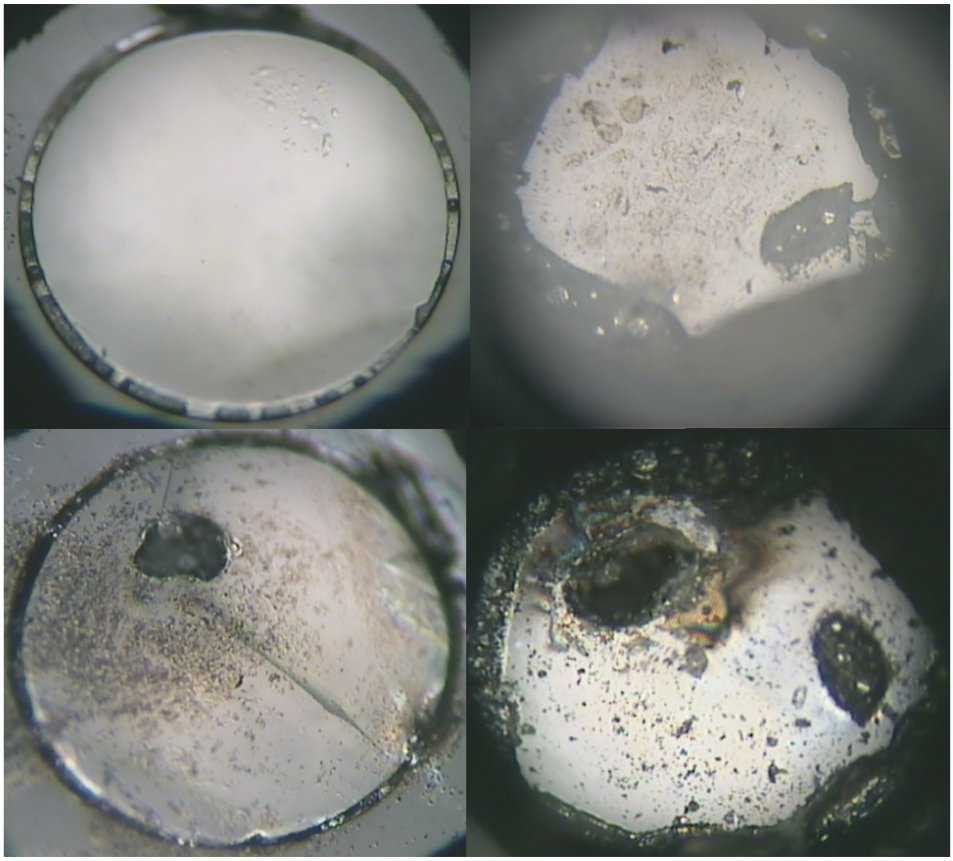

Figure 114: damage of tip (2) top left to bottom right: undamaged tip outer and inner surface damaged tip outer and inner surface. The tip is not cleaned at this stage, conditions are in dry atmosphere.

6.4 Conclusions

The encapsulation of hollow core fibres is mandatory if the fibre is to be used in a wet environment like minimally invasive surgery, this is to protect the fibre core from debris, fluids like blood and water and other contamination. If these contaminations penetrate the fibre core they would absorb the laser radiation and heat up, leading to a catastrophic damage to the fibre. The solution proposed here was the use of an endtip fabricated from sapphire. Sapphire was chosen as it has a wide transmission window, and is a very tough material and can withstand high temperatures. The steps to the final version of the sapphire endtip and its fabrication were described in this Chapter. The sapphire endtip was mechanically and optically tested, with the result that it can withstand high mechanical forces and is hermetically sealed, which is important if the fibre-endtip is to be used under water. Also it could be shown that the beam profile was not disturbed if the fibre is sealed with the endtip, which is particularly important if a single mode fibre (like the fibres described in this work). One big advantage of this encapsulation system is that it can be used over a wide range of wavelengths and with a variety of fibre

diameters and designs. Further work on the endtip is the possibility of shaping the window to achieve a manipulation of the beam exiting the fibre. This could be used to collimate the beam or to focus the beam and have a certain working distance from the end of the endtip.

7 Practical demonstration of tissue ablation using a silica HC-NCF

This final results Chapter will show a demonstration of practical tissue ablation using the HC-NCF described earlier. Due to the damage limitations of the HC-PCF sufficient energy to manipulate biological tissue could not be delivered and hence no practical demonstration could be carried out with this fibre (for more details see §3.1). The tissue samples used for these experiments were lamb in origin and different tissue types were used; muscle tissue, fat tissue and bone with most of the experiments performed on bone (Figure 115). The bone used was, as seen on in the image for the first experiment (initial ablation test, as described in the next paragraph) was preserved and sterilised by boiling for ~1 h, for the following investigation. For convenience of discussion the ablation threshold for different tissue types using similar laser parameters as the IMPEX laser system (§2.2.2), are reproduced from Table 5 in Table 9.

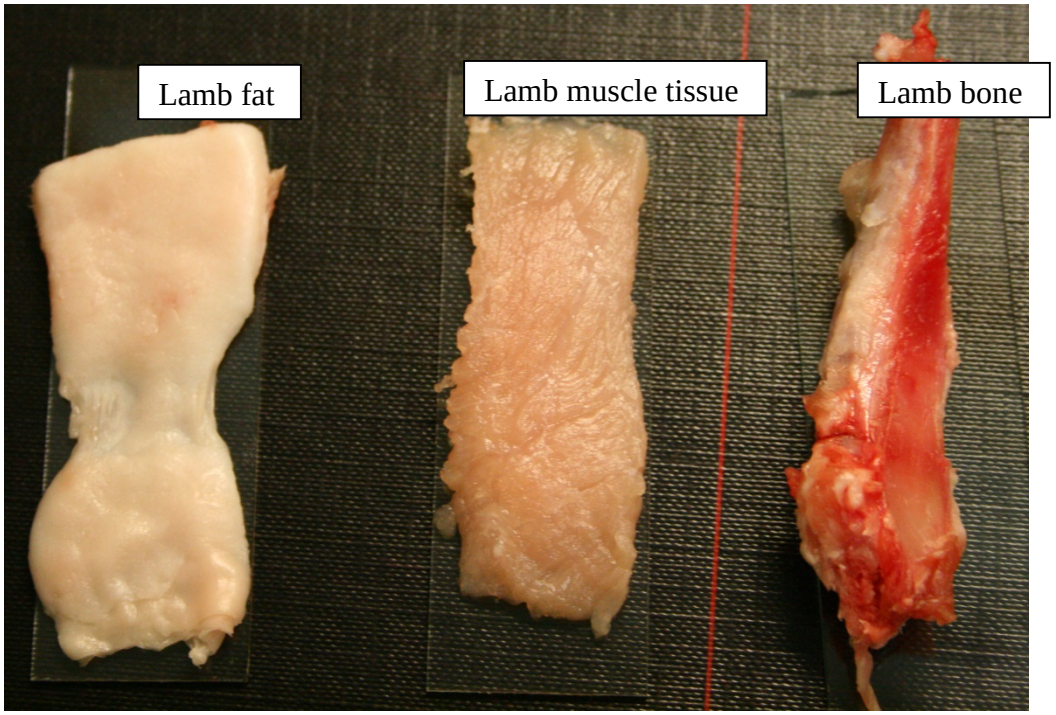

Figure 115: Lamb tissue used for the experiments. The lamb bone was sterilised and preserved after the first experiment by heating for ~1 hr in water at 100°C.

Table 9: Ablation thresholds for different tissue types for a wavelength of 2.94 µm. (na -- not available).

Rep. rate /Hz	Pulse duration/µs	Tissue type	Threshold /Jcm^{-2}	Reference
2	250	Human dental enamel	35	[44]
7-10	250	Human skin	1.6	[45]
1.7	250	Pig retina	1	[46]
1	100-5000	Human dentine	2.69-3.66	[47, 48]
5	na	Pig skin (vitro)	3.6 - 5.6	[49]
2	200	Guinea pig skin	0.6-1.5	[50]

The HC-NCF used for the trials was originally 2 m in length and was sequentially cut back by cleaving both ends of the fibre after each experiment to about 1.2 m. This was to ensure that there was no residual debris contaminated the fibre core as it was used in some tests without the endtip described in §6.2.1.4. This was particularly important for the drilling of muscle tissue described below.

The first set of tests was carried out with a hand held bare fibre, with a standoff between ~1 – 10 mm to simulate a surgeon's movement. The fibre output energy was set to 30 mJ leading to a fluence of > 430 J/cm^2 at the end of the fibre (the half divergence angle of the fibre was 1.7°). As expected with such a high fluence all three tissues could be ablated, screenshots from the ablation are presented in Figure 116. No images are included for the ablation of fat tissue as the image quality was not sufficient to be able to clearly see ablation. This was merely used as a quick demonstrator and not quantitative analysis of the hole depth and diameter was carried out.

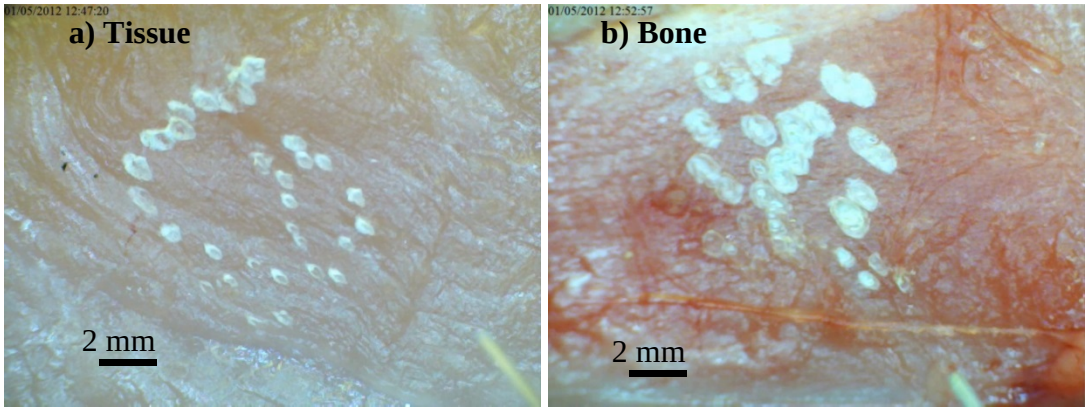

Figure 116: Ablation of biological tissue. The pulse energy was 30 mJ (430 J/cm^2), and the fibre was hand held. a) Lamb muscle tissue. b) Lamb bone.

Another test performed was again using the bare fibre (hand held) as a “drill” to penetrate the lamb muscle tissue, by pressing the fibre inside the tissue using minimal force such that it was possible to ablate a “tunnel” in front of itself. See Figure 117 for details. To verify that the fibre drilled its way through the tissue instead of being inserted due to its small size, the test was repeated with the laser turned off. The fibre was much harder to press into the tissue (not quantified) and also the tunnel collapsed after the fibre was removed from the tissue, whereas with the laser on a distinctive hole was visible. After dragging the fibre out of the tissue it was still possible to ablate further the material (Figure 117c), demonstrating that there was no catastrophic damage to the fibre. The output end of the fibre after this experiment is shown in Figure 118, and as can be seen part of the core surrounding structure was destroyed but some regions were still intact. This test was not aimed at demonstrating applicability for a specific medical procedure; the fibre in reality would not be used in this way. However, it does serve as a convincing demonstration of the relative robustness of the fibre and its potential to continue operating (in terms of delivery of pulses with appreciable energy) even if significant damage to the output end face has occurred.

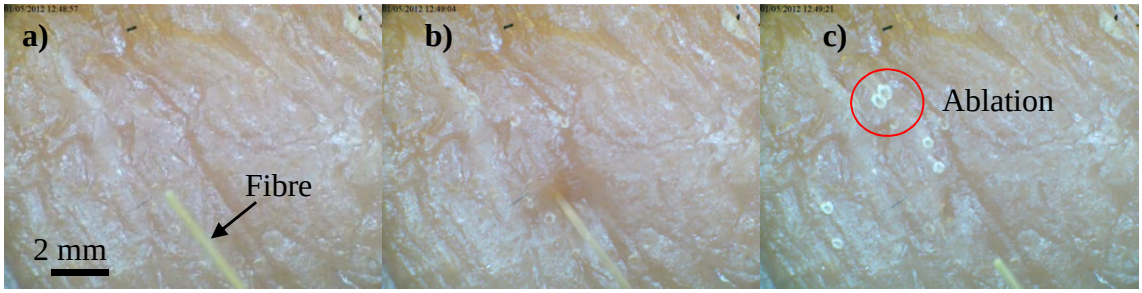

Figure 117: Bare HC-NCF fibre "drilling" of lamb tissue. a) Fibre and tissue before drilling. b) During drilling. c) After drilling. Sufficient energy for tissue ablation can still be delivered through the fibre after his process. The IMPEX laser with a wavelength of 2.94 µm was used.

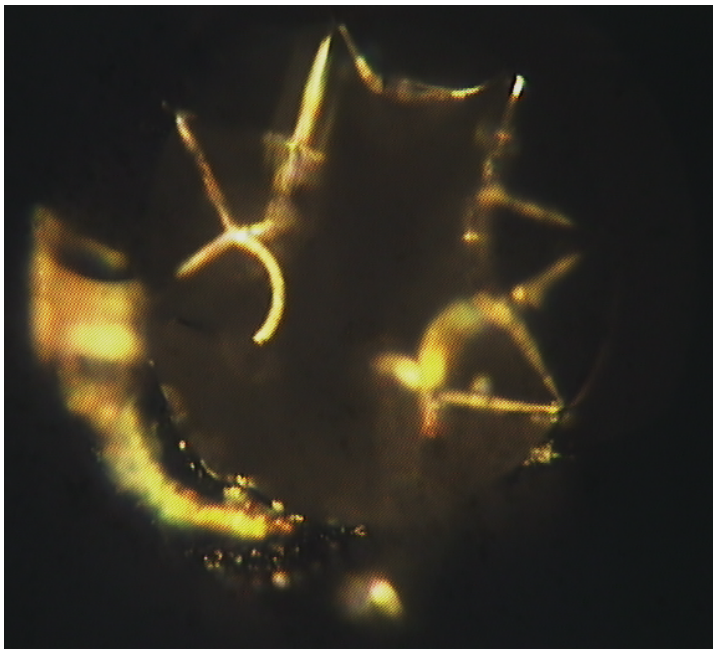

Figure 118: HC-NCF after used as a "drill". The surrounding structure remains partially intact. In this damaged condition the fibre could still be used to ablate lamb tissue.

For a more realistic demonstration of how it is envisaged the fibre would be used in actual surgical procedures the fibre was used in conjunction with the endtip. This was to demonstrate that the system is capable of ablating biological tissue in different environments and to prevent damage to the fibre as seen in Figure 118. In this case the fibre was fixed and the distance between the output of the endtip and the tissue was varied between ~5 mm to in-contact, with the same energy output after passing the endtip as in the previous experiment (30 mJ). Due to the divergence (NA=0.03 half angle of divergence of 1.7°) of the beam this lead to fluencies from ~30 J/cm^2 to ~300 J/cm^2 at 5 mm distance and in-contact, respectively. This test was performed in air and also in a fully water submerged environment with both single pulse and 15 Hz operation. However in the submerged environment only direct contact of the endtip with the tissue resulted in ablation, as is expected, due to the high absorption of water at this wavelength (87% of the energy is absorbed in 300 nm of water). Images showing both cases are presented in Figure 119. In these experiments no damage occurred to the endtip and the cuts as seen in Figure 119a are ~300 µm in width and about 250 µm in depth.

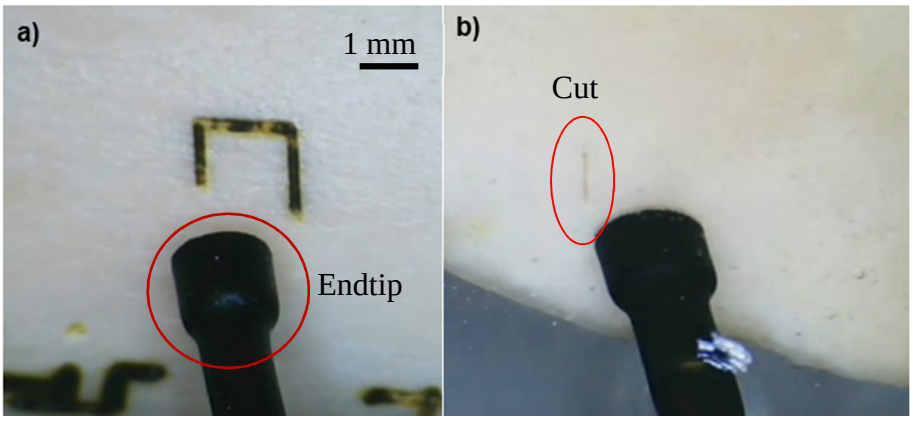

Figure 119: Tissue ablation using the HC-NCF with a sapphire endtip. a) In air with ~ 5 mm between endtip and tissue. b) Submerged in water and in-contact. The IMPEX laser with a wavelength of 2.94 µm was used.

Using the same parameters as in the previous experiment the ablation depth for a single shot on bone was approximately 200 µm and the heat-affected zone (HAZ) was about 70 µm deep (see Figure 120b) in air if the endtip was in contact with the bone. HAZ in this work is defined as discolouration/carbonization of the tissue. The HAZ was not present if the tissue was ablated submerged in water (Figure 120c), the dimensions of the ablated spot are the same as the air case. The missing HAZ/carbonisation when ablation is carried out under water is not surprising as the water has a cooling effect; it has also been shown that the main effect of ablation under water is due to micro-explosion of the superheated water [55]. In this case the laser radiation is absorbed by the water between tissue and endtip, which will evaporate instantly, leading to a micro explosion and implosion which increase the ablation rate (a more detailed explanation is given in the introduction, see §1.1.1.

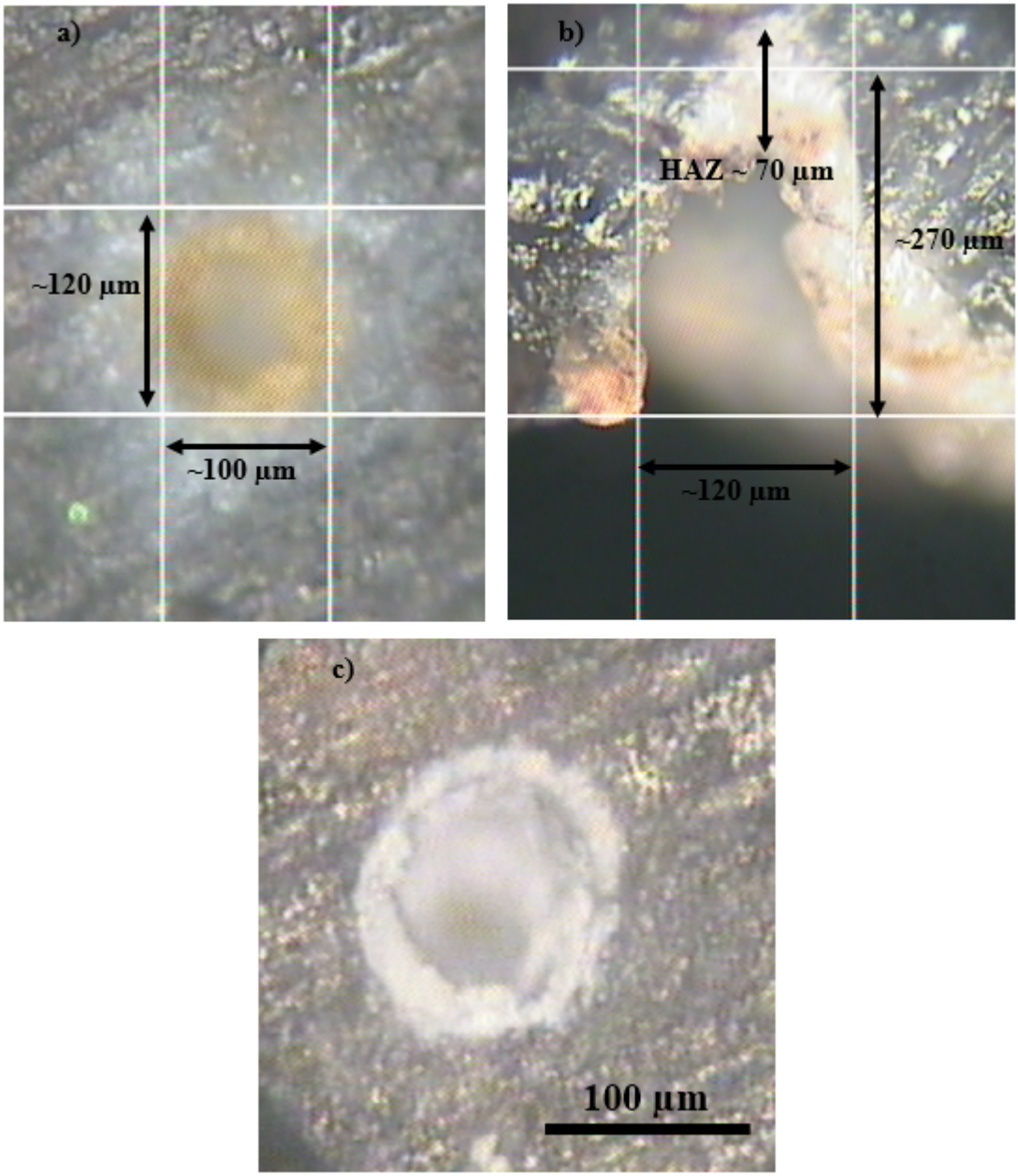

Figure 120: Single shot ablation of lamb bone: a) Top view with HAZ visible (brown/orange discolouration) in air; b) Cross-section shows an ablation depth of ~200 µm and a HAZ of ~70 µm and c) Ablation under water, same ablation spot size but no HAZ present.

For medical applications it is often important to minimise the HAZ and discolouration/carbonisation, as seen in Figure 119a and Figure 120a, to minimise collateral damage therefore a series of experiments were performed to find a parameter region where ablation could be achieved without carbonisation of the tissue. A preserved and sterilized lamb bone was again used for these experiments, which were performed by Greig McAndrew a 4th year project student who was doing these experiments as his final year project under the Author's supervision. The distances between the bone and fibre were varied from 1 mm to 10 mm using a bare fibre of 1.2 m length, these distances were chosen as they most likely simulate the usual operation distance for a surgeon (private

communication with Prof. Baljean Dhillon BMed Sci, BM BS, FRCS and Prof. Hamish Simpson, head of "Edinburgh University Department of Orthopaedics and Trauma"). The HC-NCF fibre was fixed and the lamb bone was translated underneath it at a speed of 2 mm/s, a schematic of the setup is shown in Figure 121. The energy region 1.996 – 2.847 mJ (0.5 – 15 J/cm^2) was found to give the best results as at higher energies carbonisation occured and at lower energies no ablation could be detected. The relationship between the fibre-bone distance and the ablation depth is presented in Figure 122.

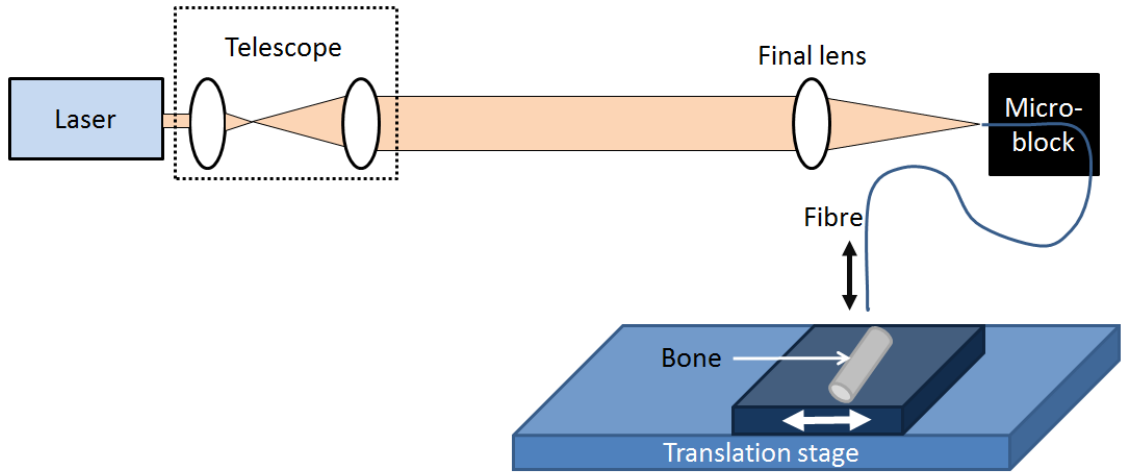

Figure 121: Schematic of the setup used for the investigation of the HC-NCF fibre to lamb bone distance versus the cut depth. The fibre was not end capped and the IMPEX laser with a wavelength of 2.94 µm was used.

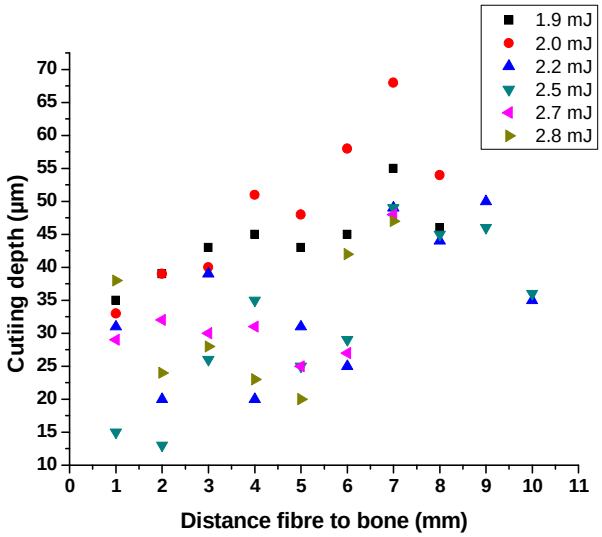

Figure 122: Relationship of the distance between the unprotected/bare HC-NCF fibre end and the lamb bone versus the cut depth. The translation speed of the bone was 2 mm/s. The fibre was not end capped and the IMPEX laser with a wavelength of 2.94 µm was used.

As can be seen from Figure 122, the ablation depth varied from ~ 15 µm to ~68 µm. No definitive trend can be seen in this graph although for all but one pulse energy value (2.2 mJ) the maximum cut depth was found when a standoff of 7 mm was used indicating and optimal position, which may be due to competing effects. It was observed that at shorter distances some carbonisation occurred which caused significant debris and material to fill the cut, therefore the measured resulting cut depth was reduced. However, as the fibre was set further away from the bone there would have been a reduction in the fluence on the tissue hence there would be a limit where no ablation occurred. By choosing a distance (7 mm) where no significant carbonisation occurs yet the energy fluence is such that tissue ablation occurs an optimal process can be achieved. One caveat to this description is that the peak standoff should be dependent on pulse energy delivered (as this will affect the fluence for a given standoff) however, in these initial experiments the optimal standoff of 7 mm was applicable for all pulse energies.

Clearly a more in depth investigation is necessary to understand the process fully and determine optimised parameters and this will be carried out in the future in collaboration with clinicians (see future work §8.2). The intention in these short experiments was to demonstrate the validity of this fibre for tissue ablation which clearly has been achieved. However using these data an initial estimation of the time for a realistic procedure can be estimated. Assuming an average cutting depth of 45 µm and a human femur with a diameter of 27 mm [158] leads to a cutting time of ~8100 seconds (2 h and 15 min) if the translation speed is 2 mm/s. This is a very simple estimation where the femur is considered uniform and solid and that the actual cutting depth would be the same as in the experiment presented. This is much longer than usual bone cutting (~3 min) using traditional methods (e.g. saw) [private communication with Prof. Hamish Simpson], however using a mechanical/ultrasonic saw has certain drawbacks compared to a laser, like limited cut geometry, fracture of fragile bones due to pressure, mechanical damage to the remaining bone and the and the potential damage and infection of surrounding tissue due to bone flour and fragments (for more details and references see §1.1.1). The overall cutting speed can be reduced if a faster translation speed is chosen, however this changes the pulse to pulse overlap to a point where there is significant distance between single shots. The maximal speed possible with the IMPEX Er:YAG laser system used here can be estimated using the maximal achieved single pulse ablation crater diameter of 305 µm. If a minimum overlap of 5% for the pulses is used the maximal speed achievable with a repetition rate of 15 Hz is ~4.4 mm/s. This provisional “speed limit”

can be overcome if a higher repetition rate laser could be used (e.g. 50 Hz using the "Pulser Derma" from doctor smile®). The easiest and most cost efficient way to increase the cutting time is to add water spray onto the ablation side, as is discussed in the introduction (see §1.1.1) the cutting depth can be increased by a factor of ~10 if a water layer is present. In this context it has to be pointed out that these experiments and the calculations following them are based on dry tissue without additional water spray.

Comparison of the presented results with the literature show a big discrepancy in the energy density needed for the carbonisation of the bone and the time needed/estimated. The energy density used by Stuebinger et al.[159] was 157 J/cm^2 with a repetition rate of 12 Hz delivered by the means of an articulated arm. Using these parameters in non-contact mode (standoff distance ~10 mm) there was no charring or any other negative surface alterations detected, as can be seen in Figure 123. The bones used for the study were 15.95±0.7 mm and 16.67±1.4 mm wide and 20.83±12 mm and 20±0.6 mm deep, respectively. It took 245.33±29.9 and 211.17±45.1 seconds to cut through the two bones, which is an acceptable time for surgical osteotomy [159]. This is a factor of ~38 faster than the estimated time for the cutting of a human femur using the presented results. There are several factors which explain this difference, 1) the femur was assumed to be a of cylindrical form, whereas in reality it is a tube, so that the cutting depth is different, 2) the laser used by Stuebinger et al. was a variable square pulsed (VSP) Er:YAG laser which was shown to increase the ablation volume compared to a free-running Er:YAG laser [160-162], 3) as mentioned earlier, the bone used presented here was dehydrated and no water spray was used, whereas in the other case study the operation was performed on a sedated and still living sheep under the addition of a water spray (40-50 ml/min).

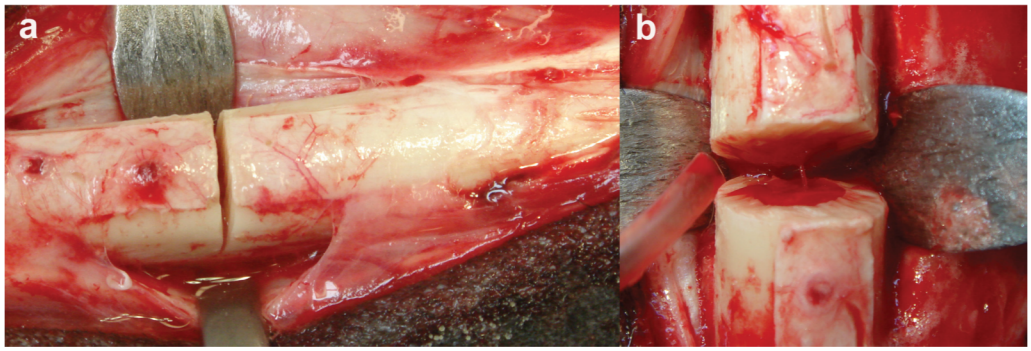

Figure 123: Precise and smooth osteotomy gap directly before final transaction of a sheep tibia. Er:YAG laser settings used for bone cutting were pulse energy of 1,000 mJ, pulse duration of 300 µs, and a frequency of 12 Hz (energy density, 157 J/cm^2). b) Clear bone surface of the osteotomy rim without any visible signs of carbonization or thermal damage. Further histological analysis revealed an undisturbed bone healing after 2 and 3 months that was even superior to conventional methods. Presented in [159].

7.1 Conclusions

HC-NCF has been demonstrated to deliver sufficient energies to be used to ablate hard and soft biological tissue; in this case lamb was used (fat, bone and muscle tissue). The feasibility of the fibre delivered system was investigated and demonstrated under air and submerged in water (with an attached sapphire endtip §6). A preliminary study was undertaken to find suitable parameters for hard tissue cutting, leading to the identification of the $0.5 – 15$ J/cm^2 regime if the fibre has a maximum distance of 10 mm from the tissue, which is a typical distance used in such operations. The cutting time through a human femur (thickest bone shaft in a human body) was estimated as > 2 h which is much longer than conventional methods (e.g. a medical saw). An investigation into the ablation properties in water immersed conditions has to be made as well, as an initial test showed that the carbonisation/HAZ can be reduced or even eliminated in this case, and the ablation rate drastically increased. Ultimately the aim is to open the way for new minimally invasive procedures using this system and not necessary to replace well established ones, therefore a comparison to working traditional systems can be misleading, as pointed out with the cutting time for a femur. However, the use of lasers for established proceedings like osteotomy has many advantages compare to the use of mechanical methods such as; the reduction of pressure and therefor avoidance of damage to fragile bone structure, the elimination of bone flour and metal abrasions (which could lead to infection) and faster wound healing.

8 Conclusions and future work

8.1 Conclusions

In this thesis two silica hollow core fibres designed for the mid-IR region were described and characterised. The two designs are known as the Hollow Core-Photonic Crystal Fibre (HC-PCF) and the Hollow Core-Negative Curvature Fibre (HC-NCF). There is a need for fibres guiding in the mid-IR driven by many applications exploiting this wavelength region such as biological imaging, gas sensing, spectroscopy and medicine. Medicine is the main driver for the presented fibre in this work, as they are capable of delivering laser radiation at 2.94 µm which coincides with an absorption peak of water, and therefore leads to high absorption by biological material. There are several advantages to use lasers for surgery, to mention some: potential for thinner cuts, non-contact operation which increases sterility, the cut geometry is independent of the tool and faster wound healing as described in detail in the introduction and literature review. To utilise all these advantages one would like to have a truly flexible delivery system to the patient, which can be achieved by optical fibres. The current state of the art fibres have a number of drawbacks and therefore an alternative solution is required. One issue with current fibres is the inability to guide sufficient energies whilst maintaining a single mode (like) or unchanging output beam profile. As both fibres presented here are hollow core the interaction of the fibre material with the laser radiation can be minimised leading to high damage thresholds with simultaneous preservation of the beam profile during bending.

The HC-PCF presented here guides due to a photonic bandgap effect, which arises from a periodical structure surrounding the core. This structure is made out of silica and air holes leading to forbidden zones for the light and is therefore confined inside the core. The remarkable property of the fibre is that, as demonstrated in this work, there are no additional losses due to bending, even down to a bending radius of <2.5 mm. Also the energy handling capability, delivering a fluence of over 3000 J/cm^2, is far over the required 35 J/cm^2 for medical surgery, and leaves enough energy excess such that losses in a fully functional system can be overcome. These two combined attributes are significant if the fibre is to be used in medical, and more specifically in minimally invasive, procedures like endoscopy, where a small bending radius is important to extend the usability for hard to reach areas. Another very important characteristic of the fibre is its single mode guidance, and that the beam profile is not changing when the fibre is bent, which avoids accidental tissue damage, and gives a well-defined cut geometry.

However if the fibre is used in practical manner it has to be stored in a dry atmosphere after it has been fabricated to avoid humidity/OH penetrating the core. One way to do this is the hermetic sealing using the sapphire endtips presented in this work. This will introduce more losses into the system, but because of the energy handling capability of the fibres this can be more than compensated for.

The key parameters and features of the HC-PCF are:

- core size: 24 µm
- NA: 0.12
- fibre length is limited by the preform, in this case 50 m were drawn
- delivered pulse energy: 14 mJ (at 15 Hz)
- delivered fluence: 3200 J/cm^2 (40 cm piece of fibre)
- attenuation at 2.94 µm: 1.1 dB/m
- minimum bend radius for high power delivery: 2.5 mm
- sufficient for ablation
- no additional losses due to fibre bending
- highly flexible and robust
- based on non-toxic material

The second fibre which was investigated in this work is the hollow core-negative curvature fibre which consists of a core wall that is curved in an opposite sense to the natural curvature of the fibre, hence the name. The guidance of the fibre is due to the Anti-Reflection Resonance Optical Waveguide (ARROW) effect, which describes the destructive interference of the Fabry-Perot interferometer that is constructed by the two interfaces of the inner wall with the air on both sides. As was described in the literature review, the negative curvature of the inner wall, moves the interstices of two neighbouring elements of the cladding structure away from the core, which reduces the attenuation of the fibre, as these studs are able to support the first cladding modes. This fibre can deliver fluencies up to <2000 J/cm^2 for shorter pieces (44 cm) and even for a nearly 10 m long fibre the output energy is still more than sufficient to ablate biological tissue. It could also be shown that the fibre again guides in a single mode like output, however it has a slight dependence on bending if the fibre is bent below a radius of 15 cm. The additional losses are in the order of 0.8 dB for a 180 degree bend at a bending radius of 10 cm, where the highest losses occur. Simulations could show that these additional losses are due to mode coupling from the core to the cladding, however these losses are low enough such

that the fibre can still operate at these (and lower) bends without damage and with sufficient output energies for tissue ablation.

The key parameters and features of the HC-NCF are:

- core size: 94 µm
- NA: 0.03
- fibre length is limited by the preform, in this case 83 m were drawn
- delivered pulse energy: 195 mJ (at 15 Hz)
- delivered fluence: 2200 J/cm^2 (33 cm piece of fibre) and 760 J/cm^2 (9.88 m piece of fibre)
- attenuation at 2.94 µm: 0.18 dB/m
- losses are independent of bending for radii > 15 cm
- low loss dependence for bending radii < 15 cm (< 1 dB)
- sufficient for ablation
- highly flexible
- based on non- toxic material

The presented fibres were compared to state of the art fibres for the same wavelength such as, chalcogenide glass fibres, sapphire glass fibres and Hollow Waveguides (HWG). One of the main advantages of the fibres is the use of silica as the fibre material, which avoids many difficulties during the fabrication and handling of the preform and fibre seen with other materials. Chalcogenide glass fibre can contain toxic materials like arsenic so that the fabrication process has to be done in a controlled and save environment (e.g. a glove box), also in these fibres it is crucial to have very pure raw materials to minimise the attenuation. In the case of the HWG the length of the fibres that perform well at these wavelengths is currently limited and they are multimode in nature. Another important benefit of the presented fibres is their ability to guide the light in a single mode, leading to a well-defined output beam profile independent of fibre bending. The alternative fibres guide mostly multimode beams as the core is relatively big, which is necessary to avoid damage to the fibre due to the limited LIDT. This is overcome in silica fibres by the use of a hollow core, minimising the interaction of the laser light with the material. Also as mentioned earlier the attenuation of the fibres is independent from fibre bend radius for the HC-PCF and weakly dependent in the case of the HC-NCF, whereas most multimode fibres have a higher loss dependence on bending.

As both fibres are hollow core it is necessary to encapsulate these, to avoid contaminations penetrating the core and therefore resulting in catastrophic damage. This was the second key part of the thesis. The so called endtip is fabricated out of a sapphire tube which is sealed with a sapphire window using a high temperature frit. The evolution and development of the endtip was described evolving from a sapphire fibre inside a glass capillary (where there were significant problems with the material property mismatch and polishing of the surfaces) to a more robust, fully sapphire final design. The justifications for using the full sapphire design are based on both the material optical properties (it is transparent in the relevant wavelength with a high LIDT) and the mechanical properties (sapphire is a robust and temperature stable material). Both attributes are necessary for the proposed purpose for a stable sealing of the fibres, without compromising the fibres natural advantages too much. The endtip was characterised for its optical and mechanical properties, with the conclusion that it can withstand the mechanical stresses that will occur during the practical use of the encapsulated fibre system, also the degradation of the beam due to the endtip is minimal and is still useful for the applications in mind. Another advantage of the proposed sapphire endtip design is its wide use over different wavelengths and for different sized fibres, so that it is not only limited to the fibres presented in this work.

The main aim of the thesis was to demonstrate the feasibility to use a silica fibre for medical applications concentrating on the high power applications like surgery. This could be shown using the HC-NCF in combination with the sapphire endtip to ablate different tissues types. The fibre itself was about 2 m long and bent in several places with an undefined bending radius; this was done to simulate an actual operating theatre. To make the experiments as realistic as possible the system was used in different environments and in different setups, these included:

- ablation tests in air and submerged in water
- different distances between the fibre endtip and the tissue
- moving the fibre and keeping the sample stable and vice versa
- holding the fibre in hand to simulate a surgeon’s movement

It could be demonstrated that the system could perform tissue ablation in all the above mentioned conditions, which demonstrates the feasibility for the use of such fibres in real operations.

8.2 Future work

For a true flexible “laser scalpel” to become reality there are some points which have to be addressed that were not within the scope of this work.

Generally for all laser based surgical applications there is a problem with an accurate feedback for the cutting depth. As haptic feedback, as is the case with mechanical tools, is missing (at least if the laser/delivery system is used in non-contact mode) it is hard for the surgeon to estimate the cutting depth with confidence. As was already mentioned in the literature review, there are several approaches to overcome this problem, such as calculation of the ablation rate and therefore estimating the depth. However there are still problems with this system, and they are not optimised for the use of endoscopic surgery.

Another point which has to be addressed for general laser medicine is the finding and standardisation of parameter regions which can be used for different tissue types. These parameters include:

- Optimal pulse shape (e.g. the use of variable square pulsed lasers)
- Optimal pulse length
- An energy density region where ablation occurs but no carbonisation, to allow for fluctuations in the system and different distances between the laser output side and the tissue (different spot sizes)
- Optimal water spray parameters (flow rate and water layer thickness)

This is a process which is complicated by the vast variety of lasers already available on the market, and their (slightly) different parameters. As the example in this work showed there is a lot experimentation involved in finding one regime for one tissue type in a certain condition using one laser system, therefore an optimisation of all parameters and for different systems will take time.

In terms of fibre delivered systems (not specifically for the ones presented) there is work to be done on the packaging of the fibres including an encapsulation of the system. The advantage of using fibre delivered laser light is the flexibility it enables, which would be corrupted if a thick and inflexible packaging is needed to make the system safe for medical, specifically endoscopic, applications. In this context the endtip can be redesigned to be implemented into the packaging system, to allow for a fully immersed system, also the possibility of the sapphire window shaping should be investigated. This can lead to output beam shaping like, focusing the beam to a desired distance, collimating

the beam to make the spot size independent of the stand-off distance and the use of elliptical spots which could be beneficial for cuts.

Future work on the presented HC-PCF has to be carried with respect to the optimisation of the coupling efficiency. To do this new fibres have to be drawn so that the attenuation of the fibre is down to the original measured value of ~1.1 dB/m, and then tested with the high beam quality laser system (Sheaumann). If these are successful and optimal parameters are found the tissue ablation test should be repeated using the HC-PCF to justify the statement that the delivered energy densities are high enough for biological tissue ablation. Also, autoclave tests (for sterilisation) should be undertaken with these fibres to find out if the final system would be reusable or disposable and therefore have a better understanding of the costs for a final product.

In the case of the HC-NCF the main work should be concentrated on the investigation of the bend sensitivity and how it can be avoided/eliminated or compensated for using closed loop power feedback. The next step in progress is to draw a new set fibre where the bandgap is centred at 2.94 µm and not around 3.2 µm as it is at the current fibre design. This might also have influences on the attenuations due to bending. Another approach to which could be using a HC-NCF design in which the individual capillaries in the cladding structure are not in contact to each other.

Ultimately it is the aim to show a fully functional system that is capable of minimally invasive surgery, using an optimised laser system that is fibre coupled into the hollow core silica fibre and sealed with a (shaped) sapphire window. A fully functional closed loop feedback system would be implemented to have monitoring of cut depth and quality and to avoid damage to non-target areas. All this will hopefully lead to new procedures in medicine that are not possible with systems currently in use ultimately resulting in improving the wellbeing of the world's population.

References

1. McGuff, P.E., R.A. Deterling Jr, L.S. Gottlieb, H.D. Fahimi, D. Bushnell, and F. Roeber, *The laser treatment of experimental malignant tumours.* Canadian Medical Association Journal, 1964. **91**(21): p. 1089.
2. McGuff, P., R.A. Deterling Jr, and L. Gottieb, *Tumoricidal effect of laser energy on experimental and human malignant tumors.* New England Journal of Mededicine, 1965. **273**: p. 286-293.
3. Izawa, T., N. Shibata, and A. Takeda, *Optical attenuation in pure and doped fused silica in the IR wavelength region.* Applied Physics Letters, 1977. **31**(1): p. 33-35.
4. Solon, L.R., R. Aronson, and G. Gould, *Physiological implications of laser beams.* Science, 1961. **134**(3489): p. 1506-8.
5. Marks, A. and J.H. Teichman, *Lasers in clinical urology: state of the art and new horizons.* World Journal of Urology, 2007. **25**(3): p. 227-233.
6. McGuff, P.E., D. Bushnell, H.S. Soroff, and R.A. Deterling, Jr., *Studies of the Surgical Applications of Laser (Light Amplification by Stimulated Emission of Radiation).* Surg Forum, 1963. **14**: p. 143-5.
7. Stellar, S., T.G. Polanyi, and H.C. Bredemeier, *Experimental studies with the carbon dioxide laser as a neurosurgical instrument.* Medical and biological engineering, 1970. **8**(6): p. 549-558.
8. Peng, Q., A. Juzeniene, J. Chen, L.O. Svaasand, T. Warloe, K.E. Giercksky, and J. Moan, *Lasers in medicine.* Reports on Progress in Physics, 2008. **71**(5).
9. Anderson, R.R. and J.A. Parrish, *Selective photothermolysis: precise microsurgery by selective absorption of pulsed radiation.* Science, 1983. **220**(4596): p. 524-7.
10. Lin, S., Q.H. Liu, Q.M. Peng, M.G. Lin, Z.L. Zhan, and X.Z. Zhang, *The ablation threshold of Er:YAG laser and Er,Cr:YSGG laser in dental dentin.* Scientific Research and Essays. **5**(16): p. 2128-2135.
11. Shapshay, S.M., E.E. Rebeiz, R.K. Bohigian, and R.L. Hybels, *Benign lesions of the larynx: should the laser be used?* Laryngoscope, 1990. **100**(9): p. 953-7.
12. Nishioka, N.S., *Applications of lasers in gastroenterology.* Lasers in Surgery and Medicine, 1995. **16**(3): p. 205-214.
13. Stubinger, S., V.B. von Rechenberg, H.F. Zeilhofer, R. Sader, and C. Landes, *Er : YAG laser osteotomy for removal of impacted teeth: Clinical comparison of two techniques.* Lasers in Surgery and Medicine, 2007. **39**(7): p. 583-588.
14. Robertson, C.W. and D. Williams, *Lambert absorption coefficients of water in the infrared.* Journal of the Optical Socioety of America, 1971. **61**(10): p. 1316-1320.
15. Peavy, G.M., L. Reinisch, J.T. Payne, and V. Venugopalan, *Comparison of cortical bone ablations by using infrared laser wavelengths 2.9 to 9.2 μm.* Lasers in Surgery and Medicine, 1999. **25**(5): p. 421-434.
16. Bader, C. and I. Krejci, *Indications and limitations of Er: YAG laser applications in dentistry.* American journal of dentistry, 2006. **19**(3): p. 178.
17. Bornstein, E. and M. Lomke, *The safety and effectiveness of dental Er: YAG lasers. A literature review with specific reference to bone.* Dentistry today, 2003. **22**(10): p. 129.
18. Horch, H., R. McCord, and E. Keiditsch, *Histological and long term results following laser osteotomy.* Laser Surgery, 1978. **2**: p. 319-325.
19. Horch, H., *Current status of laser osteotomy.* Der Orthopäde, 1984. **13**(2): p. 125.
20. Clayman, L., T. Fuller, and H. Beckman, *Healing of continuous-wave and rapid superpulsed, carbon dioxide, laser-induced bone defects.* Journal of oral surgery (American Dental Association: 1965), 1978. **36**(12): p. 932.

21. Gopin, B., C. Cobb, J. Rapley, and W. Killoy, *Histologic evaluation of soft tissue attachment to CO2 laser-treated root surfaces: an in vivo study.* The International Journal of Periodontics and Restorative Dentistry, 1997. **17**(4): p. 316-325.
22. Eriksson, R. and R. Adell, *Temperatures during drilling for the placement of implants using the osseointegration technique.* Journal of Oral and Maxillofacial Surgery, 1986. **44**(1): p. 4-7.
23. Eriksson, A. and T. Albrektsson, *Temperature threshold levels for heat-induced bone tissue injury: a vital-microscopic study in the rabbit.* The Journal of prosthetic dentistry, 1983. **50**(1): p. 101.
24. Pearson, G. and K. Schuckert, *The role of lasers in dentistry: present and future.* Dental update, 2003. **30**(2): p. 70.
25. Anic, I., I. Miletic, S.J. Krmek, J. Borcic, and S. Pezelj-Ribaric, *Vibrations produced during erbium: yttrium–aluminum–garnet laser irradiation.* Lasers in Medical Science, 2009. **24**(5): p. 697-701.
26. Ishii, J., K. Fujita, and T. Komori, *Laser surgery as a treatment for oral leukoplakia.* Oral oncology, 2003. **39**(8): p. 759-769.
27. Alster, T.S. and C. Handrick. *Laser treatment of hypertrophic scars, keloids, and striae*. in *Seminars in cutaneous medicine and surgery*. 2000. Elsevier.
28. Wang, X., C. Zhang, and K. Matsumoto, *In vivo study of the healing processes that occur in the jaws of rabbits following perforation by an Er, Cr: YSGG laser.* Lasers in Medical Science, 2005. **20**(1): p. 21-27.
29. Stübinger, S., *Advances in bone surgery: the Er: YAG laser in oral surgery and implant dentistry.* Clinical, Cosmetic and Investigational Dentistry, 2010. **2**: p. 47-62.
30. Keller, U., R. Hibst, W. Geurtsen, R. Schilke, D. Heidemann, B. Klaiber, and W.H.M. Raab, *Erbium : YAG laser application in caries therapy. Evaluation of patient perception and acceptance.* Journal of Dentistry, 1998. **26**(8): p. 649-656.
31. de Mello, E.D.A., R.M. Pagnoncelli, E. Munin, M. Sant'Ana Filho, G.P.S. de Mello, E.A.L. Arisawa, and M.G. de Oliveira, *Comparative histological analysis of bone healing of standardized bone defects performed with the Er: YAG laser and steel burs.* Lasers in Medical Science, 2008. **23**(3): p. 253-260.
32. Pourzarandian, A., H. Watanabe, A. Aoki, S. Ichinose, K.M. Sasaki, H. Nitta, and I. Ishikawa, *Histological and TEM examination of early stages of bone healing after Er: YAG laser irradiation.* Photomedicine and Laser Therapy, 2004. **22**(4): p. 342-350.
33. Taneri, S., J.D. Zieske, and D.T. Azar, *Evolution, techniques, clinical outcomes, and pathophysiology of LASEK: review of the literature.* Survey of Ophthalmology, 2004. **49**(6): p. 576-602.
34. Pallikaris, I.G. and D.S. Siganos, *Laser in situ keratomileusis to treat myopia: Early experience.* Journal of Cataract and Refractive Surgery, 1997. **23**(1): p. 39-49.
35. Hohlweg-Majert, B., H. Deppe, M.C. Metzger, S. Stopp, K.-D. Wolff, and T.C. Lueth, *Bone treatment laser-navigated surgery.* Lasers in Medical Science, 2010. **25**(1): p. 67-71.
36. Stopp, S., D. Svejdar, H. Deppe, and T.C. Lueth. *A new method for optimized laser treatment by laser focus navigation and distance visualization*. in *Engineering in Medicine and Biology Society, 2007. EMBS 2007. 29th Annual International Conference of the IEEE*. 2007. IEEE.
37. Stopp, S., H. Deppe, and T. Lueth, *A new concept for navigated laser surgery.* Lasers in Medical Science, 2008. **23**(3): p. 261-266.
38. Stopp, S., D. Svejdar, E. von Kienlin, H. Deppe, and T.C. Lueth, *A new approach for creating defined geometries by navigated laser ablation based on volumetric*

3-D data. Biomedical Engineering, IEEE Transactions on, 2008. **55**(7): p. 1872-1880.
39. Rupprecht, S., K. Tangermann-Gerk, J. Wiltfang, F.W. Neukam, and A. Schlegel, *Sensor-based laser ablation for tissue specific cutting: an experimental study.* Lasers in Medical Science, 2004. **19**(2): p. 81-88.
40. Rupprecht, S., K. Tangermann-Gerk, S. Schultze-Mosgau, F.W. Neukam, and J. Ellrich, *Neurophysiological monitoring of alveolar nerve function during sensor-controlled Er: YAG laser corticotomy in rabbits.* Lasers in Surgery and Medicine, 2005. **36**(3): p. 186-192.
41. Rupprecht, S., K. Tangermann, P. Kessler, F.W. Neukam, and J. Wiltfang, *Er: YAG laser osteotomy directed by sensor controlled systems.* Journal of Cranio-Maxillofacial Surgery, 2003. **31**(6): p. 337-342.
42. Ninomiya, T., Y. Miyamoto, T. Ito, A. Yamashita, M. Wakita, and T. Nishisaka, *High-intensity pulsed laser irradiation accelerates bone formation in metaphyseal trabecular bone in rat femur.* Journal of Bone and Mineral Metabolism, 2003. **21**(2): p. 67-73.
43. Nuss, R.C., R.L. Fabian, R. Sarkar, and C.A. Puliafito, *Infrared laser bone ablation.* Lasers in Surgery and Medicine, 1988. **8**(4): p. 381-391.
44. Pierce, M.C., M.R. Dickinson, and H. Devlin, *Selective photothermal ablation of tissue with a fibre delivered Er : YAG laser.* Laser-Tissue Interaction X: Photochemical, Photothermal, and Photomechanical, Proceedings Of, 1999. **3601**: p. 362-368.
45. Hohenleutner, U., S. Hohenleutner, W. Baumler, and M. Landthaler, *Fast and effective skin ablation with an Er:YAG laser: Determination of ablation rates and thermal damage zones.* Lasers in Surgery and Medicine, 1997. **20**(3): p. 242-247.
46. Wesendahl, T., P. Janknecht, B. Ott, and M. Frenz, *Erbium:YAG laser ablation of retinal tissue under perfluorodecaline: determination of laser tissue interaction in pig eyes.* Investigative Ophthalmology and Visual Science, 2000. **41**(2): p. 505-512.
47. Nishimoto, Y., M. Otsukii, M. Yamauti, T. Eguchi, Y. Sato, R.M. Foxton, and J. Tagami, *Effect of pulse duration of Er : YAG laser on dentin ablation.* Dental Materials Journal, 2008. **27**(3): p. 433-439.
48. Parry, J.P., T.J. Stephens, J.D. Shephard, J.D.C. Jones, and D.P. Hand, *Analysis of optical damage mechanisms in hollow-core waveguides delivering nanosecond pulses from a Q-switched Nd : YAG laser.* Applied Optics, 2006. **45**(36): p. 9160-9167.
49. Contente, M., F. de Lima, R. Galo, J. Pécora, L. Bachmann, R. Palma-Dibb, and M. Borsatto, *Temperature rise during Er:YAG cavity preparation of primary enamel.* Lasers in Medical Science: p. 1-5.
50. Walsh, J.T. and T.F. Deutsch, *Er Yag laser ablation of tissue - measurement of ablation rates.* Lasers in Surgery and Medicine, 1989. **9**(4): p. 327-337.
51. Ith, M., H. Pratisto, H. Altermatt, M. Frenz, and H. Weber, *Dynamics of laser-induced channel formation in water and influence of pulse duration on the ablation of biotissue under water with pulsed erbium-laser radiation.* Applied Physics B, 1994. **59**(6): p. 621-629.
52. Scammon, R.J., E.J. Chapyak, R.P. Godwin, and A. Vogel. *Simulations of shock waves and cavitation bubbles produced in water by picosecond and nanosecond laser pulses*. in *Proc. SPIE*. 1998.
53. Jansen PhD, E.D., M. Frenz PhD, K.A. Kadipasaoglu PhD, T.J. Pfefer MS, H.J. Altermatt MD, M. Motamedi PhD, and A.J. Welch PhD, *Laser–tissue interaction during transmyocardial laser revascularization.* The Annals of thoracic surgery, 1997. **63**(3): p. 640-647.

54. Mir, M., N. Gutknecht, R. Poprawe, L. Vanweersch, and F. Lampert, *Visualising the procedures in the influence of water on the ablation of dental hard tissue with erbium:yttrium-aluminium-garnet and erbium, chromium:yttrium-scandium-gallium-garnet laser pulses.* Lasers in Medical Science, 2009. **24**(3): p. 365-374.
55. Nahen, K. and A. Vogel, *Plume dynamics and shielding by the ablation plume during Er : YAG laser ablation.* Journal of Biomedical Optics, 2002. **7**(2): p. 165-178.
56. Colucci, V., F. Lucisano Botelho do Amaral, J. Pécora, R. Palma-Dibb, and S. Milori Corona, *Water flow on erbium:yttrium–aluminum–garnet laser irradiation: effects on dental tissues.* Lasers in Medical Science, 2009. **24**(5): p. 811-818.
57. Fried, D., N. Ashouri, T. Breunig, and R. Shori, *Mechanism of water augmentation during IR laser ablation of dental enamel.* Lasers in Surgery and Medicine, 2002. **31**(3): p. 186-193.
58. Mir, M., J. Meister, R. Franzen, S. Sabounchi, F. Lampert, and N. Gutknecht, *Influence of water-layer thickness on Er:YAG laser ablation of enamel of bovine anterior teeth.* Lasers in Medical Science, 2008. **23**(4): p. 451-457.
59. *http://www.tfederdds.com/powerlase_at.html*.06.07.13
60. Iancu, C., *Advances in Endoscopic Surgery*2011: InTech.
61. Humbach, O., H. Fabian, U. Grzesik, U. Haken, and W. Heitmann, *Analysis of OH absorption bands in synthetic silica.* Journal of Non-Crystalline Solids, 1996. **203**(0): p. 19-26.
62. Sanghera, J.S. and I.D. Aggarwal, *Development of chalcogenide glass fiber optics at NRL.* Journal of Non-Crystalline Solids, 1997. **213**: p. 63-67.
63. Aggarwal, I.D. and J.S. Sanghera, *Development and applications of chalcogenide glass optical fibers at NRL.* Journal of Optoelectronics and Advanced Materials, 2002. **4**(3): p. 665-678.
64. Seddon, A.B., *Chalcogenide Glasses - a Review of Their Preparation, Properties and Applications.* Journal of Non-Crystalline Solids, 1995. **184**: p. 44-50.
65. Sanghera, J.S., L.B. Shaw, and I.D. Aggarwal, *Applications of chalcogenide glass optical fibers.* Comptes Rendus Chimie, 2002. **5**(12): p. 873-883.
66. Shiryaev, V.S. and M.F. Churbanov, *Trends and prospects for development of chalcogenide fibers for mid-infrared transmission.* Journal of Non-Crystalline Solids, (0).
67. Snopatin, G., M. Churbanov, A. Pushkin, V. Gerasimenko, E. Dianov, and V. Plotnichenko, *High purity arsenic-sulfide glasses and fibers with minimum attenuation of 12 dB/km.* Optoelectron. Adv. Mater.-Rapid Commun, 2009. **3**(7): p. 669-671.
68. Conseil, C., Q. Coulombier, C. Boussard-Plédel, J. Troles, L. Brilland, G. Renversez, D. Mechin, B. Bureau, J.L. Adam, and J. Lucas, *Chalcogenide step index and microstructured single mode fibers.* Journal of Non-Crystalline Solids, 2011. **357**(11–13): p. 2480-2483.
69. Papagiakoumou, E., D.N. Papadopoulos, N. Anastasopoulou, and A.A. Serafetinides, *Comparative evaluation of HP oxide glass fibers for Q-switched and free-running Er : YAG laser beam propagation.* Optics Communications, 2003. **220**(1-3): p. 151-160.
70. Scott, N.J., R.A. Barton, A.L. Casperson, A. Tchapyjnikov, K. Levin, D. Tran, and N.M. Fried, *Mid-IR germanium oxide fibers for contact erbium laser tissue ablation in endoscopic surgery.* Ieee Journal of Selected Topics in Quantum Electronics, 2007. **13**(6): p. 1709-1714.
71. Poulain, M., M. Chanthanasinh, and J. Lucas, *New fluoride glasses.* Mater. Res. Bull.;(United States), 1977. **12**(2).

72. Kotsifaki, D.G. and A.A. Serafetinides, *Mid-infrared radiation transmission through fluoride glass multimode optical fibers.* Optics and Laser Technology, 2011. **43**(8): p. 1448-1452.
73. Haggerty, J., *Production of fibers by a floating zone fiber drawing technique*1972: Belvoir Defense Technical Information Center MAY. 59.
74. Merberg, G.N. and J.A. Harrington, *Optical and mechanical properties of single-crystal sapphire optical fibers.* Applied Optics, 1993. **32**(18): p. 3201-3209.
75. Nubling, R.K. and J.A. Harrington, *Optical properties of single-crystal sapphire fibers.* Applied Optics, 1997. **36**(24): p. 5934-5940.
76. Jundt, D., M. Fejer, and R. Byer, *Characterization of single-crystal sapphire fibers for optical power delivery systems.* Applied Physics Letters, 1989. **55**(21): p. 2170-2172.
77. Fried, N.M., Y.B. Yang, C.A. Chaney, and D. Fried, *Transmission of Q-switched erbium: YSGG (lambda=2.79 mu m) and erbium: YAG (lambda=2.94 mu m) laser radiation through germanium oxide and sapphire optical fibres at high pulse energies.* Lasers in Medical Science, 2004. **19**(3): p. 155-160.
78. Bouaggad, A., G. Fonteneau, and J. Lucas, *New zirconium free multicomponent fluoride glasses.* Materials Research Bulletin, 1987. **22**(5): p. 685-689.
79. Jelinkova, H., M. Nemec, J. Sulc, P. Cerny, M. Miyagi, Y.W. Shi, and Y. Matsuura, *Hollow waveguide delivery systems for laser technological application.* Progress in Quantum Electronics, 2004. **28**(3-4): p. 145-164.
80. Harrington, J.A., *A review of IR transmitting, hollow waveguides.* Fiber and Integrated Optics, 2000. **19**(3): p. 211-227.
81. George, R. and J.A. Harrington, *Infrared transmissive, hollow plastic waveguides with inner Ag–AgI coatings.* Applied Optics, 2005. **44**(30): p. 6449-6455.
82. Bledt, C.M., J.A. Harrington, and J.M. Kriesel, *Loss and modal properties of Ag/AgI hollow glass waveguides.* Appleid Optics, 2012. **51**(16): p. 3114-3119.
83. Harrington, J.A., *Infrared hollow waveguides: an update.* Proc. SPIE, 2008. Optical Fibers and Sensors for Medical Diagnostics and Treatment Applications VIII: p. 68520M-68520M.
84. Marcatili, E. and R. Schmeltzer, *Hollow metallic and dielectric waveguides for long distance optical transmission and lasers(Long distance optical transmission in hollow dielectric and metal circular waveguides, examining normal mode propagation).* Bell System Technical Journal, 1964. **43**: p. 1783-1809.
85. http://www.rp-photonics.com/m2_factor.html. 06.07.13
86. Matsuura, Y. and M. Miyagi, *Er:YAG, CO, and CO2 laser delivery by ZnS-coated Ag hollow waveguides.* Applied Optics, 1993. **32**(33): p. 6598-6601.
87. Němec, M., H. Jelínková, M. Miyagi, K. Iwai, and Y. Matsuura, *250 um inner diameter hollow waveguide for Er:YAG laser radiation.* 2009: p. 71730H-71730H.
88. Matsuura, Y., R. Kasahara, T. Katagiri, and M. Miyagi, *Hollow infrared fibers fabricated by glass-drawing technique.* Optics Express, 2002. **10**(12): p. 488-492.
89. Yablonovitch, E., *Inhibited spontaneous emission in solid-state physics and electronics.* Physical review letters, 1987. **58**(20): p. 2059-2062.
90. John, S., *Strong localization of photons in certain disordered dielectric superlattices.* Physical review letters, 1987. **58**(23): p. 2486-2489.
91. Knight, J.C., T.A. Birks, P.S. Russell, and D.M. Atkin, *All-silica single-mode optical fiber with photonic crystal cladding.* Optics Letters, 1996. **21**(19): p. 1547-1549.
92. Ouzounov, D., D. Homoelle, W. Zipfel, W. Webb, A. Gaeta, J. West, J. Fajardo, and K. Koch, *Dispersion measurements of microstructured fibers using femtosecond laser pulses.* Optics Communications, 2001. **192**(3): p. 219-223.

93. Eggleton, B., P. Westbrook, R. Windeler, S. Spälter, and T. Strasser, *Grating resonances in air-silica microstructured optical fibers.* Optics Letters, 1999. **24**(21): p. 1460-1462.
94. Bjarklev, A., A.S. Bjarklev, and J. Broeng, *Photonic crystal fibres*2003: Kluwer Academic Pub.
95. Russell, P., *Photonic Crystal Fibers.* Science, 2003. **299**(5605): p. 358-362.
96. Russell, P.S.J., *Photonic-crystal fibers.* Journal of Lightwave Technology, 2006. **24**(12): p. 4729-4749.
97. Snyder, A.W. and J. Love, *Optical waveguide theory*. Vol. 190. 1983: Springer.
98. Broeng, J., D. Mogilevstev, S.E. Barkou, and A. Bjarklev, *Photonic crystal fibers: A new class of optical waveguides.* Optical Fiber Technology, 1999. **5**(3): p. 305-330.
99. Cregan, R.F., B.J. Mangan, J.C. Knight, T.A. Birks, P.S. Russell, P.J. Roberts, and D.C. Allan, *Single-mode photonic band gap guidance of light in air.* Science, 1999. **285**(5433): p. 1537-1539.
100. Roberts, P.J., F. Couny, H. Sabert, B.J. Mangan, D.P. Williams, L. Farr, M.W. Mason, A. Tomlinson, T.A. Birks, J.C. Knight, and P.S.J. Russell, *Ultimate low loss of hollow-core photonic crystal fibres.* Optics Express, 2005. **13**(1): p. 236-244.
101. Shephard, J.D., J.D.C. Jones, D.P. Hand, G. Bouwmans, J.C. Knight, P.S. Russell, and B.J. Mangan, *High energy nanosecond laser pulses delivered single-mode through hollow-core PBG fibers.* Optics Express, 2004. **12**(4): p. 717-723.
102. Shephard, J.D., F. Couny, P.S. Russell, J.D.C. Jones, J.C. Knight, and D.P. Hand, *Improved hollow-core photonic crystal fiber design for delivery of nanosecond pulses in laser micromachining applications.* Applied Optics, 2005. **44**(21): p. 4582-4588.
103. Shephard, J.D., W.N. MacPherson, R.R.J. Maier, J.D.C. Jones, D.P. Hand, M. Mohebbi, A.K. George, P.J. Roberts, and J.C. Knight, *Single-mode mid-IR guidance in a hollow-core photonic crystal fiber.* Optics Express, 2005. **13**(18): p. 7139-7144.
104. Hensley, C.J., M.A. Foster, B. Shim, and A.L. Gaeta, *Extremely High Coupling and Transmission of High-Powered-Femtosecond Pulses in Hollow-Core Photonic Band-Gap Fiber.* 2008 Conference on Lasers and Electro-Optics and Quantum Electronics and Laser Science Conference, Vols 1-9, 2008: p. 2010-2011.
105. Ishaaya, A.A., C.J. Hensley, B. Shim, S. Schrauth, K.W. Koch, and A.L. Gaeta, *Highly-efficient coupling of linearly- and radially-polarized femtosecond pulses in hollow-core photonic band-gap fibers.* Optics Express, 2009. **17**(21): p. 18630-18637.
106. Gayraud, N., W.N. MacPherson, J.D. Shephard, R.R. Maier, D.P. Hand, J.D. Jones, J. Stone, A.K. George, and J.C. Knight. *Mid infra-red gas sensing using a hollow-core photonic bandgap fibre*. in *Optical Fiber Sensors*. 2006. Optical Society of America.
107. Kornaszewski, L., N. Gayraud, J.M. Stone, W. MacPherson, A. George, J. Knight, D. Hand, and D. Reid, *Mid-infrared methane detection in a photonic bandgap fiber using a broadband optical parametric oscillator.* Optics Express, 2007. **15**(18): p. 11219-11224.
108. Gayraud, N., Ł.W. Kornaszewski, J.M. Stone, J.C. Knight, D.T. Reid, D.P. Hand, and W.N. MacPherson, *Mid-infrared gas sensing using a photonic bandgap fiber.* Applied Optics, 2008. **47**(9): p. 1269-1277.
109. Hansen, T.P., J. Broeng, C. Jakobsen, G. Vienne, H.R. Simonsen, M.D. Nielsen, P.M.W. Skovgaard, J.R. Folkenberg, and A. Bjarklev, *Air-guiding photonic*

bandgap fibers: spectral properties, macrobending loss, and practical handling. Journal of Lightwave Technology, 2004. **22**(1): p. 11-15.
110. Bouwmans, G., F. Luan, J. Knight, P. St J Russell, L. Farr, B. Mangan, and H. Sabert, *Properties of a hollow-core photonic bandgap fiber at 850 nm wavelength.* Optics Express, 2003. **11**(14): p. 1613-1620.
111. Knight, J.C., *Photonic crystal fibres.* Nature, 2003. **424**(6950): p. 847-851.
112. Litchinitser, N.M., A.K. Abeeluck, C. Headley, and B.J. Eggleton, *Antiresonant reflecting photonic crystal optical waveguides.* Optics Letters, 2002. **27**(18): p. 1592-1594.
113. Duguay, M., Y. Kokubun, T. Koch, and L. Pfeiffer, *Antiresonant reflecting optical waveguides in SiO 2-Si multilayer structures.* Applied Physics Letters, 1986. **49**(1): p. 13-15.
114. Yu, F., W.J. Wadsworth, and J.C. Knight, *Low loss silica hollow core fibers for 3-4 μm spectral region.* Optics Express, 2012. **20**(10): p. 11153-11158.
115. Couny, F., F. Benabid, and P. Light, *Large-pitch kagome-structured hollow-core photonic crystal fiber.* Optics Letters, 2006. **31**(24): p. 3574-3576.
116. Wang, Y.Y., N.V. Wheeler, F. Couny, P.J. Roberts, and F. Benabid, *Low loss broadband transmission in hypocycloid-core Kagome hollow-core photonic crystal fiber.* Optics Letters, 2011. **36**(5): p. 669-671.
117. Février, S., B. Beaudou, and P. Viale, *Understanding origin of loss in large pitch hollow-core photonic crystal fibers and their design simplification.* Optics Express, 2010. **18**(5): p. 5142-5150.
118. Pryamikov, A.D., A.S. Biriukov, A.F. Kosolapov, V.G. Plotnichenko, S.L. Semjonov, and E.M. Dianov, *Demonstration of a waveguide regime for a silica hollow - core microstructured optical fiber with a negative curvature of the core boundary in the spectral region >3.5 μm.* Optics Express, 2011. **19**(2): p. 1441-1448.
119. Kolyadin, A.N., A.F. Kosolapov, A.D. Pryamikov, A.S. Biriukov, V.G. Plotnichenko, and E.M. Dianov, *Light transmission in negative curvature hollow core fiber in extremely high material loss region.* Optics Express, 2013. **21**(8): p. 9514-9519.
120. Kosolapov, A.F., A.D. Pryamikov, A.S. Biriukov, V.S. Shiryaev, M.S. Astapovich, G.E. Snopatin, V.G. Plotnichenko, M.F. Churbanov, and E.M. Dianov, *Demonstration of CO2-laser power delivery through chalcogenide-glass fiber with negative-curvature hollow core.* Optics Express, 2011. **19**(25): p. 25723-25728.
121. Seddon, A.B., Z. Tang, D. Furniss, S. Sujecki, and T.M. Benson, *Progress in rare-earth-doped mid-infrared fiber lasers.* Optics Express, 2010. **18**(25): p. 26704-26719.
122. Monro, T.M., Y.D. West, D.W. Hewak, N. Broderick, and D.J. Richardson, *Chalcogenide holey fibres.* Electronics Letters, 2000. **36**(24): p. 1998-2000.
123. Coulombier, Q., L. Brilland, P. Houizot, T. Chartier, T.N. N?Guyen, F. Smektala, G. Renversez, A. Monteville, D. Méchin, T. Pain, H. Orain, J.-C. Sangleboeuf, and J. Trolès, *Casting method for producing low-loss chalcogenide microstructured optical fibers.* Optics Express, 2010. **18**(9): p. 9107-9112.
124. Troles, J., Q. Coulombier, G. Canat, M. Duhant, W. Renard, P. Toupin, L. Calvez, G. Renversez, F. Smektala, M. El Amraoui, J.L. Adam, T. Chartier, D. Mechin, and L. Brilland, *Low loss microstructured chalcogenide fibers for large non linear effects at 1995 nm.* Optics Express, 2010. **18**(25): p. 26647-26654.
125. Coulombier, Q., L. Brilland, P. Houizot, T. Chartier, T.N. N'Guyen, F. Smektala, G. Renversez, A. Monteville, D. Mechin, T. Pain, H. Orain, J.C. Sangleboeuf, and

J. Troles, *Casting method for producing low-loss chalcogenide microstructured optical fibers.* Optics Express, 2010. **18**(9): p. 9107-9112.
126. Brilland, L., J. Troles, P. Houizot, F. Desevedavy, Q. Coulombier, G. Renversez, T. Chartier, T.N. Nguyen, J.-L. Adam, and N. Traynor, *Interfaces impact on the transmission of chalcogenides photonic crystal fibres.* Journal of the Ceramic Society of Japan, 2008. **116**(1358): p. 1024-1027.
127. Shi, Y.W., K. Iwai, Y. Matsuura, M. Miyagi, and H. Jelinkova, *Self-cleaning effect of sealing caps for infrared hollow fiber delivering pulsed Er : YAG laser light.* Optics and Laser Technology, 2006. **38**(2): p. 107-110.
128. Raif, J., M. Vardi, O. Nahlieli, and I. Gannot, *An Er : YAG laser endoscopic fiber delivery system for lithotripsy of salivary stones.* Lasers in Surgery and Medicine, 2006. **38**(6): p. 580-587.
129. Siegman, A.E., M.W. Sasnett, and T.F. Johnston, Jr., *Choice of clip levels for beam width measurements using knife-edge techniques.* Quantum Electronics, IEEE Journal of, 1991. **27**(4): p. 1098-1104.
130. *http://www.rp-photonics.com/rayleigh_length.html*. 04.12.2013.
131. Shephard, J.D., P.J. Roberts, J.D.C. Jones, J.C. Knight, and D.P. Hand, *Measuring beam quality of hollow core photonic crystal fibers.* Journal of Lightwave Technology, 2006. **24**(10): p. 3761-3769.
132. Dobrovinskaya, E.R., L.A. Lytvynov, and V. Pishchik, *Sapphire: Material, Manufacturing, Applications*2009: Springer Publishing Company, Incorporated. 480.
133. Sousa, J.G., D. Welford, and J. Foster, *Efficient, 1.5W CW and 7mJ quasi-CW TEM00 mode operation of a compact diode-laser-pumped 2.94ÂµÂ m Er:YAG laser.* 2010: p. 75781E-75781E.
134. Nemec, M., H. Jelinkova, J. Sulc, P. Cerny, M. Miyagi, K. Iwai, Y. Abe, Y.-W. Shi, and Y. Matsuura, *Delivery of high-energy radiation in mid-infrared spectral region by hollow waveguides.* Proc. SPIE, 2003. Optical Fibers and Sensors for Medical Applications III(178): p. 178-182.
135. Hensley, C.J., M.A. Foster, B. Shim, and A.L. Gaeta, *Extremely High Coupling and Transmission of High-Powered-Femtosecond Pulses in Hollow-Core Photonic Band-Gap Fiber*, in *2008 Conference on Lasers and Electro-Optics & Quantum Electronics and Laser Science Conference, Vols 1-9*2008, Ieee: New York. p. 2010-2011.
136. F. Rainer, L.J.A., J. H. Campbell, F. D. DeMarco, M. R. Kozolowski, A. J. Morgan, and M. C. Staggs, *Four-harmonic database of laser-damage testing.* Proc. SPIE, 1992. **116-127**.
137. Acquah, C., I. Datskov, A. Mawardi, F. Zhang, L.E. Achenie, R. Pitchumani, and E. Santos, *Optimization of an optical fiber drawing process under uncertainty.* Industrial and Engineering Chemistry Research, 2006. **45**(25): p. 8475-8483.
138. Shephard, J.D., R.I. Kangley, R.J. Hand, D. Furniss, M. O'Donnell, C.A. Miller, and A.B. Seddon, *The effect of GaSe on Ga–La–S glasses.* Journal of Non-Crystalline Solids, 2003. **326–327**(0): p. 439-445.
139. Morgan, S.P., D. Furniss, A.B. Seddon, and M.W. Moore, *Effect of glass purity on the glass stability and physical properties of Ga–La–S glasses.* Journal of Non-Crystalline Solids, 1997. **213–214**(0): p. 72-78.
140. Wu, Y., H. Yu, S. Chen, R. Sattmann, B. Cao, and J. Luo, *Effects of impurity dilution in preforms on attenuation and strength of optical fiber.* Journal of Non-Crystalline Solids. **383**(1): p. 81-85.
141. Tokiwa, H., Y. Mimura, T. Nakai, and O. Shinbori, *Fabrication of long single-mode and multimode fliuoride glass-fibers by the double-crucible technique.* Electronics Letters, 1985. **21**(24): p. 1131-1132.

142. *http://www.globalspec.com/reference/26461/203279/chapter-3-overview-of-materials-and-fabrication-technologies*. 06.07.2013.
143. Le Neindre, L., F. Smektala, K. Le Foulgoc, X.H. Zhang, and J. Lucas, *Tellurium halide optical fibers.* Journal of Non-Crystalline Solids, 1998. **242**(2–3): p. 99-103.
144. Le Coq, D., C. Boussard-Plédel, G. Fonteneau, T. Pain, B. Bureau, and J.-L. Adam, *A new approach of preform fabrication for chalcogenide fibers.* Journal of Non-Crystalline Solids, 2003. **326–327**(0): p. 451-454.
145. Savage, S.D., C.A. Miller, D. Furniss, and A.B. Seddon, *Extrusion of chalcogenide glass preforms and drawing to multimode optical fibers.* Journal of Non-Crystalline Solids, 2008. **354**(29): p. 3418-3427.
146. Furniss, D. and A.B. Seddon, *Towards monomode proportioned fibreoptic preforms by extrusion.* Journal of Non-Crystalline Solids, 1999. **256–257**(0): p. 232-236.
147. Abe, Y., T. Watanabe, H. Hiraga, and M. Miyagi, *Simplified technique of fabricating dielectric-coated silver hollow nickel waveguides by the outer-coating method of the liquid phase process.* Optics and Laser Technology, 1997. **29**(2): p. 79-82.
148. Urich, A., R.R.J. Maier, B.J. Mangan, S. Renshaw, J.C. Knight, D.P. Hand, and J.D. Shephard, *Delivery of high energy Er:YAG pulsed laser light at 2.94 mu m through a silica hollow core photonic crystal fibre.* Optics Express, 2012. **20**(6): p. 6677-6684.
149. Urich, A., R.R.J. Maier, F. Yu, J.C. Knight, D.P. Hand, and J.D. Shephard, *Flexible delivery of Er:YAG radiation at 2.94 µm with negative curvature silica glass fibers: a new solution for minimally invasive surgical procedures.* Biomedical Optics Express, 2013. **4**(2): p. 193-205.
150. Boechat, A.A.P., D.N. Su, D.R. Hall, and J.D.C. Jones, *Bend loss in large multimode optical fiber beam delivery systems.* Applied Optics, 1991. **30**(3): p. 321-327.
151. *http://www.corning.com/docs/opticalfiber/an4255.pdf*. 06.07.2013.
152. Meister, J., C. Apel, R. Franzen, and N. Gutknecht, *Influence of the spatial beam profile on hard tissue ablation Part I: Multimode emitting Er: YAG lasers.* Lasers in Medical Science, 2003. **18**(2): p. 112-118.
153. Meister, J., R. Franzen, C. Apel, and N. Gutknecht, *Influence of the spatial beam profile on hard tissue ablation, part II: pulse energy and energy density distribution in simple beams.* Lasers in Medical Science, 2004. **19**(2): p. 112-118.
154. Dragic, P., T. Hawkins, P. Foy, S. Morris, and J. Ballato, *Sapphire-derived all-glass optical fibres.* Nature Photonics, 2012. **6**(9): p. 627-633.
155. Brook, R.J., *Concise encyclopedia of advanced ceramic materials*1991: Pergamon.
156. Bucaro, J.A. and H.D. Dardy, *High-temperature Brillouin scattering in fused quartz.* Journal of Applied Physics, 1974. **45**(12): p. 5324-5329.
157. Hirano, T., M. Komatsu, H. Uenohara, A. Takahashi, K. Takayama, and T. Yoshimoto, *A novel method of drug delivery for fibrinolysis with Ho : YAG laser-induced liquid jet.* Lasers in Medical Science, 2002. **17**(3): p. 165-172.
158. Ziylan, T. and K.A. Murshid, *An analysis of anatolian human femur anthropometry.* Turkish Journal of Medical Sciences, 2002. **32**(3): p. 231-236.
159. Stübinger, S., K. Nuss, M. Pongratz, J. Price, R. Sader, H.F. Zeilhofer, and B. von Rechenberg, *Comparison of Er: YAG laser and piezoelectric osteotomy: An animal study in sheep.* Lasers in Surgery and Medicine, 2010. **42**(8): p. 743-751.

160. Stübinger, S., H.F. Zeilhofer, R. Sader, and C. Landes, *Er: YAG laser osteotomy for removal of impacted teeth: clinical comparison of two techniques.* Lasers in Surgery and Medicine, 2007. **39**(7): p. 583-588.
161. Baraba, A., I. Miletic, S.J. Krmek, T. Perhavec, Z. Bozic, and I. Anic, *Ablative Potential of the Erbium–Doped Yttrium Aluminium Garnet Laser and Conventional Handpieces: A Comparative Study.* Photomedicine and laser surgery, 2009. **27**(6): p. 921-927.
162. Lukac, M., M. Marincek, L. Grad, and Z. Bozic, *Dental laser drilling: State of art with the latest of the Variable Square Pulse Erbium dental laser systems.* Journal of Laser Health Academy, 2007. **6**: p. 1-4.